
THERMO-ELECTRIC OXIDIZATION
OF IRON
IN LITHIUM NIOBATE CRYSTALS

Dissertation

zur
Erlangung des Doktorgrades
der Naturwissenschaften

vorgelegt von

Matthias Falk

aus
Bonn

Mathematisch-Naturwissenschaftliche Fakultät
der Rheinischen Friedrich-Wilhelms-Universität Bonn

Bonn 2007

Angefertigt mit Genehmigung der Mathematisch-Naturwissenschaftlichen Fakultät
der Rheinischen Friedrich-Wilhelms-Universität Bonn

Eidesstattliche Erklärung

Hiermit erkläre ich, die vorliegende Arbeit selbständig und ohne unerlaubte Hilfe verfasst
und keine als die angegebenen Quellen und Hilfsmittel verwendet zu haben.

Bonn, 26. November 2007

Referent:	Prof. Dr. K. Buse
Korreferent:	Prof. Dr. K. Maier

Tag der Einreichung:	26. November 2007
Tag der Promotion:	20. Februar 2008

Diese Dissertation ist auf dem Hochschulschriftenserver der ULB Bonn http://hss.ulb.uni-bonn.de/diss_online elektronisch publiziert.

Erscheinungsjahr: 2008

Contents

1	Introduction	1
2	Fundamentals	3
2.1	Lithium niobate crystals	3
2.2	Nonlinear optics and photorefraction	4
2.2.1	Nonlinear-optical processes	4
2.2.2	Photorefractive effect	7
2.2.2.1	One-center model	7
2.2.2.2	Two-center model	9
2.2.2.3	Optical damage	10
2.2.2.4	Suppression of optical damage	12
2.3	Annealing	15
2.3.1	Annealing behavior of undoped lithium niobate	15
2.3.2	Annealing behavior of doped lithium niobate	17
2.3.2.1	Multivalent dopant ions and defects	17
2.3.2.2	Excitation and charge transport processes	19
2.3.2.3	Reduction	21
2.3.2.4	Oxidization	23
2.3.2.5	Annealing in the presence of an electrical field	23
3	Oxidization	25
3.1	Experimental methods	25

3.1.1	Crystals	25
3.1.2	Oxidization methods for multivalent dopant ions in lithium niobate .	26
3.1.2.1	Conventional oxidization	26
3.1.2.2	Thermo-electric oxidization	26
3.1.3	Determination of the Fe^{2+} concentration	29
3.1.3.1	Absorption spectroscopy	29
3.1.3.2	Conductivity spectroscopy	30
3.1.4	Birefringence changes	32
3.2	Experimental results	34
3.2.1	Iron concentration	34
3.2.2	Oxidization	34
3.2.3	Dynamics of the oxidization	38
3.2.3.1	Evolution of voltage and current	38
3.2.3.2	In-situ observation during annealing	40
3.2.3.3	Dynamics of the oxidization	41
3.2.3.4	Varying the parameters	42
3.2.4	Conductivity measurements	44
3.2.5	Birefringence changes at the absorption front	48
3.2.6	Investigations of the precipitation	51
3.2.7	Various dopants	51
4	Photorefraction	53
4.1	Experimental methods	53
4.1.1	Crystals	53
4.1.2	Measurements of the photorefraction	53
4.1.2.1	Beam fanning	53
4.1.2.2	Sénarmont compensator method	54
4.1.2.3	Second-harmonic generation	56
4.2	Experimental results	57
4.2.1	Photorefraction in iron-doped oxidized LiNbO_3 crystals	57
4.2.2	Photorefraction in undoped LiNbO_3 crystals	58

4.2.2.1	Single crystals	58
4.2.2.2	Periodically-poled lithium niobate	60
5	Discussion	63
5.1	Oxidization	63
5.1.1	Dynamics of the oxidization	64
5.1.2	Shock-wave model	64
5.1.2.1	Model and notation	65
5.1.2.2	Shock-wave solution	66
5.1.3	Charge compensation mechanism	68
5.1.4	Charge transport processes	70
5.1.5	Strength of the oxidization	72
5.1.5.1	Absorption spectroscopy	72
5.1.5.2	Conductivity spectra	73
5.2	Suppression of photorefraction	74
5.2.1	Photorefraction in highly iron-doped LiNbO_3 crystals	74
5.2.2	Photorefraction in undoped LiNbO_3 crystals	76
5.3	Comparison of methods to suppress optical damage	77
5.4	Connections to other fields of science	77
5.4.1	Thermal fixing	78
5.4.2	Electrochromism	79
5.4.3	Lithium ion batteries	79
5.4.4	Resistive switching	79
6	Outlook	81
7	Summary	83
	References	84
A	Sénarmont method	97

Chapter 1

Introduction

"Light influences our lives today in new ways that we could never have imagined just a few decades ago. As we move into the next century, light will play an even more significant role, enabling a revolution in world fiber-optic communications, new modalities in the practice of medicine, a more effective national defense, exploration of the frontiers of science, and much more." This statement has been given by the National Research Council of the USA in 1998 [1]. Some of these predictions have already come true, e.g., the build-up of a new and fast fiber-optic communication network by the Deutsche Telekom in Germany is in progress. Other breakthroughs in optics are imminent. Mitsubishi Digital Electronics has announced to show a large-screen laser TV at the Consumer Electronics Show in Las Vegas in January 2008 [2]. While conventional displays are able to generate about 35 % of the visible colors only, a laser TV can show nearly all possible colors. The contrast and the brightness of the displays will also benefit from lasers as light sources. The first prototype of a laser display was presented by the Schneider AG in 1993, but small and inexpensive sources for red, green, and blue laser light – one crucial point for the readiness for marketing – were not available at this time. In contrast, today the recent progress in the fields of diode lasers and nonlinear optics enables the use of compact laser diodes that emit infrared light. This light is converted by nonlinear-optical crystals into red, green and blue light beams, that write the image onto the screen. For large laser displays several watts of light power are necessary. Lithium niobate crystals [3,4] are a promising material for frequency converters. However, with standard lithium niobate crystals light powers much higher than 100 mW cannot be generated, because of the so-called "optical damage" [5]. Electrons are excited from iron impurities by light and retrapped preferentially in darker parts of the crystal. The resulting electric fields modify the refractive index of lithium niobate [6]. The consequence is a distortion of the beam shape and a limit of the achievable output power. If this obstacle can be overcome lithium niobate will be the material of choice even

for high power applications, because it is extraordinarily efficient as frequency converter, commercially available at low cost and high quality as well as robust enough for longtime operation in devices.

The aim of this work is to investigate new ways of optimizing standard lithium niobate crystals for high-power nonlinear-optical applications. Two different approaches are examined: The first idea is to increase the electric conductivity of the crystals to a point where no electric fields can persist in the crystal. Consequently, no optical damage should arise. The second approach is to remove as many electrons from the iron impurities as possible to avoid the optical damage right from the start. Both approaches are investigated in this thesis.

Chapter 2

Fundamentals

2.1 Lithium niobate crystals

Lithium niobate crystals (LiNbO_3) are an artificial material. The date of the first growth is unknown, but an early report was given by Zachariasen in 1928 [7]. The crystal structure at temperatures below the Curie point (1143°C) is shown in Fig. 2.1 [3,4,8,9]. It consists of oxygen layers and in between alternatingly a lithium ion, a niobium ion, and a vacancy along the c -axis. Above the Curie temperature the lithium ions are placed within the nearest oxygen layer and the niobium ions are located centrally in the oxygen octahedra, whereas at temperature below the Curie point lithium and niobium are shifted as shown in Fig. 2.1. This leads to a spontaneous polarization of the crystal ($P_S = 70 \mu\text{C}/\text{cm}^2$) and ferroelectric domains are formed [9]. Lithium niobate belongs to the $3m$ point group, i.e., the crystal lattice is symmetric under a rotation by 120° with respect to the c -axis. This differs from the perovskite structure, that is face-centered cubic and that many crystals of the ABO_3 composition belong to (with A and B metal ions), e.g., KNbO_3 or BaTiO_3 [10]. The peculiarity of lithium niobate implying its structure is that the ion radii of lithium ions ($r_{\text{Li}^+} = 0.68 \text{ nm}$) and niobium ions ($r_{\text{Nb}^{5+}} = 0.69 \text{ nm}$) are almost equal [11,12]. Since the Nb-O bond is stronger than the Li-O bond, the congruent crystal composition with $c_{\text{Li}}/(c_{\text{Li}} + c_{\text{Nb}}) = 48.6 \%$ is favorable compared to the stoichiometric composition, i.e., $c_{\text{Li}}/(c_{\text{Li}} + c_{\text{Nb}}) = 50 \%$ [11], with lithium and niobium concentrations c_{Li} and c_{Nb} . For charge compensation of the resulting lithium vacancies, niobium ions occupy lithium sites ($\text{Nb}_{\text{Li}}^{5+}$) [13]. Hence 20 % of the lithium vacancies are filled with niobium ions.

Some crystal properties are of special relevance for applications: Lithium niobate is mechanically robust, so it can be sawn, ground and polished easily, and it is stable against most chemicals [9]. Especially it is not hygroscopic like other optical crystals, such as lithium triborate (LiB_3O_5 , often referred to as LBO) or potassium dihydrogen phosphate

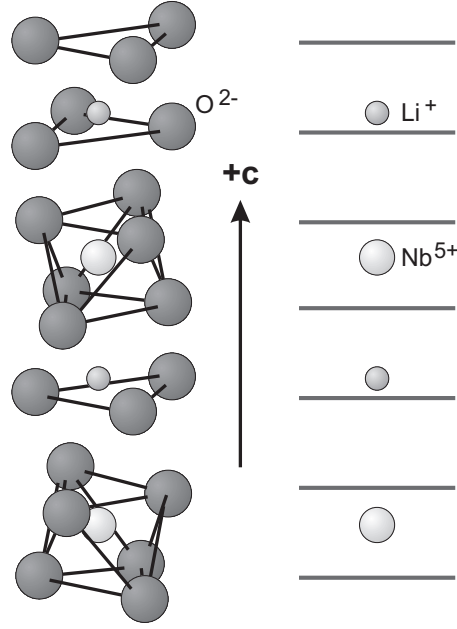


Figure 2.1: Schematic of the crystal structure of lithium niobate.

(KH_2PO_4 or KDP) that are deteriorated by water vapor. Moreover it has a large band gap of about 3.7 eV [14] that makes it transparent between wavelengths of 320 and 4000 nm [9]. Besides, lithium niobate crystals are widely used as radio frequency filters in cellular phones and TV's using surface acoustic waves [9]. That is why the crystals are commonly available in high quality and purity at low costs. These facts lead to great interest to exploit the outstanding nonlinear-optical and photorefractive properties of lithium niobate crystals.

2.2 Nonlinear optics and photorefraction

2.2.1 Nonlinear-optical processes

When an electromagnetic light wave transverses a crystal, the electrons are forced to oscillate in the electrostatic crystal potential. For small oscillation amplitudes the potential can be approximated to be harmonic. However, for larger amplitudes, i.e., higher light intensities, the anharmonicity of the crystal potential leads to an anharmonic oscillation of

the electrons. This oscillation is described by a Fourier series with non-negligible higher-order terms. The physical meaning of these terms are electromagnetic light waves with multiples of the frequency of the incident light wave.

This can also be described in a more quantitative way [15–18]: The electromagnetic wave $E(t)$

$$E(t) = E_0 e^{i\omega t} \quad (2.1)$$

polarizes the material. Here E_0 is the amplitude, ω the frequency, and t the time.

The polarization P of the crystal is usually given by

$$P = \epsilon_0 \chi^{(1)} E(t). \quad (2.2)$$

Here ϵ_0 denotes the vacuum permittivity and $\chi^{(1)}$ the electric susceptibility of the material. In the case of large amplitudes E_0 and therefore anharmonic oscillations, higher nonlinear terms of the polarization have to be taken into account

$$P = \epsilon_0 (\chi^{(1)} E(t) + \chi^{(2)} E^2(t) + \chi^{(3)} E^3(t) + \dots). \quad (2.3)$$

The higher order susceptibilities are represented by $\chi^{(n)}$ with $n > 1$. The combination of Eqs. (2.1) and (2.3) leads to

$$P = \epsilon_0 (\chi^{(1)} E_0 e^{i\omega t} + \chi^{(2)} E_0^2 e^{i2\omega t} + \dots). \quad (2.4)$$

The second term in the sum is responsible for to the emission of a light wave with frequency 2ω . This process is called second-harmonic generation (SHG) or frequency doubling. The first experimental proof of optical SHG was done by Franken et al. in 1961 [19]. The amplitude of the emitted frequency-doubled wave is proportional to the second-order susceptibility $\chi^{(2)}$, a second-rank tensor. Therefore there is a need for materials with large nonlinear susceptibilities. An overview about the nonlinear susceptibilities of various crystals that are widely used for nonlinear optics is given in Tab. 2.1. It can be seen that lithium niobate possesses extraordinarily large nonlinear coefficients [20, 21].

Due to dispersion the fundamental wave and the frequency-doubled wave propagate with different velocities. This leads to destructive interference of frequency-doubled light that is created at different crystal positions. Typical values for the propagation distance after that destructive interference takes place are several micrometers. To overcome this obstacle there exist different phase matching techniques [20, 22]. It is possible to use the birefringence of the crystal to get matching velocities, i.e., equal refractive indices, for different light polarizations. But in the case of lithium niobate this does not allow to use the largest tensor elements of the nonlinear susceptibility ($d_{13} = 4.35$ pm/V instead of $d_{33} = 27$ pm/V). The use of quasi phase-matched periodically-poled lithium niobate crystals (PPLN) is advantageous. In these crystals ferroelectric domains are structured

Name	Formula	$ \chi^{(2)} $ [pm/V]
Lithium niobate (LN)	LiNbO_3	27
Potassium niobate	KNbO_3	20.6
Potassium titanyl arsenate (KTA)	KTiOAsO_4	18.5
Potassium titanyl phosphate (KTP)	KTiOPO_4	16.9
Lithium tantalate (LT)	LiTaO_3	16
Lithium iodate	LiIO_3	5.5
Bismuth borate (BiBO)	BiB_3O_6	2.8
Beta-barium borate (BBO)	$\beta\text{-BaB}_2\text{O}_4$	2.55
Lithium borate (LBO)	LiB_3O_5	1.05
Potassium dihydrogen phosphate (KDP)	KH_2PO_4	0.44
Potassium dideuterium phosphate (KD*P)	KD_2PO_4	0.4

Table 2.1: Nonlinear susceptibilities for various commonly used crystals. The absolute values of the largest tensor elements are shown [20, 21].

such that the orientation of the c -axis is inverted periodically. With the flip of the c -axis the phase of the frequency-doubled light changes by π . If the period is suitable for the wavelength of the incident light, the phase of the frequency-doubled light is shifted before it comes to destructive interference [23]. Figure 2.2 shows schematically quasi phase matching.

In that case an effective nonlinear susceptibility of $d_{\text{eff}} = 17$ pm/V can be used. Since the nonlinear susceptibility contributes quadratically to the gained output power of the frequency-doubled light, the effort of producing PPLN is worthwhile [22].

Second-harmonic generation is not the only nonlinear-optical process. With similar considerations like above, e.g., sum frequency generation can be achieved, i.e., two light beams of different frequencies ω_1 and ω_2 generate a third beam with frequency $\omega_3 = \omega_1 + \omega_2$, or difference frequency generation ($\omega_3 = \omega_1 - \omega_2$), or optical parametric oscillation, where one beam with frequency ω_1 creates two beams with $\omega_1 = \omega_2 + \omega_3$.

All these nonlinear-optical processes need phase matching. However, if the refractive indices are modified, e.g., by temperature changes or by illumination itself, the output power decreases strongly. Refractive index changes as small as 10^{-5} are sufficient to disturb the phase matching critically. Light-induced refractive index changes can occur due to the photorefractive effect [6]. This is the case especially at high light intensities, that are desired for nonlinear optics, because, e.g., the output power of the frequency-doubled wave depends quadratically on the intensity of the incident fundamental wave (Eq. (2.4)). One aim of this work is therefore to suppress the photorefractive effect in LiNbO_3 crystals.

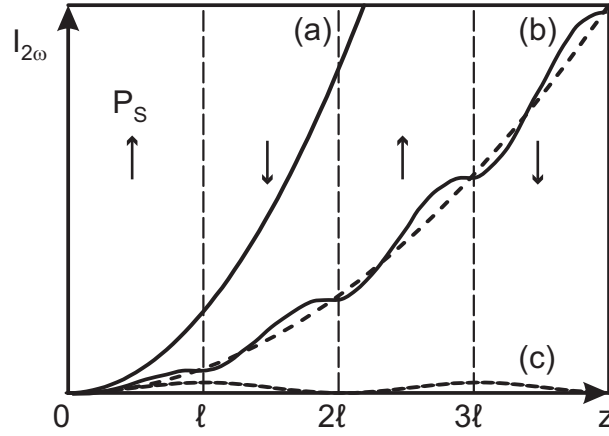


Figure 2.2: Schematic of quasi-phase matching. The intensity $I_{2\omega}$ of the frequency-doubled light is shown vs. the crystal length z . The sketched periodic inversion of the spontaneous polarization P_s is only valid for graph (b). The graphs correspond to (a) (theoretical) perfect phase matching, (b) quasi-phase matching, and (c) no phase matching.

2.2.2 Photorefractive effect

In 1966 Ashkin et al. discovered that a green laser beam is distorted when it passes a lithium niobate crystal [5]. This effect is called the photorefractive effect: Light excites electrons from multivalent impurities or crystal defects to the conduction band. The subsequent electronic currents lead to a charge carrier redistribution from illuminated to darker areas. Space-charge fields arise that modulate the refractive index via the electrooptic effect. This process is considered in more detail in the following section.

2.2.2.1 One-center model

In the case that only one photorefractive center, i.e., one multivalent impurity or defect like $\text{Fe}^{2+/3+}$ is present, the photorefractive effect can be described within the framework of the one-center model [6]. A schematic of the model is depicted in Fig. 2.3. The states of the photorefractive center are located in the band gap between valence band and conduction band. Part of these defects are filled with electrons and can act as electron sources, the other part is empty and acts as traps for electrons. Light with sufficient photon energy can excite electrons from the filled centers to the conduction band leading to electric currents.

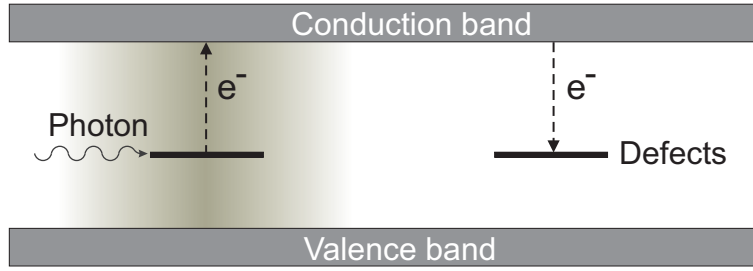


Figure 2.3: Schematic of the one-center model.

Charge driving forces The bulk photovoltaic effect and the drift of electrons act as the main charge driving forces. Other contributions such as the pyroelectric effect or diffusion often are negligible. Hence the total current density in the conduction band is given by

$$j = j_{\text{phv}} + j_{\text{drift}}. \quad (2.5)$$

These two contributions to the current density are considered in detail in the following.

- Bulk photovoltaic current density j_{phv}

$$j_{\text{phv}} = \beta^* N^- I \quad (2.6)$$

The bulk photovoltaic current density j_{phv} is determined by the appropriate element of the bulk photovoltaic tensor β^* , the concentration of filled photorefractive centers N^- and the light intensity I . Bulk photovoltaic currents, i.e., light-induced currents in the crystal bulk are possible in non-centrosymmetric crystals like LiNbO_3 . They flow along the polar c -axis.

- Drift current density j_{drift}

$$j_{\text{drift}} = \sigma E \quad (2.7)$$

The drift current density j_{drift} is the product of the electrical conductivity σ and the electrical field E (Ohm's law). The electrical conductivity is given by the sum of the dark conductivity σ_d and the photoconductivity σ_{ph} :

$$\sigma = \sigma_d + \sigma_{\text{ph}} \quad (2.8)$$

The photoconductivity can be expressed by:

$$\sigma_{\text{ph}} \propto I \frac{N^-}{N^0} \quad (2.9)$$

Here N^0 denotes the concentration of empty centers.

Space-charge fields The charge carrier redistribution due to the bulk photovoltaic currents builds up an electrical field, the so-called space-charge field, whereas the drift currents tend to decrease the electrical fields. After a while the equilibrium state is reached when $j_{\text{phv}} = j_{\text{drift}}$. In that case it follows from Eqs. (2.6–2.9):

$$E_{\text{SC}} = \frac{\beta^* N^- I}{\sigma_{\text{d}} + kI} \quad (2.10)$$

with k constant. Under typical conditions the dark conductivity σ_{d} is negligible and therefore the space-charge field E_{SC} is independent of the light intensity.

Electro-optic effect LiNbO₃ is birefringent with the refractive indices for ordinarily polarized light n_{o} and for extraordinarily polarized light n_{e} . The space-charge field modifies both refractive indices of lithium niobate via the linear electro-optic effect, also called "Pockels effect":

$$\Delta n_{\text{o,e}} = -\frac{1}{2} n_{\text{o,e}}^3 r_{13,33} E_{\text{SC}} \quad (2.11)$$

Here $\Delta n_{\text{o,e}}$ denote the refractive index changes for ordinarily and extraordinarily polarized light and $r_{13,33}$ the elements of the electro-optic tensor. The indices 13 and 33 are contracted indices. Since $r_{33} \approx 3r_{13}$ the birefringence is changed by illumination.

This one-center model is valid for nominally undoped LiNbO₃ crystals as well as for crystals that are doped with small amounts of, e.g., Fe, Cu, or Mn at small light intensities $I < 10^5 \text{ W/m}^2$.

2.2.2.2 Two-center model

For large light intensities of $I > 10^6 \text{ W/m}^2$ the two-center model is used to describe the occurring effects [6,24]. A schematic of the two-center model can be seen in Fig. 2.4.

In addition to the deep center C_1 , that is identical to the photorefractive center in the one-center model, a second shallow center C_2 is present. The Nb_{Li} antisite defect could be identified as such a shallow center. At room temperature C_2 is empty due to thermal excitation of the electrons from C_2 to the conduction band. During illumination with laser light at high intensities with a wavelength suitable to excite electrons from the deep center C_1 , electrons recombine to the shallow center C_2 and are not reexcited effectively, because the suitable absorption wavelength is much larger than the wavelength for excitation from the deep centers. These trapped electrons significantly decrease the photoconductivity. So the dependence of σ_{ph} on the light intensity is sublinear,

$$\sigma_{\text{ph}} \propto I^x \quad \text{with} \quad 0 < x < 1. \quad (2.12)$$

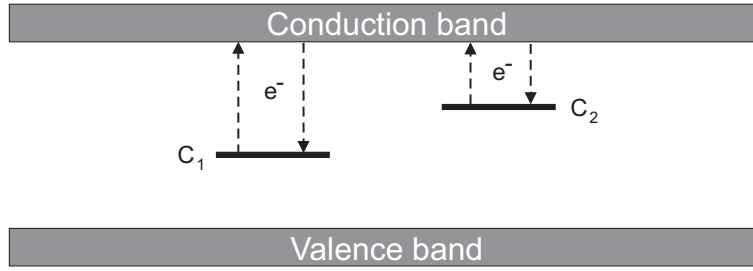


Figure 2.4: Schematic of the two-center model.

The bulk photovoltaic currents are also affected,

$$j_{\text{phv}} = \kappa_1 N_1^-(I)I + \kappa_2 N_2^-(I)I. \quad (2.13)$$

Here N_1^- and N_2^- are the concentrations of the centers C_1 and C_2 that are filled with electrons, and κ_1 and κ_2 are their bulk photovoltaic coefficients. The resulting equilibrium space-charge field is given by:

$$E_{\text{SC}} = \frac{\kappa_1 N_1^-(I)I + \kappa_2 N_2^-(I)I}{\sigma_d + kI^x} \quad (2.14)$$

Hence the space-charge field and therefore the refractive index change depends on the light intensity I .

2.2.2.3 Optical damage

The photorefractive effect is useful, e.g., to record holograms. However, for nonlinear-optical applications it is undesired and greatly limits the output power of nonlinear-optical devices. In that case it is called "optical damage". Sometimes optical damage is used as a generic term for photorefractive damage, light-induced cracks, and other undesired effects under illumination. In this thesis it is used as a synonym for unwanted light-induced refractive-index changes.

In nonlinear-optical processes such as second-harmonic generation a single light beam transverses a LiNbO_3 crystal and generates optical damage. The beam shape is distorted ("beam fanning") along the c -axis as it can be seen in Fig. 2.5.

The characteristic pattern comes from two contributions:

- A *macroscopic lens* is formed by the photorefractive effect (see Sect. 2.2.2) as well as by the thermo-optic effect, i.e., refractive index changes due to the inhomogeneous

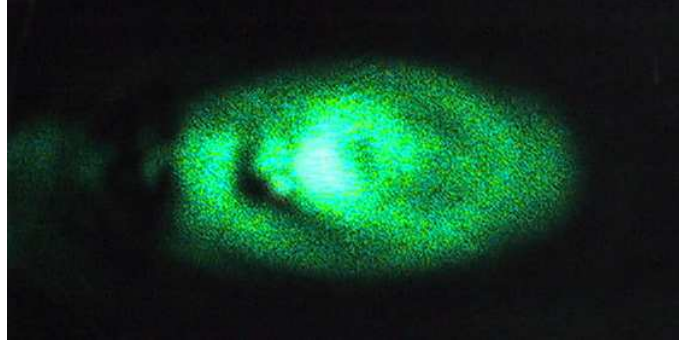


Figure 2.5: Photograph of the beam shape that is deformed by optical damage in a LiNbO_3 crystal at a light intensity of $I \approx 100 \text{ MW/m}^2$.

heating of the crystal [25]. This leads to a symmetric spread-out of the light beam. According to simulations in [25] temperature changes are the dominant contribution for intensities larger than 35 MW/m^2 ($\Delta T \geq 0.03 \text{ K}$).

- *Holographic scattering* is responsible for the irregular substructures [25]. Scattering of light on defects at the crystal surface and in the crystal bulk as well as reflection of light from the surfaces lead to a variety of light beams in different directions. These beams interfere and the resulting intensity pattern creates a refractive index pattern via the photorefractive effect that is enhanced by holographic two-wave mixing (Sect. 2.2.2). Light is diffracted at this pattern. This contribution increases with the beam diameter, because the larger the illuminated area is the more scattering centers are involved.

The refractive index changes Δn and with it the beam fanning increase with the illumination time until saturation is reached [26–28]. The evolution can be described by $\Delta n(t) = A[1 - e^{-(t/t_0)}]$ with A constant. Typical saturation times t_0 are in the range of seconds to minutes. Some authors report that Δn also depends linearly on the light intensity over a wide range of light intensities [25, 26, 28]. At high intensities the refractive-index changes saturate. The wavelength dependence of the optical damage shows a maximum near 415 nm but light-induced refractive-index changes can be generated by light of the whole visible range of the spectrum [27].

Yet another disturbing light-induced effect in LiNbO_3 , related to optical damage, is the green induced infrared absorption (GRIIRA) [29]. Illumination with green light evokes an absorption band in the infrared that is attributed to the formation of $\text{Nb}_{\text{Li}}^{4+}$ and can

be understood within the framework of the two-center model (Section 2.2.2.2). For SHG this leads to absorption of the infrared fundamental wave. The subsequent heating of the crystal disturbs the phase matching.

2.2.2.4 Suppression of optical damage

During the last 40 years since Ashkin et al. have discovered the optical damage, a large variety of methods have been proposed to overcome this disadvantage of LiNbO_3 crystals. The most promising methods are reviewed here. An attempt to compare these methods quantitatively is made in Sect. 5.3.

Crystal purity and composition Since optical damage originates from crystal defects and impurities it seems self-evident to purify the crystal growth process [30] as well as to grow stoichiometric LiNbO_3 instead of congruent material. Both possibilities are studied intensively. The main impurity in LiNbO_3 is iron. The actual impurity level is less than 1 ppm (specified by Crystal Technology, Inc.). But, nevertheless, this is not sufficient to prevent from optical damage. Even ironless crystals may exhibit optical damage due to $\text{Nb}_{\text{Li}}^{4+/5+}$ antisite defects that act as photorefractive centers [31]. To decrease their concentration, crystals with nearly equal lithium and niobium concentrations can be grown by special growth techniques [28, 32, 33] or the stoichiometry can be improved by a post-growth vapor-transport equilibration (VTE) [28, 34, 35]. Despite enormous efforts both methods can only provide nearly-stoichiometric crystals. Increase of the lithium concentration leads to stronger optical damage up to a lithium concentration of at least $c_{\text{Li}} = 49.8 \text{ mol}\%$ [28, 32, 36]. If the lithium concentration is increased further, a suppression of the photorefractivity can be reached at $c_{\text{Li}} \geq 49.9 \text{ mol}\%$ [28].

Doping The optical damage suppressing dopant reported first was magnesium (Mg^{2+}) [37, 38]. It is known that Mg doping decreases the concentration of Nb_{Li} antisite defects by replacing them and filling Li vacancies. At a doping level of 5.5 mol% all Nb_{Li} defects are replaced by Mg, and the optical damage as well as the GRIIRA drop in a threshold-like behavior. Moreover Mg doping enhances the photoconductivity [31, 38] and possibly the dark conductivity [39]. This suppresses optical damage according to Eqs. (2.9) and (2.10). Additionally, iron ions change their lattice site from Fe_{Li} to Fe_{Nb} and do not act as electron traps any more [31, 38]. Comparable results were achieved for doping with 7.5 mol% zinc (Zn^{2+}) [31, 40–45], 5 mol% indium (In^{3+}) [42, 45–48], 1.5 mol% scandium (Sc^{3+}) [49], 4 mol% hafnium (Hf^{4+}) [50, 51], and 6 mol% zirconium (Zr^{4+}) [50]. Recently, several attempts have been made to combine two or more dopants (see e.g. [52–55]). A very promising alternative is to combine increased stoichiometry with a smaller dopant

concentration of Mg [56–59]. In that case, additionally to the other optical damage suppression mechanisms, the bulk photovoltaic currents are decreased [56]. Strong optical damage suppression with nearly-stoichiometric VTE-treated LiNbO_3 crystals containing only 0.5 mol% Mg is reported in [59]. Similar results can also be achieved by combining increased stoichiometry with other optical damage suppressing dopants [60,61].

Another effect that is related to optical damage and which disturbs nonlinear-optical processes is the so-called "dark trace effect" (also called "gray trace", "gray track", and "bulk darkening"). It occurs in LiNbO_3 doped with Mg. After intense illumination with green light the crystal shows a darkening along the beam path [62,63]. This absorption can be erased by an oxidizing annealing treatment [63]. According to [62,63] the dark trace effect also occurs in $\text{LiNbO}_3\text{:Zn}$, whereas in Refs. [40,41] light-induced darkening is not observed.

A further doping ion that leads to suppressed optical damage is hydrogen (H^+). In proton exchanged waveguides with an enormous concentration of H^+ ions, strong optical damage suppression is observed [64]. As origin of this effect a decrease of the electrooptic coefficients and a decrease of the bulk photovoltaic currents are identified [64,65].

In general doping with large amounts of ions leads to worse optical quality of the crystals. Additionally, it seems to be a great challenge to create small ferroelectric domain structures that are required for quasi-phase matching, because elimination of the Nb_{Li} defects reduces the ferroelectric coercive field, i.e., the electric field that is required to reverse ferroelectric domains, by at least one order of magnitude. These defects stabilize domains. Without these defects period lengths of domain patterns of several micrometers are hard to achieve as they are required for generation of visible light by frequency doubling [66].

Illumination A further method of optical damage suppression is presented by Liu et al. [67]. If a nearly stoichiometric LiNbO_3 crystal is illuminated with UV light of the wavelength 350 nm at the same time as it is exposed to optical-damage-inducing green light ($\lambda = 532$ nm), the UV light will reduce the optical damage. The intensity of the UV light has to be only 1/7 of the intensity of the green light beam in order to suppress the optical damage almost completely. The origin of this effect is the increase of the photoconductivity of the crystal due to the UV light [67].

Heating In 1972 Ninomiya and Motoki firstly used heating to 200 °C to prevent optical damage in a LiNbO_3 -based light modulator [68]. A systematic analysis of the temperature dependence of the optical damage was performed by Rams et al. in 2000 [69]. A threshold for optical damage is observed that shifts to higher light intensities with increasing temperatures. This threshold shows an Arrhenius-type behavior with an activation energy of $E_A = 0.24$ eV.

External electrical fields With the help of large external electrical fields, additional drift currents, that compensate for the bulk photovoltaic currents, can be generated in order to shift the equilibrium space charge fields to small values. But part of the optical damage resides, because of diffusion currents that cannot be compensated by drift currents induced by an external field [70]. But, additionally to the diffusion of electrons which are excited from Fe^{2+} to the conduction band, there is also diffusion of holes formed by excitation of electrons from the valence band to Fe^{3+} . The latter process is much weaker, but both can be brought to equilibrium if the Fe^{2+} to Fe^{3+} concentration ratio $c_{\text{Fe}^{2+}}/c_{\text{Fe}^{3+}}$ is at a certain small value [70]. By means of external electric fields combined with the suitable $c_{\text{Fe}^{2+}}/c_{\text{Fe}^{3+}}$ the optical damage is reduced significantly.

Annealing treatments Several reports exist showing that annealing treatments have a permanent impact on the optical damage in LiNbO_3 crystals. In 1967 Levinstein et al. observed a significant decrease of the optical damage after annealing at 700 °C in the presence of an externally applied electrical field [71]. They attributed the suppression of the optical damage to the indiffusion and drift of an unknown impurity (possibly platinum or gold from the electrodes) into the crystal along dislocations. In these dislocations the newly introduced impurity compensates for charges of photorefractive centers and deactivates them by this means. In 1968 Smith et al. found that the annealing procedure proposed by Levinstein leads to indiffusion of hydrogen [72]. The suppression of the optical damage was claimed to be related to hydrogen, but a microscopic model was not given. In 1971 Peterson et al. explained the optical damage suppression in field annealing experiments by the drift of Fe^{2+} ions from the bulk to the negative electrode and the subsequent pullout of the Fe^{2+} . By this means only Fe^{3+} is still present in the crystals and the photorefractive effect cannot take place due to a lack of photoexcitable electrons [73].

In [74] a process is depicted in which LiNbO_3 crystals containing a waveguiding layer created by titanium (Ti) indiffusion are annealed at 150 °C while they are illuminated with an optical damage generating light beam. After cooling down to room temperature the optical damage is suppressed by one order of magnitude with this treatment. To explain this effect it is assumed that electrons from Fe^{2+} centers move along the c -axis due to the bulk photovoltaic effect and leave the illuminated area. Hydrogen impurities that are mobile at these temperatures compensate for the electric fields by drift. Finally, the optical damage is suppressed by a lack of photoexcitable electrons in the illuminated region of the crystal. This effect is also permanent because electrons and H^+ ions are immobile at room temperature and therefore cannot return.

In [75] a series of annealing experiments shows that optical damage can be suppressed by annealing of Ti-indiffused LiNbO_3 crystals at 500 °C in an oxygen atmosphere, whereas annealing in a nitrogen atmosphere deteriorates the optical damage. This effect is explained by oxidization or reduction of Fe centers in LiNbO_3 .

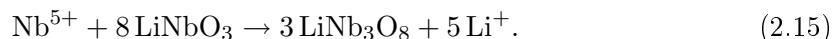
Finally, it is shown in [48,63] that annealing of Mg, Zn, or In doped LiNbO_3 at 1050-1100 °C in oxygen atmosphere permanently reduces the dark trace effect. This is attributed to oxidization, but a detailed model is not given.

In general, different annealing treatments are proposed that have a favorable impact on the optical damage, while less is known about the processes that occur during annealing, as it becomes evident from the large number of different models proposed. One further aim of this work is to clarify processes that occur during annealing and to investigate the optical damage suppression ability of annealing treatments. That is why the knowledge about annealing of LiNbO_3 crystals is reviewed in the following section.

2.3 Annealing

2.3.1 Annealing behavior of undoped lithium niobate

The melting point of undoped LiNbO_3 is about 1250 °C. The phase diagram can be seen in Fig. 2.6 [10]. Most crystals are grown in the congruently melting crystal composition, i.e., the composition of the crystal and the melt, from which the crystal is grown, are identical and remain constant during the whole growth process. In that case the lithium concentration is 48.38 mol% (Specification by Crystal Technology, Inc., but values between 48.3 and 48.6 mol% can be found in the literature [76–78]). According to Fig. 2.6 congruently melting LiNbO_3 can form a second crystal phase at temperatures below 910 °C, a mixture between lithium niobate and lithium triniobate (LiNb_3O_8). At temperatures above 300 °C LiNb_3O_8 starts to grow around surface scratches if present [79]. While this process takes many days at 300 °C, the formation of LiNb_3O_8 becomes more rapid with increasing temperature. At 600 °C segregation is found within 1 week and at 750 °C after 1 day of annealing [79,80]. The maximum of LiNb_3O_8 growth is found around 800 °C [81]. At higher temperatures above 910 °C LiNb_3O_8 disappears from the surface. The segregation process is independent of the atmosphere, but becomes weaker with increasing crystal stoichiometry [81]. LiNb_3O_8 can also form in the crystal bulk close to crystal defects, but this has been observed only after longtime treatments of one week at 780 °C [79]. The formation of LiNb_3O_8 takes place according to the reaction:



The excess of Li^+ ions pushes the LiNbO_3 crystals closer to stoichiometry [80]. It has been observed that the segregation of LiNb_3O_8 is suppressed if the LiNbO_3 crystals are free of hydrogen impurities [82,83].

Additionally a surface layer consisting of HNbO_3 can form if LiNbO_3 is annealed above

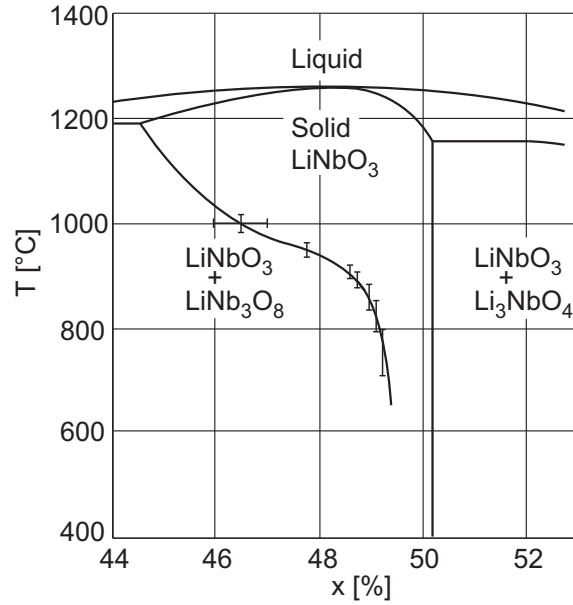


Figure 2.6: Phase diagram of the $\text{Li}_2\text{O} - \text{Nb}_2\text{O}_5$ system. The $c_{\text{Li}}/(c_{\text{Li}} + c_{\text{Nb}})$ concentration ratio is denoted by x [10].

600 °C depending on the humidity of the surrounding atmosphere [84,85].

Self diffusion At elevated temperatures the ions which LiNbO_3 consists of become mobile. Activation energies E_A and diffusion constants D_0 of Li^+ , Nb^{5+} , and O^{2-} are summarized in Tab. 2.2 [86]. The mobility μ of the ions can be calculated from these data using

$$\mu = \frac{\sigma}{eN} = D_0 e^{\frac{-E_A}{k_B T}}, \quad (2.16)$$

where σ is the electrical conductivity, e the elementary charge, N the concentration of the mobile charge carriers, k_B the Boltzmann constant, and T the absolute temperature. As it can be seen, lithium is the most mobile ionic species at typical annealing temperatures because of the large diffusion constant D_0 .

These data vary in the literature within a very broad range. For a better comparison all data presented in Tab. 2.2 are measured with a tracer method. For lithium ions the variations are particularly large: D_0 varies between 10^{-2} and $10^3 \text{ cm}^2/\text{s}$ and E_A between 1.17 and 3.24 eV depending on the method used, because for many methods interaction with

	D_0 [cm ² /s]	E_A [eV]
Li ⁺	4.7×10^0	1.98
Nb ⁵⁺	2.0×10^{-7}	1.07
O ²⁻	3.0×10^{-6}	1.27

Table 2.2: Diffusion constants D_0 and activation energies E_A for self diffusion in LiNbO₃ [86].

other species, that have to diffuse to balance the charge, influences the results drastically.

Ferroelectric domains LiNbO₃ changes from its ferroelectric phase to its paraelectric phase at the Curie Temperature $T_C = 1142.3$ °C. When a single-domain LiNbO₃ crystal is heated above this point it becomes multi domain. When a periodically-poled LiNbO₃ crystal is heated up, domain patterns with small period lengths of several micrometers that are typically needed for SHG devices remain stable until temperatures of 1000 °C [87]. At higher temperatures their shape is distorted, and at 1100 °C the domain pattern disappears.

2.3.2 Annealing behavior of doped lithium niobate

Doped lithium niobate shows a lot of additional changes in crystal properties during annealing. Most of the time this behavior is governed by the influence of the dopants. That is why important dopant properties have to be considered.

2.3.2.1 Multivalent dopant ions and defects

Multivalent dopants play a key role as photorefractive sensitizers in lithium niobate. The most prominent dopant is iron (Fe) that occurs as Fe²⁺ and Fe³⁺ [88]. It occupies only lithium sites even for the highest possible doping levels of several percent [89]. The Fe^{2+/3+} states are located energetically within the band gap of LiNbO₃. Light can excite electrons from Fe²⁺ to the conduction band. The resulting absorption for visible light can be used to determine the concentration of Fe²⁺ [88]:

$$c_{\text{Fe}^{2+}} = 2.16 \times 10^{21} \text{m}^{-2} \alpha_{477 \text{ nm}}^0. \quad (2.17)$$

Here $c_{\text{Fe}^{2+}}$ denotes the concentration of Fe²⁺ ions and $\alpha_{477 \text{ nm}}^0$ the absorption coefficient for ordinary light polarization (i.e. polarization perpendicular to the c -axis) at the wavelength 477 nm. An absorption spectrum of an iron-doped lithium niobate crystal is shown in Fig. 2.7. A second absorption peak can be seen in the infrared part of the spectrum be-

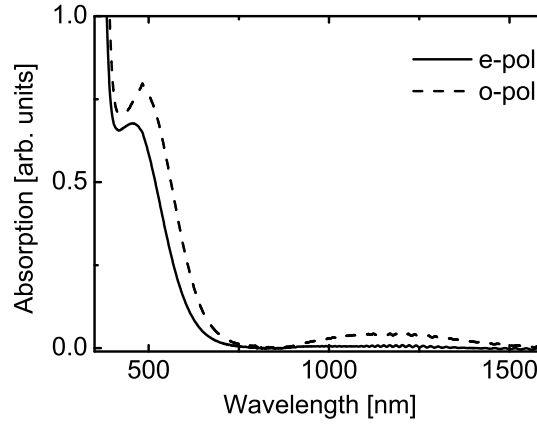


Figure 2.7: Absorption spectrum of an iron-doped LiNbO_3 crystal.

tween 1000 and 1500 nm. Its origin is the internal Fe^{2+} transition ${}^5T_2 - {}^5E$ $d-d$ [88]. The concentration of Fe^{3+} ions $c_{\text{Fe}^{3+}}$ is not determined by absorption spectroscopy, because the peaks at light wavelengths $\lambda = 483$ and 420 nm, that belong to spin-forbidden $d-d$ transitions of Fe^{3+} , are very weak and the $\text{O}^{2+} - \text{Fe}^{3+}$ transition starting to absorb at 400 nm is superimposed by the band edge [11]. But it can be calculated by $c_{\text{Fe}^{3+}} = c_{\text{Fe}} - c_{\text{Fe}^{2+}}$. The total iron concentration c_{Fe} can be determined by, e.g., atomic absorption spectroscopy (AAS).

Other multivalent dopants behave similar [11]: Copper ($\text{Cu}^{+/2+}$) [90], manganese $\text{Mn}^{2+/3+/4+}$ [91, 92], and titanium $\text{Ti}^{3+/4+}$ [11] are widely used. The intrinsic niobium antisite defects can also occur as $\text{Nb}_{\text{Li}}^{4+/5+}$ [11]. All these ions differ in the incorporation sites and their states in the energy levels within the band gap (Fig. 2.8). Manganese has the deepest energy level, followed by copper, iron, titanium, and niobium on lithium site [11]. For excitation from deeper levels more energy is required. The possible excitation and charge transport processes that can occur during annealing under various conditions are now considered in detail.

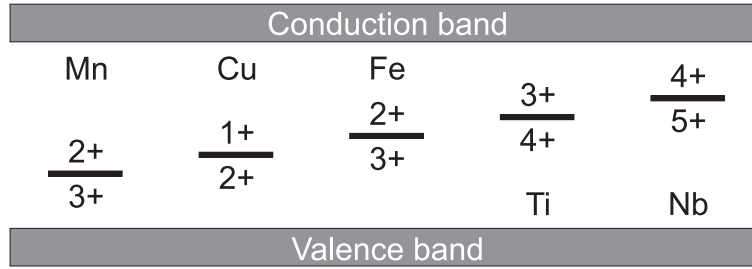


Figure 2.8: Band scheme of doped lithium niobate. Various bivalent dopants form electronic states at different energy levels.

2.3.2.2 Excitation and charge transport processes

Electrons from the multivalent dopant ions can be excited to the conduction band and can be transported by different mechanisms. The most important mechanisms are summarized schematically in Fig. 2.9.

- Electrons can be excited by light with sufficient energy $E = h\nu$ to the conduction band. Due to the bulk photovoltaic effect the resulting current is mainly directed along the c -axis. The current density is given by $j_{\text{phv}} = \beta^* N^- I$ (see section 2.2.2.1).
- Thermal excitation of electrons is often negligible at room temperature, but can have significant influence if LiNbO_3 is annealed. The thermal conductivity holds $\sigma_{\text{th}} = \sigma_{\text{th},0} e^{-E_A/(k_B T)}$ with $\sigma_{\text{th},0}$ constant, k_B the Boltzmann constant and T the absolute temperature. The thermal activation energy for excitation of electrons from Fe^{2+} to the conduction band is about $E_A = 1.4$ eV [93].
- At high doping levels tunneling between filled and empty centers becomes relevant as charge transport process. In the case of iron doping it becomes the dominant charge transport process at room temperature for doping levels larger than 0.05 % Fe_2O_3 [94]. The tunneling conductivity σ_{tu} is given by

$$\sigma_{\text{tu}} \propto N_{\text{eff}} \exp\left(-\frac{a}{\sqrt[3]{c_{\text{Fe}}}}\right) \quad (2.18)$$

with the effective trap density N_{eff}

$$N_{\text{eff}} = \frac{c_{\text{Fe}^{2+}} c_{\text{Fe}^{3+}}}{c_{\text{Fe}}}. \quad (2.19)$$

Here $a > 0$ denotes a constant.

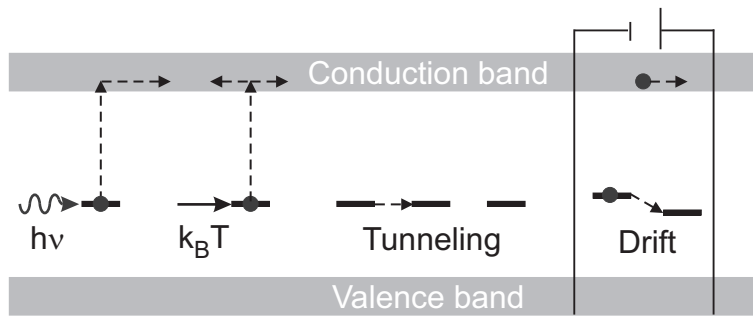


Figure 2.9: Band scheme of lithium niobate. The most important electronic excitation and transfer processes are shown schematically.

- Drift currents are possible in the conduction band as well as between adjacent centers at high doping levels. The drift current density holds $j_{\text{Drift}} = \sigma E$ with σ as total conductivity and E as electrical field.

Additionally, thermally activated drift and diffusion of ionic charge carriers take place (see section 2.3.1 and Tab. 2.2).

Random free energy barrier model The conductivity of many disordered materials can be described within the framework of the "Random free energy barrier model" [95]. For LiNbO_3 with its several percent of crystal defects like Li vacancies and Nb_{Li} antisite defects the model should be applicable. It considers charge transport in a spatially randomly varying potential landscape as it is shown in Fig. 2.10. The frequency dependence of the

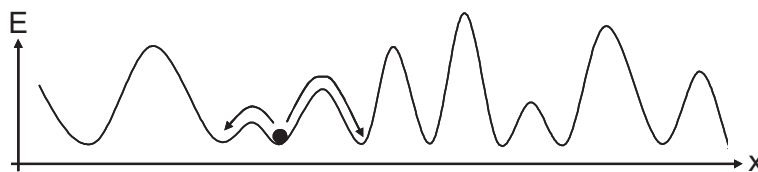


Figure 2.10: Schematic of the charge transport in a randomly varying potential landscape.

conductivity $\sigma(\omega)$ on an electric AC field is derived in [95] to be:

$$\sigma(\omega) = \frac{\sigma_0 \omega \tau_e \arctan(\omega \tau_e)}{\frac{1}{4} \ln^2(1 + \omega^2 \tau_e^2) + [\arctan(\omega \tau_e)]^2}. \quad (2.20)$$

Here σ_0 denotes the DC conductivity and $1/\tau_e$ can be interpreted as the frequency, where the conductivity changes from its frequency-independent DC part to its frequency-dependent AC part.

2.3.2.3 Reduction

During a reducing annealing treatment multivalent dopant ions and crystal defects are transferred from the valence state $n + 1$ to the state n , e.g., $\text{Fe}^{3+} \rightarrow \text{Fe}^{2+}$. The occurring processes during reduction and their activation energies are topic of a still vivid discussion for the last 40 years. The entire discussion cannot be reviewed in this work, but instructions from the literature for the reduction of LiNbO_3 as well as the most important theories are considered.

The first systematic study on reduction was performed by Phillips and Staebler in 1974 [96]. It is described that iron can be reduced in LiNbO_3 by annealing the crystals in argon or hydrogen atmosphere as well as in vacuum at temperatures between 800 and 1150 °C. Conversion of 90 % of Fe^{3+} to Fe^{2+} has been observed for annealing at 1150 °C in argon. The crystals can also be annealed in Li_2CO_3 powder at 450 to 600 °C for strong reduction (> 95% Fe^{2+}). Other compounds (Li_2SiO_3 , LiAlO_2 , LiF , Na_2CO_3) lead to similar results.

Reduction leads to strong changes of the absorption in doped LiNbO_3 crystals [97], because the absorption depends on the valence state of the ions, e.g., in the case of Fe doping, reduction increases the absorption in the visible and the infrared parts of the spectrum. By this means the degree of reduction can be determined (see Eq. (2.17)) [88, 90]. It has been observed that Mn ions start to reduce at temperatures between 200 and 300 °C and Cu ions between 400 and 500 °C. Fe starts to reduce above 600 °C and Ti above 650 °C [98] (compare to Fig. 2.8).

In undoped samples reduction also increases absorption and electrical conductivity drastically [99–101]. The dependence of the absorption and the conductivity on the annealing parameters are considered in detail in the following.

Electrical conductivity The saturation value of the electrical conductivity depends linearly on $p_{\text{O}_2}^{-1/4}$ where p_{O_2} is the partial pressure of oxygen in the surrounding atmosphere during annealing [99–101]. The exact dependence is given by an Arrhenius-type function [99]:

$$\sigma_e = 3.83 \times 10^4 p_{\text{O}_2}^{-1/4} \exp\left(-\frac{E_A}{k_B T}\right) \quad (2.21)$$

Here σ_e denotes the conductivity due to the electrons, k_B the Boltzmann constant, and T the absolute temperature. For the activation energy E_A the value 2.12 eV is given in [99] whereas in [101] a value of 1.5 eV is determined. This equation is valid for oxygen partial pressures $p_{O_2} < 10^{-3}$ hPa. At larger oxygen partial pressures the conductivity saturates to the value of the ionic conductivity, because of a lack of mobile electrons.

Absorption When an undoped LiNbO_3 crystal is reduced, several broad absorption peaks can occur around 380, 500, and 760 nm light wavelength depending on the treatment [11, 102]. The absorption around 500 nm as a function of the electrical conductivity has been measured in Refs. [101, 103]. The following expression for the saturation value of the absorption α measured after annealing is given in [103, 104] according to the theory given in [105]:

$$\alpha = \frac{\sigma_0}{nc\epsilon_0} \frac{\sinh(\hbar\omega\pi/k_B T)}{(\hbar\omega\pi/k_B T)} \exp\left(-\frac{\hbar^2\omega^2\pi^2}{4E_A k_B T}\right) \quad (2.22)$$

Here σ_0 denotes the DC conductivity, n the refractive index, c the light velocity, ϵ_0 the vacuum permittivity, \hbar the reduced Planck constant, and ω the angular frequency of the incident light. The experimentally determined value for the activation energy is $E_A = 0.51$ eV [103]. In [101] measurements of the absorption versus the annealing temperature lead to $E_A = 1.2$ eV.

The absorption build-up dynamics have been analyzed in [106]. The time dependence of the absorption can be described within the framework of a diffusion model from [107]:

$$\Delta A(t) = \beta N_0 d \left[1 - \frac{8}{\pi^2} \sum_{k=0}^{\infty} \frac{1}{(2k+1)^2} \exp\left(-D \frac{(2k+1)^2 \pi^2}{d^2} t\right) \right]. \quad (2.23)$$

Here $\Delta A(t)$ denotes the time dependent optical density change, i.e., A is given by $A = \log(I_0/I)$. The crystal thickness is denoted by d , D is a diffusion coefficient, N_0 is the equilibrium concentration of the diffusing substance, and β is given by $\beta = \sigma_\alpha / \ln 10$ with σ_α the absorption cross section. The activation energy E_A for the diffusion coefficient D is observed to be 3.6 eV.

The microscopic processes occurring during reduction have been discussed in the literature since the first reduction experiments in 1974. It is commonly assumed that oxygen ions leave LiNbO_3 . The formation of the absorption bands is explained by two different models [11, 104]:

- Nb_{Li} ions are reduced from the valence state 5+ to 4+ forming polarons with an absorption peak around a wavelength of 760 nm. These polarons are instable at room temperature and couple with $\text{Nb}_{\text{Nb}}^{4+}$ to bipolarons that absorb light around

500 nm wavelength. The dissociation energy is found to be 0.27 eV [11,108]. The peak at 380 nm is not explained [11].

- Color centers are formed by the out-diffusion of oxygen [11,102]. The oxygen vacancies can be occupied by one or two electrons (F^+ , F centers). The absorption band around 500 nm is attributed to F centers and the peak at 380 nm to the F^+ centers.

2.3.2.4 Oxidization

Early reports of oxidization of multivalent dopant ions in lithium niobate, i.e., the change of the valence state from n to $n + 1$, reach back to the late 60's and early 70's of the 20th century. Since then it is common sense that oxidization takes place when a LiNbO_3 crystal is heated up to 800-1100 °C in oxygen atmosphere for 5-24 h (see e.g. [30,73,96,97,99,101,106,109,110]). In [109] it is observed that LiNbO_3 can also be oxidized in Nb_2O_5 powder. Oxidization can reverse absorption and conductivity changes that occur during reduction.

The first systematic study of the oxidization dynamics was performed in 2007 by Sugak et al. [106]. An equation analogous to Eq. (2.23) could not be fitted to the observed evolution of the absorption changes.

Similar results are obtained for various crystal materials like BaTiO_3 or $\text{KTaNbO}_3\text{:Cu}$ [111,112].

2.3.2.5 Annealing in the presence of an electrical field

Externally applied electrical field In 1967 Levinstein et al. annealed LiNbO_3 in the presence of an externally applied electric field for the first time [71,113]. The electric field was applied via gold electrodes. The crystals are observed during the annealing treatment with a polarizing microscope and it could be seen that an interference fringe pattern forms at the anode and progresses slowly to the cathode with a velocity of 0.1 cm/min if an electrical field of 250 V/cm is applied at a temperature of 700 °C. At the same time the electrical conductivity of the LiNbO_3 crystal decreases. It has been observed that behind this front the optical damage of the crystal is reduced. A similar treatment at 400 °C with an electrical field of 1000 V/cm is able to remove color changes caused by strong reduction. The microscopic origin of these effects is rather unclear. In [71–73] different arguments are presented considering drift of gold, hydrogen, and iron, but proofs are still missing. In recent field-annealing experiments the behavior of the LiNbO_3 crystals has been studied depending on the electrode material. In [114] a lithium supporting ceramic is chosen as the anode (LiSiPO_8). Platinum is used as the cathode. By this means at temperatures of 700 °C lithium ions can drift from the anode into the crystal while for charge compensation electrons drift from the cathode into the crystal. Therefore the LiNbO_3 is reduced and

the stoichiometry is changed. A color change is observed that has a step-like profile in the crystal. The front between dark and bright fractions of the crystal moves from one electrode to the other [115,116]. The electrical conductivity of the LiNbO_3 crystal increases during the lithium injection. A flip of the polarity of the electric field reverses the effects and reoxidizes the crystal.

This process of reversible color change caused by an externally applied electrical field is often called "electrochromism" or "electrocoloration". The same behavior is also known from other materials [117]. Possible applications are displays or windows with tunable transmission.

Internal electrical field An internal electrical space charge field can also serve as the driving force for ions during annealing. This process is called "thermal fixing", because it is used to stabilize holograms that are written by light [118]. An interference light pattern – for simplicity it is assumed to be sinusoidal – illuminates the crystal. Due to the bulk-photovoltaic effect charges are redistributed leading to a sinusoidally modulated concentration of Fe^{2+} and consequently Fe^{3+} . The resulting space-charge field forces hydrogen and lithium ions to move while the crystal is annealed at 150-250 °C, temperatures where the ions become mobile. Finally, the concentrations of hydrogen and lithium ions have a sinusoidal shape. Holograms that are thermally fixed can persist hundreds of years until their final decay. An overview about thermal fixing is given in [93].

Chapter 3

Oxidization

3.1 Experimental methods

3.1.1 Crystals

Most crystals that are used in this work are supplied by Crystal Technology, Inc., CA, USA, otherwise it is mentioned. Crystal Technology succeeded in growing LiNbO_3 crystals with iron doping of several percent Fe_2O_3 for the first time. Boules with nominal doping levels of 0.05, 0.5, 1.0, 2.0, 3.0, and 4.0 wt% Fe_2O_3 were grown from a melt of congruent composition. In the following they are labeled with 0.05, 0.5, 1.0, 2.0, 3.0, and 4.0 % Fe. The distribution coefficient of iron in LiNbO_3 is less than one at high doping levels. The iron concentrations in the crystals are determined with the help of atomic absorption spectroscopy (AAS). The growth of crystals with such high doping levels becomes more challenging with increasing doping level especially above 2.0 % Fe. Crystal Technology succeeded in growing a small boule of LiNbO_3 with 3.0 % Fe (about 4 cm in diameter and 0.7 cm thick). The boule with a doping level of 4.0 % Fe grew as a spiral instead of a cylinder. In that case the direction of the crystallographic c -axis and the x -axis which is perpendicular to the c -axis has not been determined before cutting and therefore it is not parallel to the edges of the samples. For all other samples the direction of the c -axis is well known. X -cut samples, i.e., samples whose large crystal faces are perpendicular to the x -axis, were cut from all boules to have a size of $1 \times 6 \times 8 \text{ mm}^3$ or $1 \times 10 \times 8 \text{ mm}^3$. In some cases other dimensions and z -cuts are used.

3.1.2 Oxidization methods for multivalent dopant ions in lithium niobate

3.1.2.1 Conventional oxidization

For 40 years an oxidization setup for LiNbO_3 crystals is known [71, 73]. It is referred to as "conventional oxidization". The setup is schematically shown in Fig. 3.1. The LiNbO_3 crystals are placed on a ceramic plate that is covered with platinum foil to prevent from surface damages of the crystal. The samples are heated up to 800-1000 °C in oxygen atmosphere or an atmosphere with increased oxygen partial pressure compared to that of air. After some hours at least a part of the multivalent ions are oxidized.

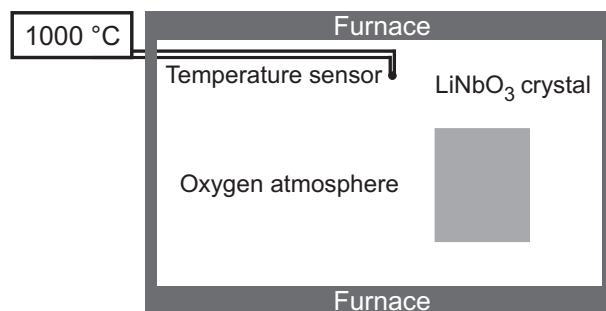


Figure 3.1: Schematic of the conventional oxidization setup.

3.1.2.2 Thermo-electric oxidization

A setup is built inspired by Refs. [71–73] in order to investigate the effect of electrical fields on the oxidization state of multivalent impurities in LiNbO_3 at elevated temperatures. A schematic of the setup can be seen in Fig. 3.2. The crystals can be heated up to temperatures of 900 °C in the presence of an externally applied electrical field. The samples are placed in the middle of a tube furnace (length 1.6 m) with a very homogeneous temperature profile due to three zones with independent heating and temperature control. The tube consists of quartz glass and has a diameter of 3.0 cm. A DC voltage of up to 3000 V can be applied with the help of gold paste electrodes. Two types of gold paste are used: Gold paste from the company Ferro, Hanau, Germany. Since this paste is no longer commercially available, gold paste is mixed consisting of 66 % gold powder, >27 % dibutyl phthalate and <7 % 1-ethoxypropan-2-ol as solvent. With the amount of the solvent the viscosity can be adjusted. It has turned out that much less solvent is sufficient for the use

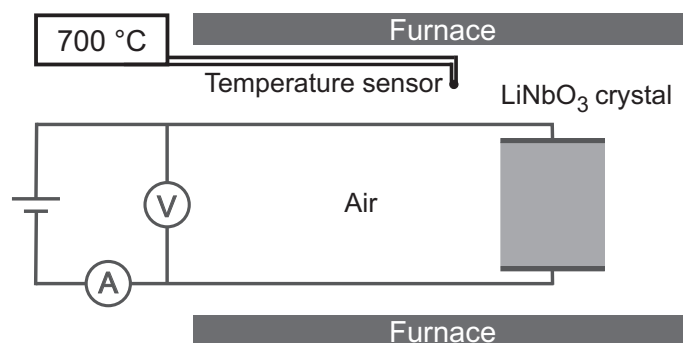


Figure 3.2: Schematic of the thermo-electric oxidization setup.

as electrodes. This mixture has similar properties to the gold paste by Ferro. Both fulfill the most important requirements:

- Adhesion to LiNbO₃ and to the wires at room temperature as a suspension as well as at elevated temperature as a solid compound
- Stability up to temperatures of 900 °C
- Large electrical conductivity at room temperature as well as at elevated temperatures, i.e., the paste has to dry at room temperature. This distinguishes the gold paste used from most standard gold pastes that exhibit significant electrical conductivity not until drying at 800 °C.

The wires in the furnace consist of an alloy of nickel and aluminum that is chemically stable enough to persist several month at 700 °C in air and at least one experiment at 900 °C.

Nickel and aluminum as well as gold are indeed able to diffuse into the crystal, but they can reach a depth of only several micrometers below the surface under typical experimental conditions [86, 119, 120].

The current can be limited to values between 0.1 and 10 mA. When the current limit is reached, the voltage is automatically decreased by the power supply. The evolution of voltage and current is recorded. Heating and cooling ramps of 0.1 to 6 °C/min can be used. These limits are set by the temperature controller and the stability of the tube, respectively. The sample holder is made of Duratec 750 ceramic. Duratec 750 withstands much higher temperatures than used in experiments, is chemically inactive, and exhibits no significant electrical conductivity at 700 °C. By this means leakage currents are avoided.

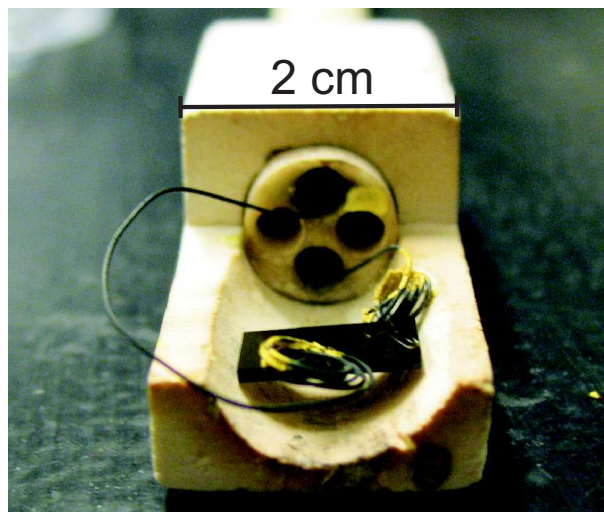


Figure 3.3: Photograph of an iron-doped LiNbO_3 crystal (black) in the white crystal holder. The contact area of the crystal and the holder is minimized by construction. The wires that are used to contact the sample electrically are covered with rests of gold paste.

The crystal is mounted in such a way that the contact area to the holder is minimized as shown in Fig. 3.3.

In-situ observation of the thermo-electric oxidation To observe the crystals during the treatments a special second furnace is constructed. It consists of two crossing quartz glass tubes (lengths 0.6 m, diameter 3.2 cm) that are enveloped by heating wires and thermally isolating materials. A schematic of this furnace is shown in Fig. 3.4. This furnace can reach temperatures of up to 900 °C. The temperature profile is not very homogeneous in the crossing region, because no heating wires can be attached there. The temperature varies by 10 °C between the center of the cross and the region, that is surrounded by the heating wires, in 2 cm distance. While one of the two crossing tubes is used for the sample holder the other tube is employed for observations with a digital camera that takes one picture every minute. The camera has a rather small distance of 40 cm to the crystal. The temperature at the end of the tubes is below 100 °C, so neither the camera can be damaged nor air turbulences arise. The furnace can be heated with up to 10 °C/min, limited by the stability of the tubes. The construction of the sample holder is comparable to the holder that is described in the section before. The only difference is that the crystal stands freely on the holder instead of lying for better observation. A similar high voltage power supply

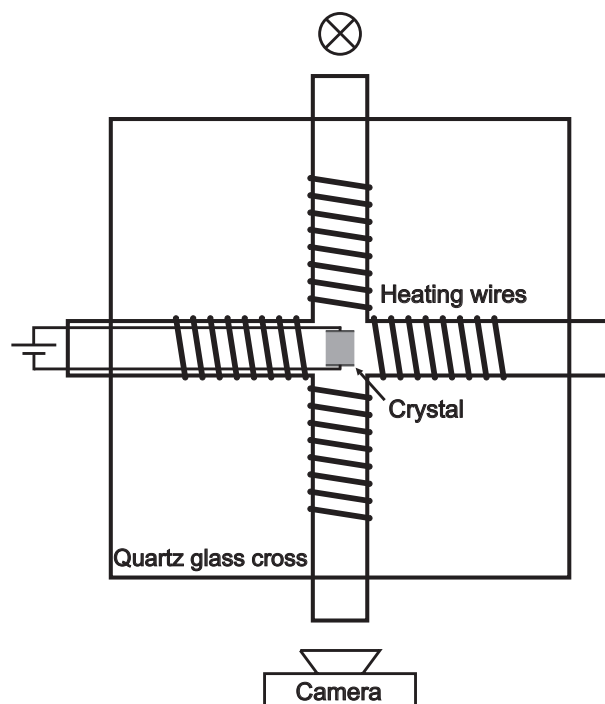


Figure 3.4: Schematic of the furnace that is constructed for in-situ observation of the crystal during annealing.

and the same gold paste are used.

3.1.3 Determination of the Fe^{2+} concentration

3.1.3.1 Absorption spectroscopy

The concentration of Fe^{2+} in the LiNbO_3 crystal can be determined by measuring the absorption of ordinarily polarized light of the wavelength $\lambda = 477$ nm according to Eq. (2.17). A Cary 500 spectrophotometer from Varian, Inc. is used to determine absorption spectra from $\lambda = 300$ to 3200 nm. The largest optical densities that can be measured are $A = \log(I_0/I) = 5$. The absorption values are corrected for reflection losses applying the Sellmeier equation for undoped congruently melting LiNbO_3 .

3.1.3.2 Conductivity spectroscopy

Principle of the method Since the electronic transport between Fe^{2+} centers dominates the charge transport in iron-doped LiNbO_3 crystals with doping levels $c_{\text{Fe}} > 0.05\%$ at room temperature [94], conductivity spectroscopy can be used to determine the Fe^{2+} concentration. The principle of this method is shown in Fig. 3.5. An AC voltage

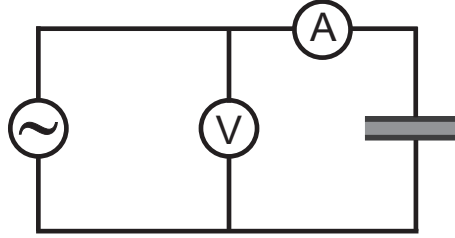


Figure 3.5: Principle of conductivity spectroscopy, also called dielectric spectroscopy. A frequency-dependent AC voltage is applied to a sample while the evolutions of voltage and current are monitored.

$U^*(\omega) = U'(\omega) + iU''(\omega)$ with the frequency ω is applied to the sample, and the amplitude and the phase shift of the corresponding current $I^*(\omega) = I'(\omega) + iI''(\omega)$ are measured. The star indicates complex quantities with real part ($'$) and imaginary part ($''$). The imaginary unit is denoted by i . The impedance is calculated by $Z^*(\omega) = U^*(\omega)/I^*(\omega)$. The complex conductivity $\sigma^*(\omega) = \sigma'(\omega) - i\sigma''(\omega)$ (please note the commonly used minus sign between real and imaginary part of the conductivity) is given by

$$\sigma^*(\omega) = \frac{1}{Z^*(\omega)} \frac{d}{A_{\text{el}}}. \quad (3.1)$$

Here d denotes the distance of the electrodes and A_{el} the electrode area.

Sample preparation The crystals that are used for conductivity spectra measurements are x -cuts and have dimensions of $0.1 - 0.6 \times 11 \times 11 \text{ mm}^3$. The use of z -cuts is avoided, because they exhibit strong pyroelectric currents, i.e., currents that flow as soon as the crystal temperature is changed, which disturb temperature dependent measurements. The electrodes are evaporated to the large surfaces, i.e., $A_{\text{el}} = 10 \times 10 \text{ mm}^2$ and $d = 0.1 - 0.6 \text{ mm}$. The electrodes consist of two layers: chromium (Cr, 10 nm thickness) and gold (Au, 100 nm thickness). The chromium leads to a better adhesion of the gold layer to the crystal surface. The evaporation is performed at elevated temperatures of 280-300 °C to minimize the

water layer that covers all oxide materials. From [121] it can be estimated that chromium can diffuse less than one micrometer into the crystal at temperatures up to 700 °C for typical timescales.

Spectrometer and measurement chamber The conductivity spectra are measured with the Alpha AL spectrometer from Novocontrol. Frequencies from 3×10^{-6} to 3×10^5 Hz can be set. The measurable capacities range from 10^{-15} to 1 F and the measurable conductivities from 5×10^{-15} to $100 \Omega^{-1}$. An external voltage with the amplitude 1 V is applied. A self-constructed heatable measurement chamber is used. A schematic of this chamber can be found in Fig. 3.6. The electrodes of the LiNbO_3 samples are connected

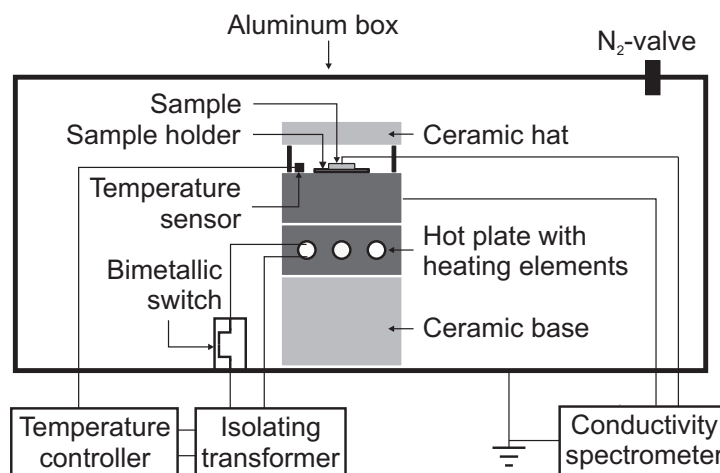


Figure 3.6: Schematic of the measurement chamber for conductivity spectroscopy.

to the conductivity spectrometer. The top electrode is glued to the wire by silver paste, the bottom electrode to the sample holder. Screws fix the sample holder to the steel plate below. This steel plate is wired to the spectrometer. In the hot plate below three heating elements with each 125 W heating power heat the sample up to 720 °C. They are connected to the power supply via an isolating transformer. By this means noise from external cables is reduced, and grounding of the hot plate can be avoided. Grounding would necessitate to isolate the hot plate from the steel plate. That would lead to reduced thermal conductivity and lower temperatures at the sample. The heating elements are controlled by a temperature controller "2408" from Eurotherm. The associated temperature sensor is attached close to the sample (1.5 cm away). The temperature stability is ± 0.5 °C. A ceramic base and a ceramic hat consisting of Duratec 750 isolate the metal parts from the surrounding

aluminum box that is grounded and shields the setup from electromagnetic noise. The free space in this box is filled with isolating fleece. The ceramic hat also prevents the fleece from touching the sample. If the aluminum box reaches temperatures above 100 °C, a bimetallic switch will turn off the heaters for security. A valve in the box can be opened to flood the interior with nitrogen gas. This suppresses the corrosion of the steel parts in the measurement chamber.

3.1.4 Birefringence changes

Optical inhomogeneities often show up as birefringence inhomogeneities that can be measured by the Sénarmont compensator method. It is named after the french physicist H. H. de Sénarmont (1808 - 1862) [122]. It is often referred to similar techniques as "compensator setup" or "ellipsometry". A schematic of the setup is shown in Fig. 3.7. A red laser beam

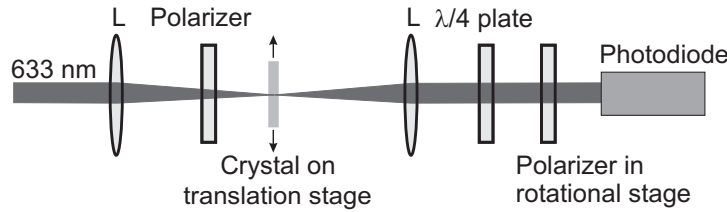


Figure 3.7: Schematic of the Sénarmont compensator setup. The abbreviation "L" represents a lens.

of a helium-neon laser (HeNe) with a wavelength of 633 nm is focussed into the crystal (beam diameter $2\sigma = 17 \mu\text{m}$, light intensity $I = 3 \text{ W/cm}^2$). The polarizer in front of the crystal polarizes the laser beam at an angle of 45° with respect to the crystallographic c -axis. By this means the crystal is birefringent for the incident red light. Consequently, the light polarization changes inside the crystal from linear to elliptic. A second lens behind the crystal transforms the laser beam into a plane wave for a proper function of the quarter-wave plate. One of the two axes of this quarter-wave plate is parallel to the light polarization in front of the sample. Thus any elliptic polarization turns back into linear polarization, but generally with a different plane of polarization compared to that of the input polarization (see Appendix A and [15]). The direction of the polarization is determined with a polarizer (analyzer) in a rotational stage and a photodiode. In order to get precise data about the rotation of the polarization plane, the intensity of the transmitted beam is detected for various angles of the analyzer, and afterwards a sinusoidal function is fitted to the data. By the phase difference β of sinus waves measured at different positions

in the crystal, birefringence changes $\Delta(n_e - n_o)$ between these positions can be determined

$$\Delta(n_e - n_o) = \frac{\beta\lambda}{2\pi d} . \quad (3.2)$$

Here d denotes the crystal thickness and λ the vacuum wavelength of the HeNe laser beam. Furthermore, the crystal can be shifted perpendicularly to the HeNe laser beam and in parallel to the optical table, enabling lateral scans of birefringence changes. The minimum step size is $2.5 \mu\text{m}$. With the help of small steps ambiguities about the phase shift that can be induced by phase shifts larger than π can be avoided. For crystals of a thickness of 1 mm, birefringence changes as small as $\Delta(n_e - n_o) > 5 \times 10^{-6}$ can be detected. This limit is given by small temperature fluctuations of the LiNbO_3 crystal that lead to birefringence changes due to the thermo-optic effect [123]. If these fluctuations can be eliminated a detection limit for the birefringence changes of 5×10^{-7} will be feasible.

3.2 Experimental results

3.2.1 Iron concentration

The total iron concentration in the crystals, which can differ from the nominal concentration, i.e., the concentration of iron oxide (Fe_2O_3) in the melt, is measured by means of atomic absorption spectroscopy (AAS). The iron concentration is determined for the crystals doped with 0.5, 1.0, 2.0, and 3.0 wt% Fe_2O_3 in the melt. The results are shown in Tab. 3.1.

Doping level [wt% Fe_2O_3]	c_{Fe} [10^{26} m^{-3}]
0.5	1.29
1.0	2.35
2.0	3.85
3.0	5.00

Table 3.1: Nominal doping level and overall iron concentration c_{Fe} for highly iron-doped crystals.

3.2.2 Oxidization

Sample preparation Samples of all iron-doped crystals are heated up to 700 °C with a temperature change of $dT/dt = 3 \text{ °C/min}$. An electric field E_{max} of 125 V/mm is applied already before heating. A current limit is set corresponding to a current density of $j_{\text{max}} = 0.01 \text{ mA/mm}^2$. The temperature is kept constant for 6 hours, then cooling starts with $dT/dt = -3 \text{ °C/min}$. The voltage is not turned off before the temperature falls below 200 °C. The evolution of voltage and current during the annealing experiment is shown in Fig. 3.8. When the LiNbO_3 crystal is heated up, its conductivity increases. At temperatures typically between 500 and 600 °C the current limit is reached, and the voltage is decreased automatically. At 700 °C the electric field is lowered to only 2-10 V/mm. When the crystal is cooled down, its conductivity increases again and the voltage is restored to its former level.

Absorption changes Pictures of the crystals in the as-grown and the annealed state and the corresponding absorption spectra are shown in Figs. 3.9 and 3.10. In Fig. 3.9 (a) a photograph of an untreated LiNbO_3 sample doped with 2.0 % Fe is shown. The crystal looks black. The corresponding absorption spectrum in Fig. 3.10 (a) shows a strong

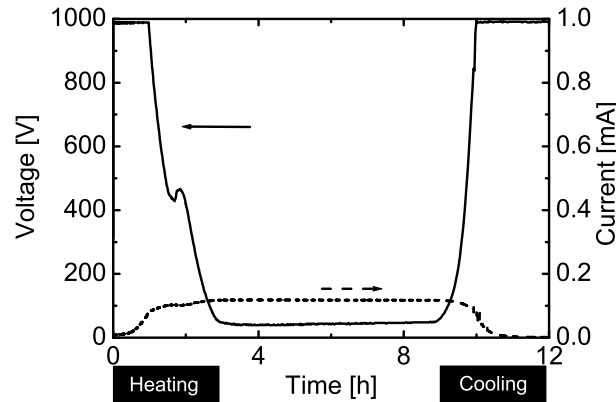


Figure 3.8: Evolution of voltage and current during an annealing experiment using a LiNbO_3 crystal doped with 2 wt% Fe_2O_3 .

absorption peak in the visible due to the large Fe^{2+} concentration. The crystals doped with 0.5, 1.0, and 3.0 % Fe look similarly black. Their absorption spectra are also shown in Fig. 3.10 (a). The absorption coefficients around 477 nm, belonging to absorption from Fe^{2+} , are higher than 10/mm. In order to measure that high absorption coefficients special crystals with a thickness of only 55 μm are utilized. After the annealing treatment all crystals become at least partially transparent. The absorption spectra of the annealed LiNbO_3 crystals are shown in Fig. 3.10 (b). In Fig. 3.9 (b) and (c) the samples with 0.5 and 1.0 % Fe are shown. The electrodes are attached to the left and the right side of the crystal. Some remains of the electrodes can be seen in the pictures. The black parts of the crystals at the left side are sections where the crystals are still dark. In the central part the transparent crystal is seen. It appears yellowish with two brownish horns ranging from the left, dark part to the right electrode. On the right part of the pictures the crystal appears black. This originates from surface precipitations. Below these precipitations the crystals are as transparent as in the central part. Absorption spectra of the transparent section are found in Fig. 3.10 (b). It can be seen that no more Fe^{2+} absorption is visible. The absorption coefficient around 477 nm is smaller than 1/mm. Only the internal Fe^{3+} transition causes the tiny, narrow peak around 483 nm. This means that the annealing treatment leads to a strong oxidization. Therefore in the following the annealing procedure is called "thermo-electric oxidization". In both crystals brown irregularities are found, mainly close to the dark part and in (c) close to the bottom. In Fig. 3.9 (d) and (e) photographs of

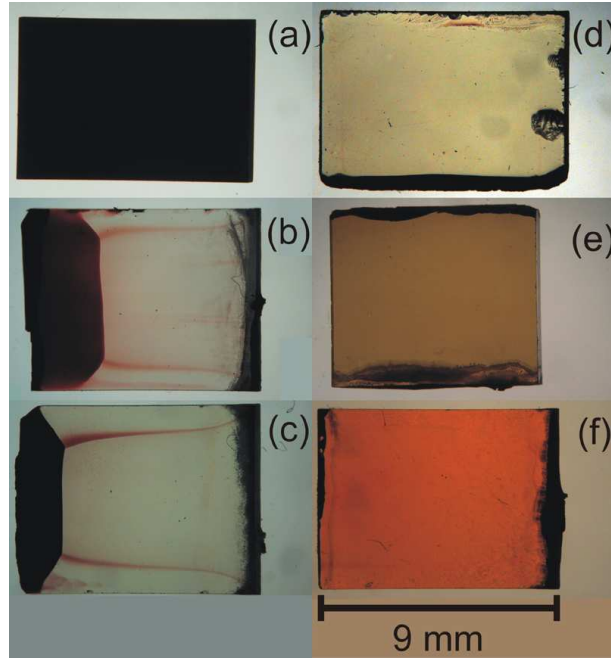


Figure 3.9: Photographs of the doped LiNbO_3 samples: (a) 2.0 wt% Fe_2O_3 in the as-grown state, (b)-(f) 0.5, 1.0, 2.0, 3.0, 4.0 wt% Fe_2O_3 after annealing.

the crystals doped with 2.0 and 3.0 % Fe are shown. The electrodes are attached to the bottom and the top of the crystals in these photographs. Here almost no dark sections and no inhomogeneities are visible. The color is remarkably darker. The absorption spectrum is shown in Fig. 3.10 (b). No absorption from Fe^{2+} centers is measurable. The Fe^{3+} peaks are larger compared to those of the samples that contain 0.5 and 1.0 % Fe. The absorption edge shifts remarkably to larger wavelengths. In Fig. 3.9 (f) a photograph of a treated crystal doped with 4.0 % Fe is shown. The electrodes are attached at the left and the right side of the sample. It appears brownish, but from the absorption spectrum in Fig. 3.11 it is obvious that this color does not come from residual Fe^{2+} , but from the Fe^{3+} absorption peak and the shifted absorption edge. The direction of the c -axis of the sample is not known, that is why the light polarization is arbitrary and no correction for reflection losses can be performed. Consequently in Fig. 3.11 the optical density $\log(I_0/I)$ (incident light intensity I_0 , intensity I of the transmitted beam) is shown instead of the absorption coefficient α . In Fig. 3.12 a conventionally oxidized LiNbO_3 crystal containing 2.0 % Fe is compared to a crystal in the as-grown state and a crystal that is thermo-electrically

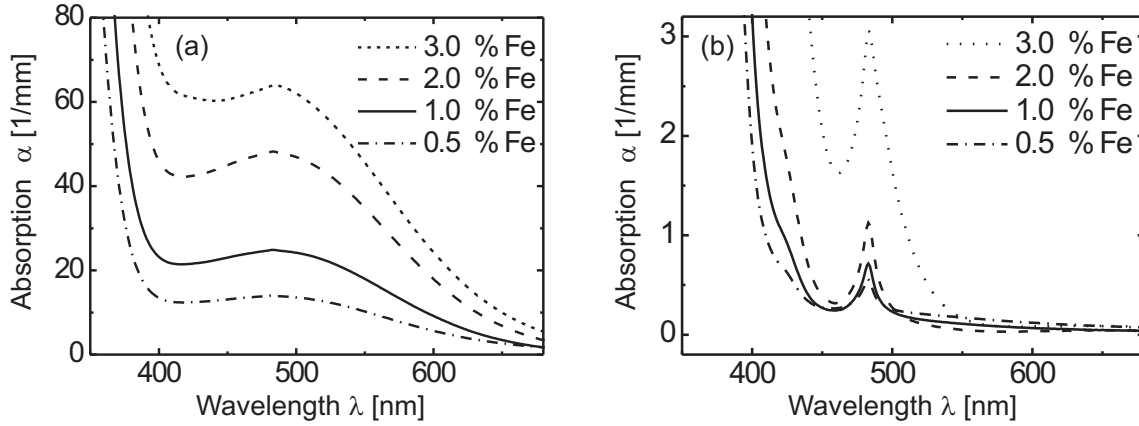


Figure 3.10: Absorption spectra for ordinarily polarized light of LiNbO₃ crystals doped with 0.5-3.0 wt% Fe₂O₃ (a) in the as-grown state and (b) after thermo-electric oxidization.

oxidized. It can be seen that the conventional oxidization technique is able to oxidize the highly iron-doped crystal, but only the thermo-electric oxidization leads to a nearly complete oxidization of iron.

Precipitations After the annealing precipitations and scratches can be seen on the crystal surface. A photograph of a crystal doped with 1.0 % Fe is shown in Fig. 3.13. These scratches were neither present before the annealing nor any tip was in contact to the sample. They show no preferred direction or length.

The precipitations on the surface are observed with the help of an atomic force microscope (AFM). The resulting pictures are shown in Fig. 3.14. Precipitations are present at the entire crystal surface, but near to the anode only islands show up whereas closer to the cathode the precipitations grow together and form a compact layer.

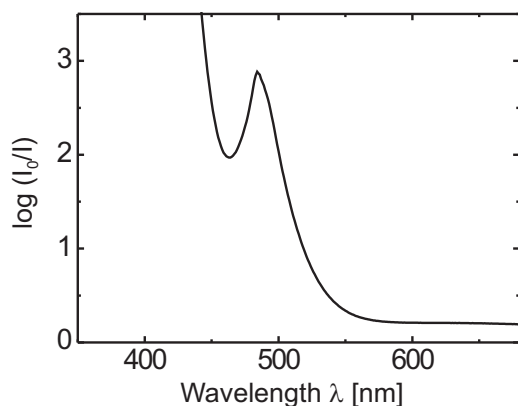


Figure 3.11: Optical density $\log(I_0/I)$ versus wavelength for a thermo-electrically oxidized LiNbO_3 crystal doped with 4.0 wt% Fe_2O_3 . The thickness of the sample is 1 mm.

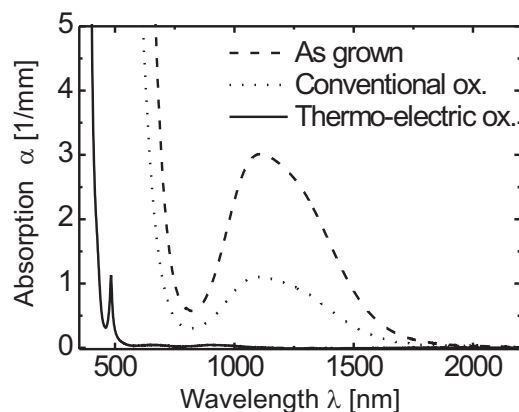


Figure 3.12: Absorption spectra for ordinarily polarized light of LiNbO_3 crystals doped with 2.0 wt% Fe_2O_3 in the as-grown state, the conventionally oxidized, and the thermo-electrically oxidized state.

3.2.3 Dynamics of the oxidation

3.2.3.1 Evolution of voltage and current

The evolution of the voltage and the current shows an anomalous behavior during the heating phase (Fig. 3.8). When the current limit is reached due to an increasing conductivity of

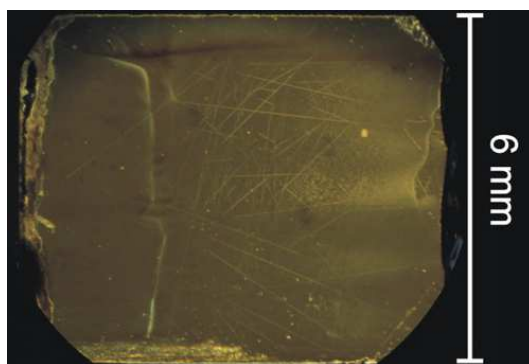


Figure 3.13: Photograph of a crystal which is doped with 1.0 wt% Fe_2O_3 . After annealing scratches can be seen on the surface.

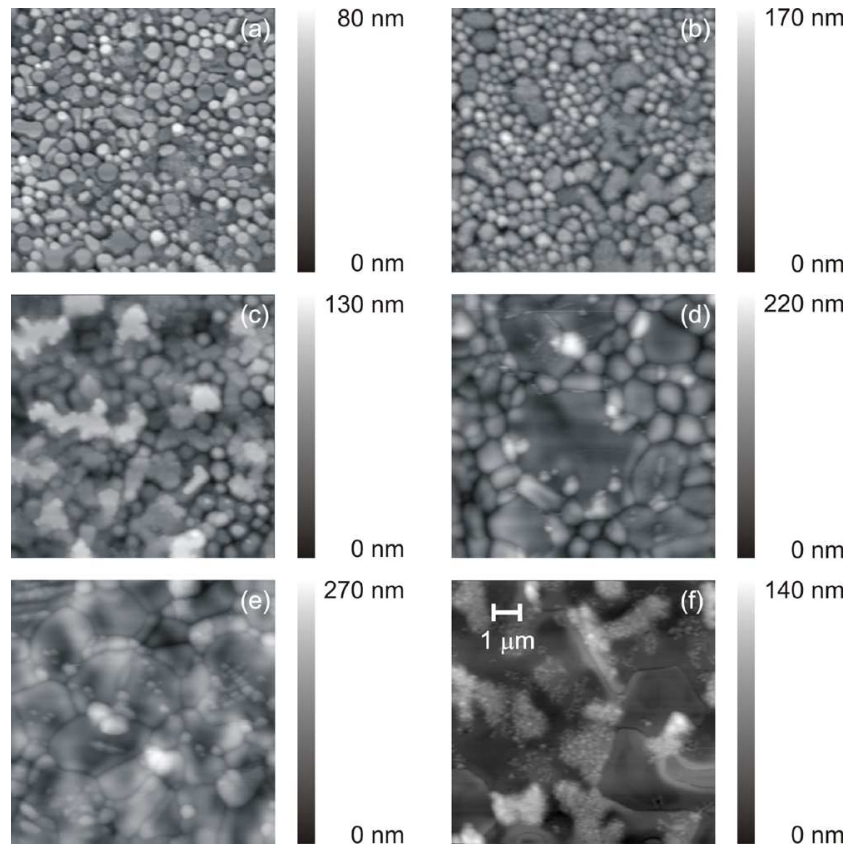


Figure 3.14: Surface topology of an annealed crystal doped with 1.0 wt% Fe_2O_3 measured with an atomic force microscope. The images (a) to (f) are taken at equidistant positions. Image (a) is taken close to the anode, image (f) close to the cathode.

the LiNbO_3 crystal at elevated temperatures, the voltage is dropped automatically. After about 2.7 hours at a temperature of about 500 °C the voltage shows an unexpected peak, i.e., the crystal conductivity increases while the sample is constantly heated. This behavior depends strongly on the total iron concentration as shown in Fig. 3.15. Below a doping level of 2.0 % Fe no peak can be seen. With increasing iron concentration it becomes larger. This anomaly is further analyzed by in-situ observations of the LiNbO_3 crystals during the annealing procedure.

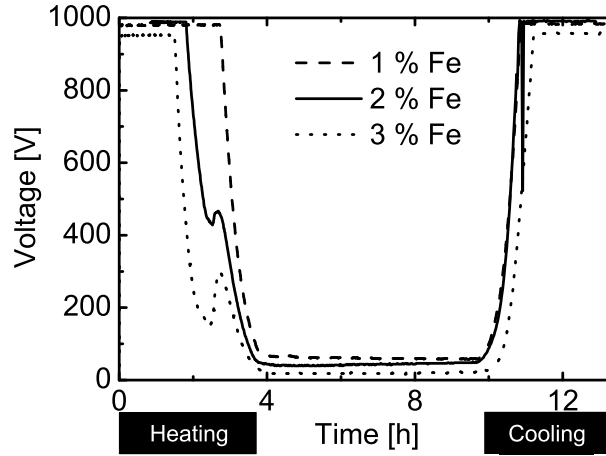


Figure 3.15: Evolution of the voltage during thermo-electric oxidation for crystals doped with 1.0, 2.0, and 3.0 wt% Fe_2O_3 .

3.2.3.2 In-situ observation during annealing

The observation furnace (Sect. 3.1.2.2) is used to get in-situ images of the crystals during the annealing. A picture series is shown in Fig. 3.16. The crystal is heated up from room temperature to 700 °C with $dT/dt = 3$ °C/min. An electric field E_{max} of 125 V/cm is applied at room temperature, and the current density j_{max} is limited to 0.01 mA/mm². The crystal is dwelled on 700 °C for 6 hours and afterwards cooled down to room temperature with $dT/dt = -3$ °C/min. The picture series shows the crystal in the holder with the electrodes at the top and the bottom. At temperatures of about 450 °C a remarkably sharp absorption front starts to cross the initially black crystal from the cathode to the anode. It moves further with increasing temperature. Above 600 °C the bright part of the crystal darkens again starting from the cathode, but with no sharp front. The first absorption front is unaffected by this and continues moving. During the dwell time at 700 °C the first absorption front reaches the anode, but the crystal becomes homogeneously black due to the subsequent darkening. In the moment when the cooling starts a third absorption front begins to transverse the crystal, also starting from the cathode. During cooling the front moves further exhibiting two dark horns (Fig. 3.16, 608 °C) that resemble the weaker doped crystals after annealing (see Fig. 3.9) but disappear after a short while. White precipitations can be seen close to the cathode. At temperatures of about 450 °C the third

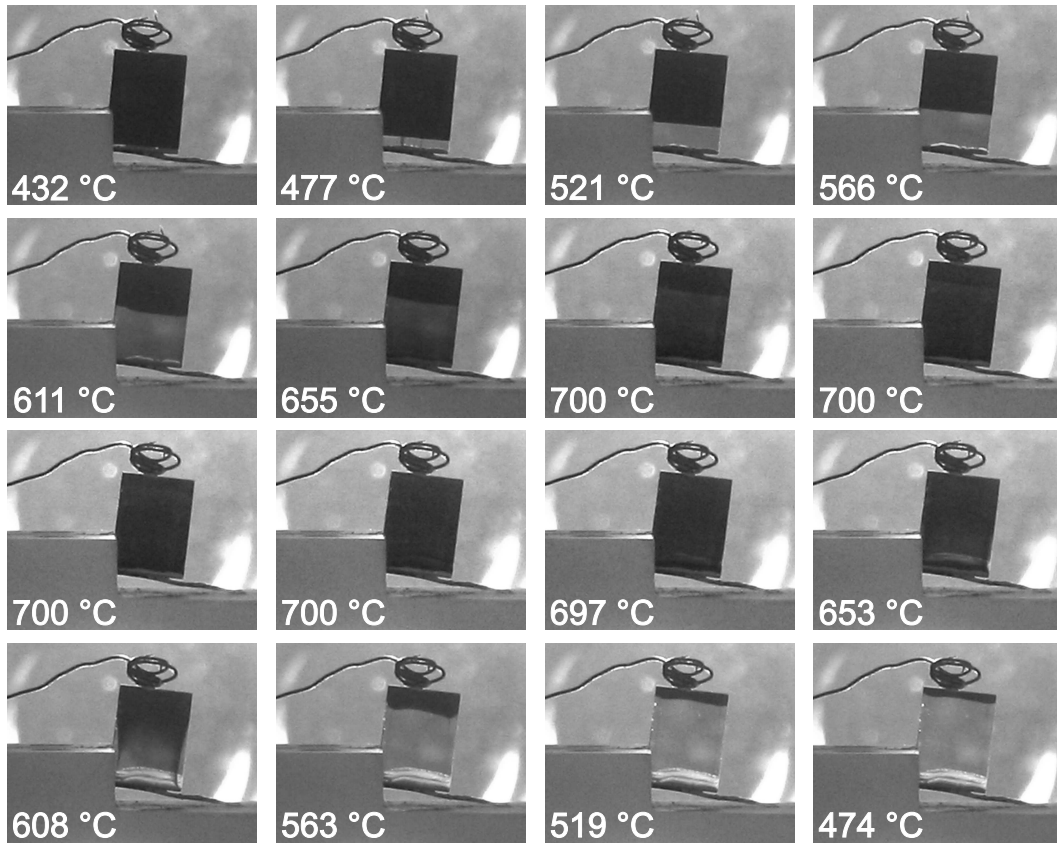


Figure 3.16: The picture sequence shows the evolution of a LiNbO_3 crystal doped with 2.0 wt% Fe_2O_3 during annealing.

absorption front has passed almost the entire crystal.

It has been observed that the first front, which is the sharpest, becomes even sharper with increasing doping level. The dynamics of this front is investigated in detail in the following section.

3.2.3.3 Dynamics of the oxidization

In order to investigate the dynamics of the oxidization process, the time-dependence of the position of the absorption front in the crystal during annealing is analyzed from the

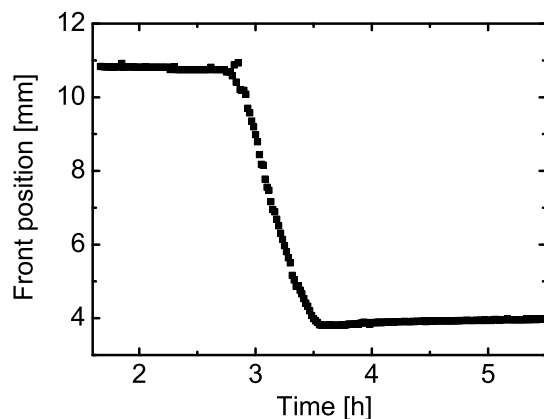


Figure 3.17: Analysis of the motion of the first absorption front crossing the crystal. The position of the front is shown over the time. The sample is doped with 0.5 wt% Fe_2O_3 .

photographs with the help of the following algorithm: The picture is converted into a grayscale bitmap, i.e., an array consisting of integer values. Each integer represent one pixel. A section of the image, where the front is clearly visible, is chosen. It is averaged over every line that is parallel to the absorption front in order to reduce the noise level. Then the spatial derivative of the resulting line which is now perpendicular to the front is calculated. It shows a narrow peak at the position of the absorption front. In order to determine the position of this peak a threshold value is chosen. The peak position is set to be the position where the derivative firstly exceeds this level. The threshold has to be chosen individually for every picture series in the way that only a very few data points exceed the threshold. This algorithm is applied to picture sequences of the annealing of various crystals. A typical plot of the position of the absorption front over the time is shown in Fig. 3.17. The slope determines the velocity of the absorption front. It can be seen that the absorption front moves with constant speed from the cathode to the anode.

3.2.3.4 Varying the parameters

The annealing parameters are varied to find optimum conditions for the oxidization where it is as strong as possible and homogeneous.

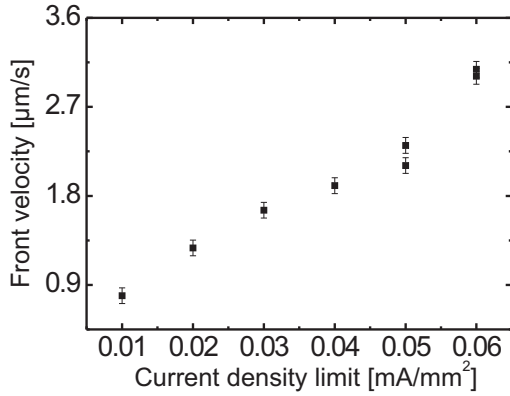


Figure 3.18: Velocity of the absorption front versus current density limit for crystals doped with 0.5 wt% Fe_2O_3 .

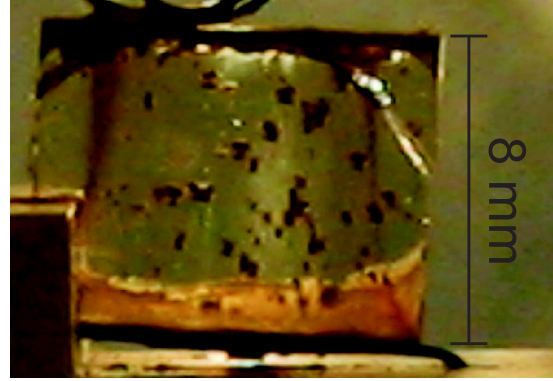


Figure 3.19: Photograph of a crystal doped with 0.5 wt% Fe_2O_3 after thermo-electric oxidation with a current density limitation of 0.5 mA/mm². The dark spots are bulk defects induced by the annealing.

Current limit The velocity of the absorption front is measured for various current density limitations j_{max} . The other parameters are kept constant ($dT/dt = 3 \text{ }^\circ\text{C}/\text{min}$, $E_{\text{max}} = 125 \text{ V/cm}$, $T_{\text{max}} = 700 \text{ }^\circ\text{C}$). The crystals are doped with 0.5 % Fe. The result is shown in Fig. 3.18. The velocity of the absorption front increases linearly with the current limitation. The error bars are estimated from the reproducibility of the measurements. The use of large current limitations leads to the appearance of bulk crystal defects during the 6 hours dwell time at 700 °C. A photograph of such a crystal after annealing is shown in Fig. 3.19. The current density limitation was set to 0.05 mA/mm².

Doping level The velocity of the absorption front is also measured for various doping levels ranging from 0.05 to 2.0 % Fe. The result is shown in Fig. 3.20. The velocity is almost equal for the doping levels 0.5, 1.0, and 2.0 % Fe. Only the crystal that contains 0.05 % Fe shows a significantly faster absorption front.

To predict a dT/dt that allows the first absorption front to transverse a crystal completely during heating the following dependence is found experimentally:

$$\frac{dT}{dt} = \frac{(T_{\text{max}} - 450 \text{ }^\circ\text{C})v_0j_{\text{max}}}{0.01s \text{ mA/mm}^2}, \quad (3.3)$$

where v_0 is the velocity of the absorption front for the doping level used that can be found in Fig. 3.20 and s the distance of the electrodes. Hence if larger crystals are used the

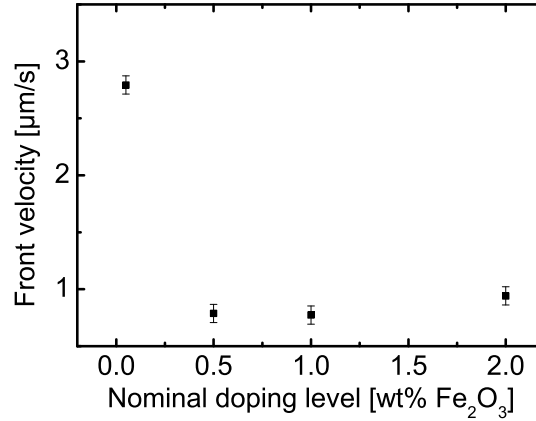


Figure 3.20: Velocity of the absorption front over the iron doping level of the samples.

temperature ramp dT/dt can be tailored to allow the absorption fronts to pass longer distances (see Eq. (3.3)).

Geometry The direction and the orientation of the electric field with respect to the direction and orientation of the c -axis show no significant impact on the oxidization.

Dwell time If the heating ramp does not provide enough time for the first front to pass the whole crystal, the front will continue moving during the dwell time. It is also possible to avoid the dwell time by tailoring the temperature ramps (Eq. (3.3)). This can be useful, because crystal defects are induced mainly during the dwell time.

3.2.4 Conductivity measurements

Conductivity spectra Conductivity spectra are measured for all iron-doped LiNbO₃ crystals and for undoped LiNbO₃ in the frequency range 10 mHz–300 kHz for temperatures between 30 and 700 °C. Typical results are shown in Fig. 3.21. LiNbO₃ doped with 1.0 % Fe in the as-grown state is used. The conductivity shows a frequency-independent part - the DC conductivity σ_{dc} - at small frequencies and an increase above a certain frequency ω_0 . Both parameters σ_{dc} and ω_0 shift to higher values with increasing temperature. The

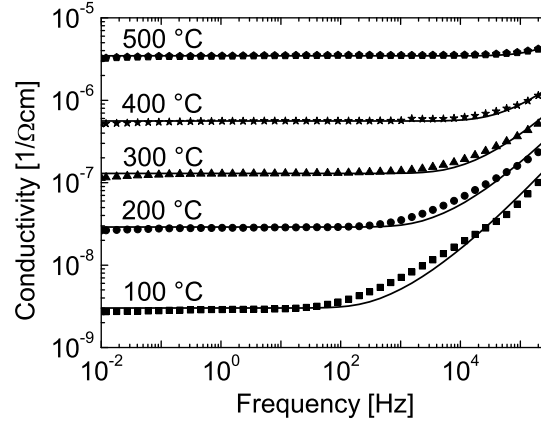


Figure 3.21: Conductivity spectra of a crystal doped with 1.0 wt% Fe_2O_3 at different temperatures. The lines show fits according to the random free energy barrier model.

random-free-energy-barrier-model function (see Sect. 2.3.2.2, Eq. (2.20)) is fitted to the data. By this means σ_{dc} is determined.

Arrhenius plots The resulting DC conductivities are plotted in an Arrhenius plot, i.e., σ_{dc} is plotted logarithmically versus $1000/T$. The plots for crystals in the as-grown state are shown in Fig. 3.22 (a). For most crystals two linear segments and an intermediate region in between are observed. Hence the DC conductivity shows an Arrhenius behavior, i.e., it is thermally activated, with

$$\sigma_{\text{dc}} = \sigma_0^{(1)} \exp\left(-\frac{E_{\text{A}}^{(1)}}{k_{\text{B}}T}\right) + \sigma_0^{(2)} \exp\left(-\frac{E_{\text{A}}^{(2)}}{k_{\text{B}}T}\right) \quad (3.4)$$

with $\sigma_0^{(1,2)}$ constant, $E_{\text{A}}^{(1,2)}$ the activation energies, k_{B} the Boltzmann constant, and T the absolute temperature. In the following the larger activation energy is denoted by $E_{\text{A}}^{(2)}$, the smaller by $E_{\text{A}}^{(1)}$. In the linear segments one of the two contributions in Eq. (3.4) is dominant, the other is negligible, whereas in the intermediate region there are significant contributions from both summands. The linear segments are used to determine the activation energies $E_{\text{A}}^{(1,2)}$.

In the Arrhenius plots of the crystals in the as-grown state the undoped crystal and the

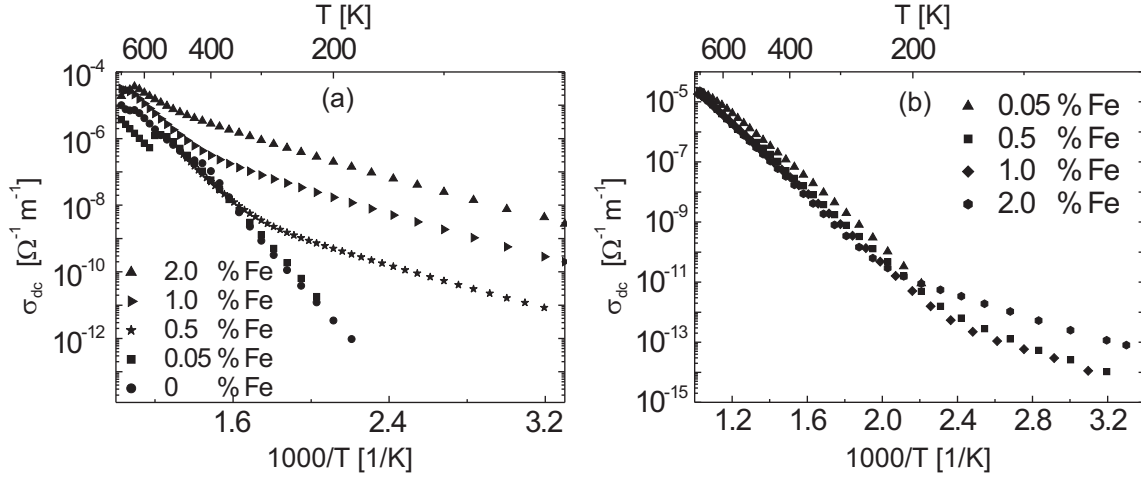


Figure 3.22: Arrhenius plots of the DC conductivity σ_{dc} over $1000/T$ for crystals (a) in the as-grown state and (b) thermo-electrically oxidized.

LiNbO₃ sample doped with 0.05 % Fe show only one straight line with $E_A^{(2)}$. At low temperatures no σ_{dc} could be obtained, because no frequency-independent part of the conductivity is observed down to frequencies of 10^{-2} Hz, and the random-free-energy-barrier-model function (Eq. (2.20)) could not be fitted satisfactorily to the data. The LiNbO₃ samples doped with 0.5 and 1.0 % Fe show two distinct linear segments with different activation energies $E_A^{(1,2)}$ and an intermediate segment where both superpose. For the crystal that is doped with 2.0 % Fe one large segment with $E_A^{(1)}$ is visible and a superposition segment, but up to 700 °C there is not any segment with $E_A^{(2)}$. At high temperatures some discontinuities occur, that originate from outdiffusion of chromium in the steel sample holder, which leads to a detachment of the electrodes.

In general, the segments with the $E_A^{(1)}$ shift to higher conductivities with increased doping levels, i.e., $\sigma_0^{(1)}$ varies with the doping level, whereas the segment with $E_A^{(2)}$ shows no significant dependence on the doping level.

Thermo-electrically oxidized samples are studied as well. They were oxidized with the following parameters: $T = 700$ °C, 6 hours dwell time, $dT/dt = \pm 3$ °C/min, $E_{max} = 1000$ V/mm, $j_{max} = 1 \times 10^{-3}$ mA/mm². After oxidation the samples are ground to remove the residual non-oxidized parts and surface precipitations. The final thickness

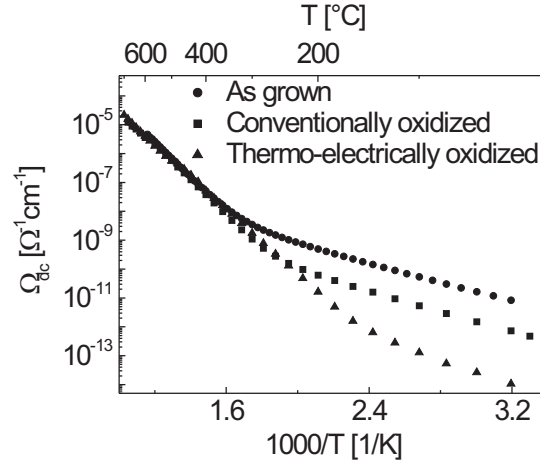


Figure 3.23: Arrhenius plot of the DC conductivity σ_{dc} over $1000/T$ for a crystal doped with 0.5 wt% Fe_2O_3 in the as-grown state, conventionally oxidized and thermo-electrically oxidized.

of the samples varies between 0.1 and 0.6 mm. For the oxidized crystals the same analysis is done. The random-free-energy-barrier-model function is fitted to the data, and σ_{dc} is extracted and plotted in an Arrhenius plot. The result is shown in Fig. 3.22 (b). For the crystals with doping levels from 0.5 - 2.0 % Fe the same two linear segments are found. Note that the segment with the activation energy $E_A^{(1)}$ is shifted by several orders of magnitude compared to that of the crystals in the as-grown state. The crystals doped with 0.5 and 1.0 % Fe show nearly equal conductivities, also in the segment with $E_A^{(1)}$. The LiNbO_3 crystal containing 0.5 % Fe shows small but visible brown inhomogeneities.

In Fig. 3.23 Arrhenius plots of crystals doped with 0.5 % Fe are compared, that show different concentration ratios $c_{\text{Fe}^{2+}}/c_{\text{Fe}}$. One LiNbO_3 crystal is conventionally oxidized, i.e., it is heated up to 1000 °C in oxygen atmosphere for 12 hours. The brown color of the sample after the treatment shows that the oxidation remains incomplete. In the Arrhenius plot a segment with $E_A^{(1)}$ is found that is shifted to lower conductivity values compared to a crystal in the as-grown state, whereas it shows larger conductivities than a thermo-electrically oxidized sample. A side effect of this treatment is the nearly complete loss of hydrogen impurities in the crystal. The OH^- concentration c_{H^+} can be determined

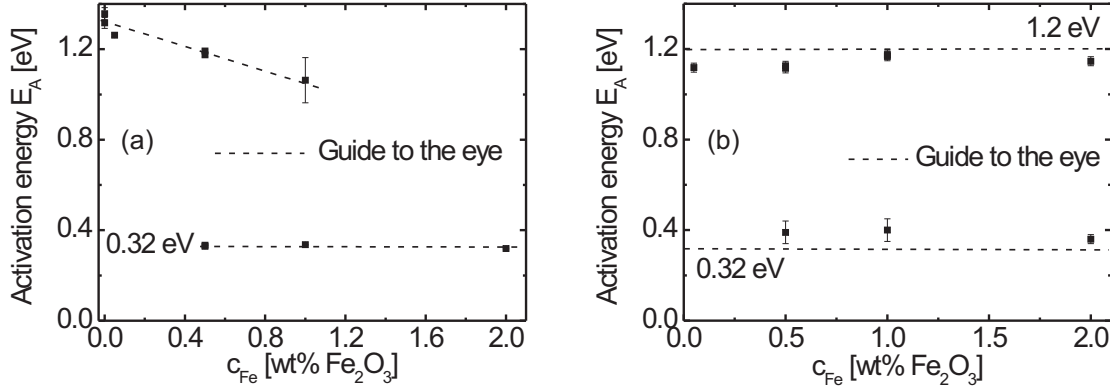


Figure 3.24: Activation energies E_A over iron concentration for LiNbO_3 crystals (a) in the as-grown state and (b) thermo-electrically oxidized.

easily from absorption spectroscopy of the OH^- vibration band [124,125]:

$$c_{\text{H}^+} = (1.67 \pm 0.09) \times 10^{22} \text{ m}^{-2} \alpha_{2870}^0. \quad (3.5)$$

Here α_{2870}^0 denotes the absorption of ordinarily polarized light of the wavelength 2870 nm. No OH vibration peak is found in the crystal any more. With respect to the noise level of the spectrometer a lowering of the hydrogen concentration by at least a factor of five is found. In the thermo-electrically oxidized sample the hydrogen concentration is increased by about one order of magnitude compared to the sample in the as-grown state.

The activation energies $E_A^{(1,2)}$ that are deduced from the Arrhenius plots are summarized in Fig. 3.24. All measured values for $E_A^{(1)}$ are close to 0.32 eV, whereas the values for $E_A^{(2)}$ are close to 1.2 eV.

3.2.5 Birefringence changes at the absorption front

The optical homogeneity of partially oxidized iron-doped LiNbO_3 crystals with various doping levels is examined. The samples used for this study have dimensions of $1 \times 10 \times 8 \text{ mm}^3$ (0.05, 0.5 % Fe) and $1 \times 8 \times 6 \text{ mm}^3$ (1.0 % Fe). All crystals are x -cuts. Only a fraction of the volume of each crystal is oxidized by the thermo-electric oxidization treatment. The samples are heated up to 700 °C, then the temperature is kept constant until about half

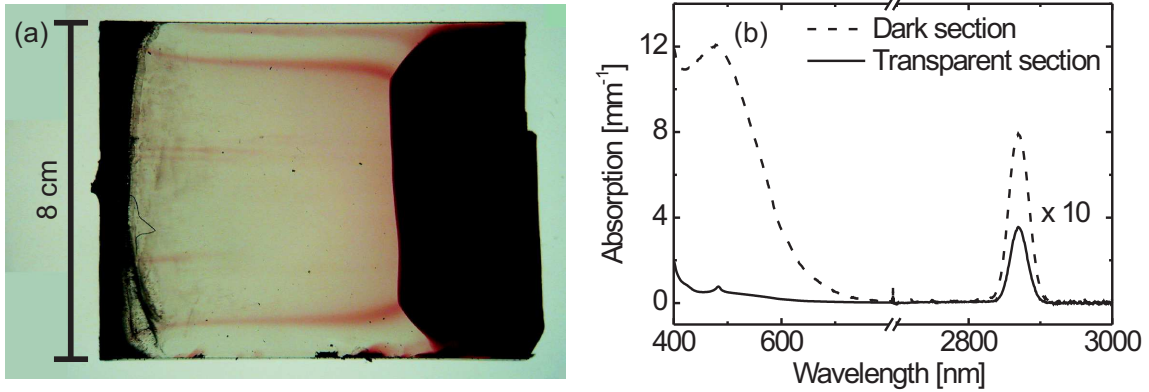


Figure 3.25: LiNbO_3 crystal doped with 0.5 wt% Fe_2O_3 . The thermo-electric oxidation treatment is interrupted before the crystal is completely oxidized. In (a) a photograph is shown, in (b) the corresponding absorption spectra for ordinarily polarized light of the dark and the bright sections. The absorption values between 2700 and 3000 nm are magnified by a factor of 10.

of the crystal volume is oxidized, afterwards the cooling is started. The temperature is changed with $\pm 3^\circ\text{C}/\text{min}$. The electrical field is limited to 125 V/mm and the current density to 0.01 mA/mm². A photograph of such a partially oxidized crystal which is doped with 0.5 % Fe is shown in Fig 3.25 (a). The absorption front is very sharp, and the dark and the transparent sections of the crystal appear homogeneous. The absorption spectra of the dark and the transparent sections of the crystal are shown in Fig. 3.25 (b). A strong decrease of the Fe^{2+} absorption in the transparent section due to the oxidation is observed and also the absorption peak originating from the OH vibration around 2870 nm is decreased. The hydrogen (H^+) concentration can be deduced from this absorption peak (Eq. (3.5)). The Sénarmont setup shown in Sect. 3.1.4 is used to determine absolute values of birefringence changes $|\Delta(n_e - n_o)|$ at the absorption front by scanning from the transparent side to the dark side of the crystal. The result of the scan with the Sénarmont setup is shown in Fig. 3.26 (a). The birefringence changes by about 1.2×10^{-4} at the front, whereas it remains constant in the dark and the transparent sections of the crystal. It is checked with an atomic force microscope that the thickness of the crystal does not change at the absorption front. This is necessary to assure that the measured phase changes originate

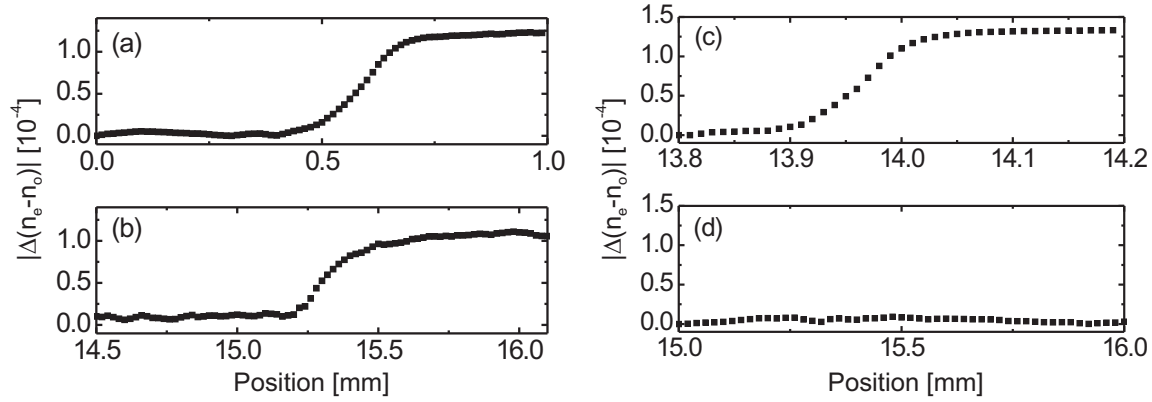


Figure 3.26: Absolute value of the birefringence change $|\Delta(n_e - n_o)|$ vs. the position in the crystal. The crystals are doped with (a) 0.5, (b) and (d) 1.0, and (c) 0.05 wt% Fe_2O_3 . The crystals in (b) and (c) are pretreated.

from refractive index changes and not from thickness variations of the sample.

The same analysis is performed with other samples: In Fig. 3.26 (b) data of a crystal that is doped with 1.0 % Fe are presented. In order to avoid too large absorption in the dark part of the crystal, it is conventionally oxidized in a pretreatment (12 h at 1100 °C in oxygen atmosphere). The conventional oxidization technique leads to a homogeneous decrease of $c_{\text{Fe}^{2+}}$ in the entire crystal. In a second step the crystal is thermo-electrically oxidized generating the absorption front. In (c) $|\Delta(n_e - n_o)|$ of a sample that contains 0.05 % Fe is shown. The crystal is reduced in a pretreatment in order to enhance the resulting birefringence changes. It is annealed for 12 hours at a temperature of 1000 °C in vacuum ($p = 10^{-4}$ mbar). In Fig. 3.26 (d) $|\Delta(n_e - n_o)|$ of a crystal doped with 1.0 % Fe is shown. In this particular sample two separated absorption fronts are seen. The color changes from transparent to brownish at the first front and from brownish to dark at the second front. Such a second absorption front occurs especially if $|dT/dt|$ is smaller for heating than for cooling. The measurement is performed at the first front, where the crystal is transparent enough. A summary of all measured absolute values of the birefringence changes and of the Fe^{2+} and the H^+ concentration changes that are deduced from the absorption spectra are given in Tab. 3.2.

c_{Fe} [wt% Fe_2O_3]	pretreatment	$\Delta c_{\text{Fe}^{2+}}$ [10^{25} m^{-3}]	Δc_{H^+} [10^{25} m^{-3}]	$ \Delta(n_e - n_o) _{\text{meas}}$ [10^{-4}]
0.05	reduced	-1.4 ± 0.4	0 ± 0.01	1.3 ± 0.1
0.5	—	-2.5 ± 0.8	-0.7 ± 0.04	1.2 ± 0.1
1.0	oxidized	-1.6 ± 0.5	-0.24 ± 0.01	1.0 ± 0.1
1.0	—	-0.18 ± 0.05	-0.17 ± 0.01	< 0.1

Table 3.2: Nominal iron concentration c_{Fe} , pretreatment before the thermo-electric oxidation, difference $\Delta c_{\text{Fe}^{2+}}$ of the Fe^{2+} concentrations between dark/brownish and transparent sections of the crystals, difference Δc_{H^+} of the H^+ concentrations between dark and transparent sections of the crystals, and measured birefringence change $|\Delta(n_e - n_o)|_{\text{meas}}$ for all crystals used. The sample with 1.0 wt% Fe_2O_3 and without pretreatment exhibits two sharp absorption fronts. The presented data refer to the changes between brown and transparent sections.

3.2.6 Investigations of the precipitation

The solubility of the surface precipitations after the thermo-electric oxidation is examined. The crystals are placed into warm water ($T = 70^\circ\text{C}$). After 30 minutes the gold layer that acted as the cathode during annealing is detached from the surface, whereas the anode sticks firmly to the crystal. Part of the visible surface structure cannot be solved in warm water even after days. The water with the solved part of the precipitations is analyzed in a mass spectrometer. To assure that as much as possible of the solvable compounds are solved, the thermo-electrically oxidized sample is placed into water for several weeks. For comparison a crystal with gold electrodes, but still untreated, is also set into warm water for the same time. The solution that was obtained from the oxidized sample shows an increased lithium concentration by a factor of 4 with respect to the solution from the untreated sample.

3.2.7 Various dopants

The thermo-electric oxidation treatment is applied to LiNbO_3 doped with copper (Cu) and manganese (Mn). The copper-doped samples are fabricated by indiffusion of copper into undoped LiNbO_3 . The manganese-doped crystals are supplied by Deltronics, Inc. It is observed that copper-doped crystals show only very small oxidized parts for annealing parameters that resemble the optimum parameters for the oxidation of iron doping. Manganese-doped crystals have been successfully oxidized with $dT/dt = 0.1^\circ\text{C}/\text{min}$ instead of $dT/dt = 3^\circ\text{C}/\text{min}$ for iron. Undoped LiNbO_3 crystals that are heavily reduced

and therefore appear black are fully reoxidized by the thermo-electric oxidization treatment under similar experimental conditions compared to iron-doped crystals also showing a sharp oxidization front moving from the cathode to the anode.

Chapter 4

Photorefraction

4.1 Experimental methods

4.1.1 Crystals

Photorefraction measurements are performed with the highly iron-doped, completely oxidized samples mentioned in Sect. 3 as well as with undoped LiNbO_3 wafers grown from a congruent melt. The supplier Crystal Technology, Inc. specifies that these undoped crystals contain less than 1 ppm iron impurities. Other impurities have even smaller concentrations. The samples are x -cuts with a size of $1 \times 8 \times 10 \text{ mm}^3$. The c -axis is not parallel to the edges but includes a 45° angle.

Periodically-poled z -cut samples provided by Crystal Technology, Inc. are also used. The domain grating has period lengths between 5.9 and $6.3 \mu\text{m}$. The crystals are 5 cm long, 1 cm wide and 0.5 mm thick. The end faces are polished to optical grade.

4.1.2 Measurements of the photorefraction

The photorefractive optical damage is measured in undoped lithium niobate crystals with the help of the spread-out of the transmitted beam ("beam fanning"), the Sénarmont compensator setup, and measurements of the maximum obtainable second harmonic power.

4.1.2.1 Beam fanning

The fastest and simplest, but rather qualitative measurements of the optical damage are performed with the setup shown in Fig. 4.1. A frequency-doubled Nd:YAG laser beam

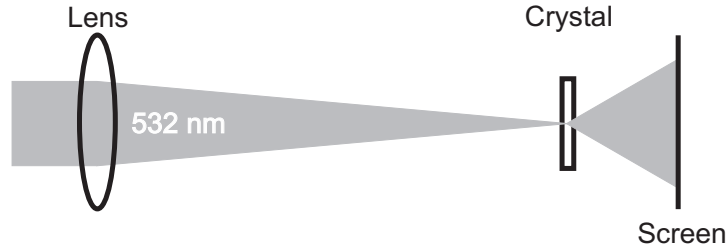


Figure 4.1: Setup to measure qualitatively the optical damage by observing the distortion of a green light beam that passes the crystal.

(wavelength $\lambda = 532$ nm) is focussed into a LiNbO_3 sample. The light intensity can be varied. The transmitted light beam is observed on a screen. Its beam shape will be distorted, if optical damage is present.

4.1.2.2 Sénarmont compensator method

For optical damage quantification the Sénarmont compensator setup from Sect. 3.1.4, which is able to measure birefringence changes, is extended by the possibility to illuminate the samples and to measure *light-induced* birefringence changes. All parameters mentioned in Sect. 3.1.4 are also used in this study. A schematic of the extended setup is shown in Fig. 4.2. In addition to the setup shown in Fig. 3.7, a frequency-doubled continuous-wave Nd:YAG laser beam is focussed into the crystal to create birefringence changes via the photorefractive effect. The HeNe laser beam is too weak to cause any significant photorefracton. The green laser beam has a focal waist of $2\sigma_{532} = 20 \mu\text{m}$. The light intensity ($I \leq 8 \text{ GW/m}^2$) can be varied by a half-wave plate and a polarizer. Moreover the beam is expanded and spatially frequency filtered for smallest possible beam waist and optimum beam shape. For simplicity these components are not shown in Fig. 4.2. Behind the crystal the green beam is reflected into a beam blocker with the help of a dielectric mirror that is highly reflecting for light of the wavelength 532 nm, whereas it has large transmittance for the 633 nm HeNe laser beam. The beam splitter enables the overlap of the green and the red laser beams. A glass plate is used as beam splitter. About 7 % of the red laser beam are reflected into the crystal and consequently only about 7 % of the green laser beam are lost at the beam splitter. The red laser beam can be shifted with respect to the fixed green laser beam in order to perform lateral scans of the birefringence pattern. The minimum scanning step size is $2.5 \mu\text{m}$. Usually one such scan - the baseline - is recorded before the illumination with the green light beam. It shows if birefringence

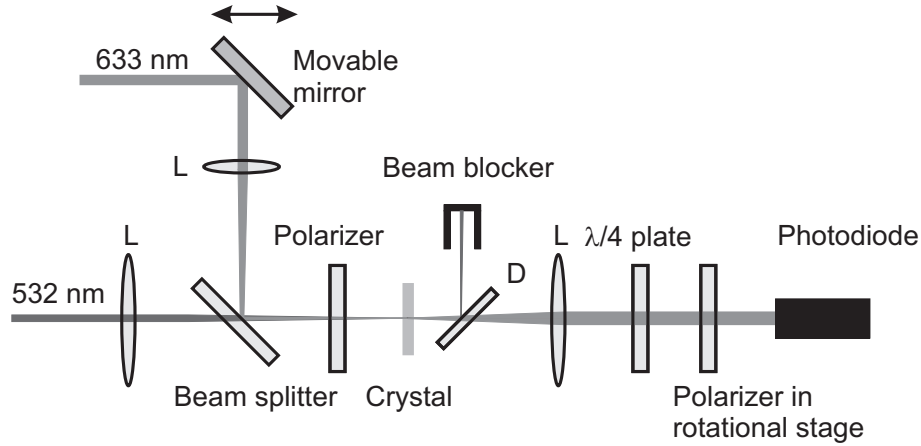


Figure 4.2: Schematic of the extended Sénarmont setup for measurements of light-induced refractive-index changes. The abbreviations in the figure are L: lens, D: dielectric mirror.

inhomogeneities are already present in the crystal. After the illumination a second scan is taken showing the sum of already existing birefringence inhomogeneities and light-induced birefringence changes. That scan is corrected by subtracting the baseline. The crystals are illuminated with the green laser beam for several minutes in order to assure that the birefringence change has reached its equilibrium.

Simulation The finite waist of the red readout beam leads to an underestimation of the birefringence change maximum. In order to correct the error this behavior is simulated. A two-dimensional Gaussian function $A(x, y)$ represents the spatial birefringence pattern in a sample after illumination with the green laser beam. It is proportional to the phase shift $A'(x, y)$ behind the analyzer. It has a waist $2\sigma_{\Delta n}$. A second two-dimensional Gaussian function $B(x, y)$ represents the intensity of the red readout beam. Its waist is $2\sigma_r$. Every point in the birefringence pattern that is illuminated by the readout beam contributes to the signal behind the analyzer with its particular phase shift weighted by the intensity of the readout beam. So rotating the analyzer by the angle α gives the following signal shape:

$$\begin{aligned} & \int \int B(x, y) \sin[\alpha + A'(x, y)] dx dy \\ &= \sin(\alpha) \int \int B(x, y) \cos[A'(x, y)] dx dy + \cos(\alpha) \int \int B(x, y) \sin[A'(x, y)] dx dy \end{aligned} \quad (4.1)$$

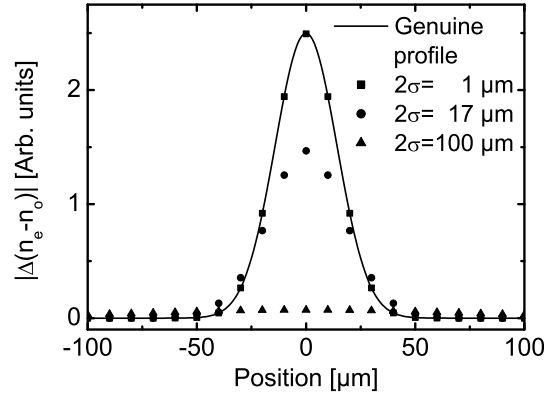


Figure 4.3: Simulation of the impact of the beam waist $2\sigma_r$ of the readout beam on the measured birefringence profile.

A numerical simulation is performed. The result can be found in Fig. 4.3 for beam waists of the readout beam of 1, 17, and 100 μm . The waist of the birefringence profile is $2\sigma_{\Delta n} = 20 \mu\text{m}$. It can be seen that a readout beam with a very small waist (1 μm) compared to the birefringence pattern leads to an exact reproduction of the pattern, whereas a much broader readout beam (100 μm) leads to a strong underestimation of the amplitude and a broader profile. The value for the waist of the readout beam of 17 μm , that is chosen in the following experiments, leads to a good reproduction of the profile shape, but underestimates the amplitude by about a factor of two. In the experimental results it is accounted for this error.

4.1.2.3 Second-harmonic generation

For the investigation of the second-harmonic generation a continuous-wave Yb:YAG laser beam (wavelength $\lambda = 1030 \text{ nm}$) is focussed into a congruently melting, periodically-poled, undoped lithium niobate crystal. The beam waist in the focus is 90 μm . The crystal is temperature stabilized by $\pm 0.1 \text{ }^\circ\text{C}$. The crystal sections with domain period lengths of 6.129, 6.071, and 6.014 μm are used, specified by the manufacturer of the photolithographic mask for the fabrication of the PPLN. The corresponding phase matching temperatures are 50, 70, and 90 $^\circ\text{C}$. In the crystal the infrared light is partially frequency-doubled to green light of the wavelength 515 nm. Two dielectric short-pass filters separate the infrared

pump beam from the frequency-doubled green beam. The reflectivity of the mirrors for the infrared light is larger than 99 %. The transmitted light power is measured. In order to calculate the pump power P_P^{int} inside the crystal and the generated second-harmonic light power $P_{\text{SHG}}^{\text{int}}$ inside the crystal, the limited transmission at the crystal surfaces for light of the wavelengths 515 nm T_C^{515} and 1030 nm T_C^{1030} as well as the limited transmission of the dielectric mirrors for the frequency-doubled light T_M^{515} are taken into account:

$$P_{\text{SHG}}^{\text{int}} = P_{\text{SHG}}^{\text{meas}} / (T_C^{515} T_M^{515} T_M^{515}) \quad (4.2)$$

$$P_P^{\text{int}} = T_C^{1030} P_P^{\text{meas}}. \quad (4.3)$$

4.2 Experimental results

4.2.1 Photorefraction in iron-doped oxidized LiNbO_3 crystals

The beam fanning in highly iron-doped thermo-electrically oxidized samples is investigated. The result is shown in Fig. 4.4. All crystals are exposed to the same light intensity $I \approx 50 \text{ MW/m}^2$. It can be seen that the beam fanning becomes less pronounced for higher doping levels. The crystal containing 3.0 % Fe shows about the same beam fanning, i.e., optical damage as a congruently melting and undoped LiNbO_3 crystal.

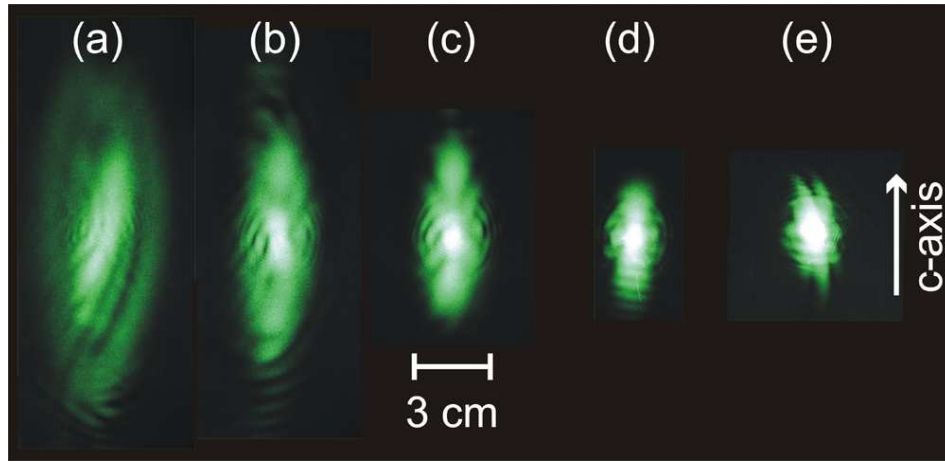


Figure 4.4: Beam fanning of highly iron-doped thermo-electrically oxidized LiNbO_3 crystals. The samples contain: (a) 0.5, (b) 1.0, (c) 2.0, and (d) 3.0 wt% Fe_2O_3 . For comparison the beam fanning of a congruently melting, undoped LiNbO_3 crystal is shown in (e).

4.2.2 Photorefractive in undoped LiNbO_3 crystals

4.2.2.1 Single crystals

Undoped congruently melting LiNbO_3 crystals are annealed using the annealing parameters that lead to optimum oxidization for doping levels from 0.05 to 4.0 % Fe: Annealing for 6 hours at 700 °C, $dT/dt = \pm 3$ °C/min, $E_{\text{max}} = 125$ V/mm, $j_{\text{max}} = 0.01$ mA/mm². No significant changes in the absorption spectra can be observed, only the OH vibration peak is enhanced by about a factor of 2. The crystal is as transparent as before the treatment, within the sensitivity of the spectrometer used, but in some cases surface and bulk defects arise that resemble the defects occurring during annealing of iron-doped LiNbO_3 . Furthermore, small pieces of the crystal detach at the anode.

Beam fanning Crystals that are treated in the way described above are investigated in the beam fanning setup. The result is shown in Fig. 4.5. The beam fanning of a green laser beam that has passed an untreated crystal (a) is compared to the beam fanning generated by an annealed sample (b). The light intensity is the same in both cases ($I \approx 100$ MW/m²). The treated LiNbO_3 crystal exhibits almost no beam fanning whereas the untreated sample

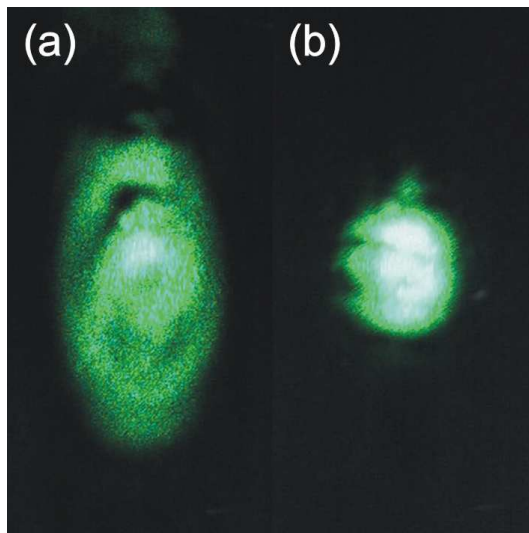


Figure 4.5: Beam fanning of a light beam that has passed an undoped congruently melting LiNbO_3 crystal: (a) as grown, (b) thermo-electrically oxidized.

leads to the typical spread-out of the laser beam.

Sénarmont compensator measurements Quantitative measurements of the birefringence changes of the same crystals as mentioned above are performed with the help of the Sénarmont setup. The crystals are illuminated with the Nd:YAG laser beam varying the light intensity. After every illumination a lateral scan of the birefringence changes is recorded. Typical results of these scans are shown in Fig. 4.6. They exhibit nearly Gaussian shape, and the widths of the birefringence patterns are broader compared to the width of the green laser beam. The amplitude of the pattern is plotted versus the intensity of the Nd:YAG laser beam. The result can be seen in Fig. 4.7. For comparison the birefringence changes of a conventionally oxidized sample are presented. All crystals show a linear increase of the birefringence change with increasing light intensity. It can be seen, that the crystal in the as-grown state shows the largest slope of the birefringence change, and the thermo-electrically oxidized crystal exhibits the smallest slope, which is one order of magnitude smaller than that of the as-grown sample. The conventionally oxidized crystal shows a slope between those of the other crystals. At higher light intensities than those that are used in Fig. 4.7, no steady-state value of $|\Delta(n_e - n_o)|$ is achieved. Some crystals exhibit inhomogeneities concerning the light-induced birefringence changes. With the pre-

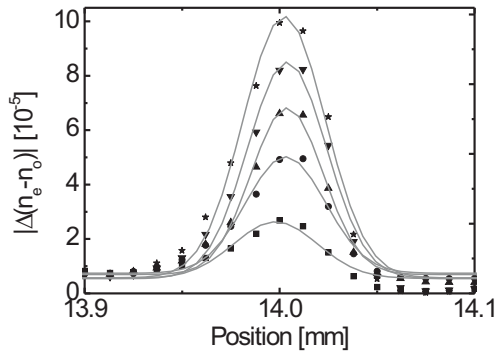


Figure 4.6: Birefringence change $|\Delta(n_e - n_o)|$ for a thermo-electrically oxidized crystal versus position of the scanning HeNe laser beam for various light intensities: 50, 70, 90, 110, and 140 MW/m² (increasing amplitudes). The lines show Gaussian fits.

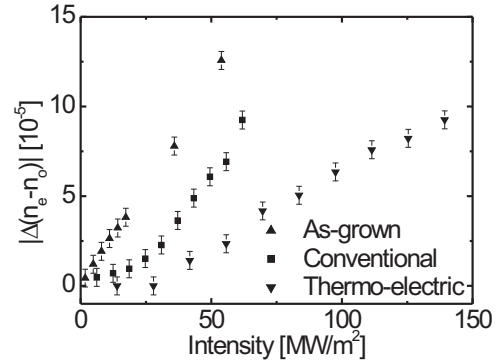


Figure 4.7: Amplitudes of the absolute value of the birefringence change vs. light intensity for an undoped LiNbO₃ crystal in the as-grown state, a conventionally oxidized crystal, and a thermo-electrically oxidized sample.

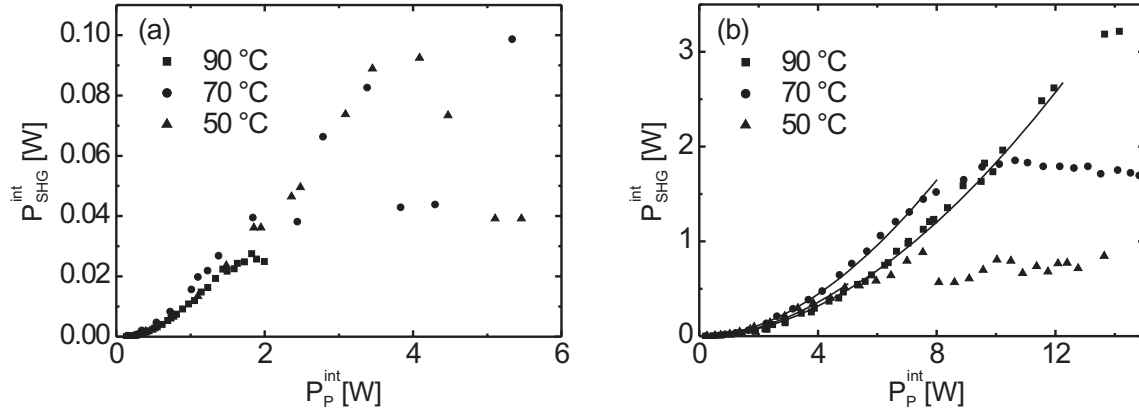


Figure 4.8: Power of the second-harmonic wave $P_{\text{SHG}}^{\text{int}}$ vs. the pump power $P_{\text{P}}^{\text{int}}$ for various temperatures. In Fig. (a) PPLN crystals in the as-grown state are used. The samples in (b) are thermo-electrically oxidized.

sented Sénarmont setup systematic studies on the homogeneity are rather time consuming. Usually three different positions in the crystal, one near to the cathode, one near to the anode and one position in between is investigated. It is averaged over these results.

For comparison a LiNbO_3 crystal containing 5.5 mol% MgO is studied. At the light intensities up to 150 MW/m^2 no light-induced birefringence changes are observed.

4.2.2.2 Periodically-poled lithium niobate

The photorefraction in the undoped, congruently melting, periodically-poled LiNbO_3 crystals is measured with the help of second-harmonic generation. The internal second-harmonic power $P_{\text{SHG}}^{\text{int}}$ is measured as a function of the internal pump power $P_{\text{P}}^{\text{int}}$ for 50, 70, and 90 °C. The result is shown in Fig. 4.8 (a). The power of the frequency-doubled light increases quadratically with the internal pump power until a threshold is reached at about $P_{\text{SHG}}^{\text{int}} = 30 \text{ mW}$. Larger values, achieved in some cases, are not reproducible. Above this threshold the beam shape is visibly distorted and no further increase of the second-harmonic power is obtained. The untreated crystals exhibit no clear temperature dependence. After the thermo-electric oxidization treatment the second-harmonic power is measured again. The results are depicted in Fig. 4.8 (b). The treated crystals show

Temperature [°C]	$P_{\text{SHG}}^{\text{max}}$ (as grown) [mW]	$P_{\text{SHG}}^{\text{max}}$ (oxidized) [mW]
50	≈ 30	500
70	≈ 30	1500
90	≈ 30	2600

Table 4.1: Maximum stable internal second-harmonic powers $P_{\text{SHG}}^{\text{max}}$ for congruently melting undoped periodically-poled LiNbO_3 crystals before and after thermo-electric oxidation treatment at different phase matching temperatures.

the same quadratic increase of the second-harmonic output power until a threshold is reached, but the maximum obtainable output power is enhanced drastically. At 90 °C up to 3.2 W of green light are generated. The lines show quadratic fits. The highest stable second-harmonic output powers that are generated by untreated and oxidized samples are summarized in Tab. 4.1. The light beam passes the PPLN crystal over its full length and averages over the induced optical damage. Hence inhomogeneities in the optical damage, as observed in the measurements of the light-induced birefringence changes in Sect. 4.2.2.1, contribute to the measured output power. The maximum output power is generated within a very small temperature range because of the phase-matching requirement. A graph of the temperature dependence of the second-harmonic output can be seen in Fig. 4.9. A theoretical calculation using the Sellmeier equation is also shown.

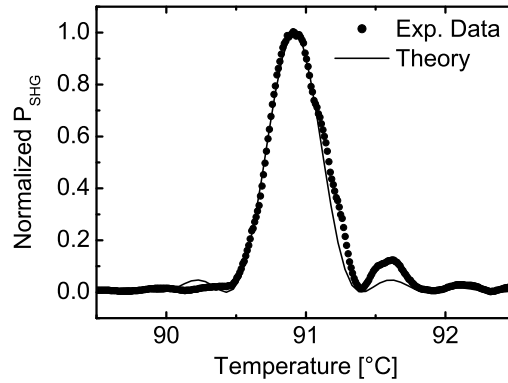


Figure 4.9: Power of the second-harmonic output P_{SHG} vs. temperature. The line shows the theoretically expected dependence.

Chapter 5

Discussion

5.1 Oxidization

Tailoring the degree of oxidization of iron doping, i.e., the concentration ratio $c_{\text{Fe}^{2+}}/c_{\text{Fe}}$, is crucial for many applications in nonlinear optics and photorefraction. For iron-doped LiNbO_3 crystals with doping levels ranging from 0.05 to 4.0 % Fe, the novel thermo-electric oxidization method leads to a nearly complete oxidization of Fe^{2+} to Fe^{3+} (Fig. 3.10 (b)). The known conventional oxidization is able to oxidize the iron impurities only partially, and the crystals remain dark (Fig. 3.12). From Fig. 3.9 it is obvious that the oxidization becomes more homogeneous for doping levels above 2 % and the entire crystal volume is oxidized, whereas crystals with doping levels smaller than 2 % show residual dark areas. The charge of the removed electrons has to be compensated by other charged species. Obviously, this process is not limiting the thermo-electric oxidization up to 4.0 % Fe. The coloration of the highly-doped crystals is due to the shift of the absorption edge and the spin-forbidden Fe^{3+} transition, but not from significant residual Fe^{2+} centers as it can be deduced from the absorption spectra in Fig. 3.10 (b). The residual extinction signal around 500 nm can include contributions from small residual Fe^{2+} concentrations as well as scattering and absorption from the bulk and surface defects that are induced by the annealing process. These scratches (Fig. 3.13), surface precipitations (Fig. 3.14) and bulk defects (Fig. 3.19) probably originate from a phase transition of LiNbO_3 . In Fig. 2.6 the phase diagram of LiNbO_3 is shown. At typical annealing temperatures of 700 °C the formation of lithium triniobate (LiNb_3O_8) is possible. At temperatures above 300 °C it grows along scratches in the surface and around other surface defects [79]. The scratches that are observed after the thermo-electric oxidization do not form during annealing, but very small, invisible scratches being present after polishing become visible after annealing due to the precipitation of LiNb_3O_8 along them. At higher temperatures LiNb_3O_8 forms

faster on the entire surface. It has been reported that at a temperature of 750 °C after 1 day a surface layer can be found. Hence it seems reasonable to assume that the surface precipitations observed after 6 hours at 700 °C consist at least partially of LiNb_3O_8 . The bulk defects, that are found to form at 700 °C preferentially if larger currents flow, can also consist of LiNb_3O_8 . In the literature the formation of LiNb_3O_8 in the bulk is reported after much longer times than 6 hours [79], but the formation can be enhanced by currents flowing through the crystal.

5.1.1 Dynamics of the oxidation

The evolution of the voltage at constant current during the annealing procedure shows a remarkable anomaly (see Fig. 3.15). The peak after 2.7 h, when the crystal has a temperature of about 500 °C, shows a significantly decreased conductivity of the crystal during this annealing phase. From the in-situ observations of the oxidation in Fig. 3.16 it can be seen that the decrease of the conductivity and the appearance of the absorption front occur simultaneously. The measurements of the conductivity spectra (Fig. 3.23) show that the oxidation indeed decreases the conductivity of the crystals at room temperature by orders of magnitude. This decrease is larger for higher doping levels (Figs. 3.22). However, at temperatures around 500 °C, when the oxidation starts, only the crystals with the highest doping levels above 1.0 % Fe show a significant decrease of the conductivity. That is why the peak in the evolution of the voltage only appears for crystals above 1 % Fe doping level and it becomes more distinct with increasing iron concentration. When the crystal starts to oxidize in a certain region the conductivity is decreased locally. Now the crystal can be seen as two resistors in series with different resistances. This implies that a larger part of the applied voltage drops over the higher resistance, i.e., the oxidized part of the crystal. If the voltage drives the oxidation process this will lead to a self-enhancing oxidation process and to the formation of an absorption front that is more distinct for larger differences in the conductivity, i.e., higher doping levels. This is consistent with the observation that the absorption front is sharper with higher doping levels (Fig. 3.9). This model is now considered in detail.

5.1.2 Shock-wave model

Acoustic shock waves are characterized by propagating, nearly discontinuous changes of some properties of the medium, e.g., the density. During the thermo-electric oxidation a front crosses the crystals that separates crystal fractions of different absorption, conductivity, and Fe^{2+} concentration. Due to this analogy it is reasonable to model the processes that occur during the thermo-electric oxidation within the framework of a shock-wave model.

5.1.2.1 Model and notation

Let $N_{\text{Fe}^{2+}}$ and $N_{\text{Fe}^{3+}}$ be the concentration of Fe^{2+} and Fe^{3+} centers, $N_{\text{Fe}} = N_{\text{Fe}^{2+}} + N_{\text{Fe}^{3+}}$ be the total concentration of iron, and n be the concentration of free electrons. Since the main source of free electrons for temperatures used in the experiments presented here ($T \leq 700$ °C) are Fe^{2+} ions, it is also useful to employ the parameter $N^- = N_{\text{Fe}^{2+}} + n$. It represents the total concentration of active electrons. These electrons can be redistributed via charge transport processes at elevated temperatures. With good accuracy, the concentration of free electrons is

$$n = \frac{sN_{\text{Fe}^{2+}}}{\gamma(N_{\text{Fe}} - N_{\text{Fe}^{2+}})}, \quad (5.1)$$

where s and γ are the excitation and the recombination coefficients, respectively. The excitation coefficient is expected to be thermally activated, $s \propto \exp[-E_A/(k_B T)]$, where E_A is the activation energy and k_B is Boltzmann's constant. The expression $1/[\gamma(N_{\text{Fe}} - N_{\text{Fe}^{2+}})]$ represents the recombination time for free electrons. Most probable, this time does not possess a strong temperature dependence. As long as no charge transport takes place, the parameter $N^- = N_{\text{Fe}^{2+}} + n$ remains temperature independent within our model, while the constituents $N_{\text{Fe}^{2+}}$ and n possess strong temperature dependences. When considering the electric properties, compensation charges are of major importance. Let N^+ be the concentration of these charges. The question which kind of charge carrier is represented by N^+ is answered later (Sect. 5.1.3).

Let us denote N_0^\pm as the uniform background concentrations of N^\pm in the absence of charge transport processes. These parameters are temperature independent by definition. In particular, N_0^- can be treated as the concentration of Fe^{2+} ions at room temperature when the thermal excitation of electrons is negligible. As soon as the charge neutrality requirement is applied, we have to assume that the background charge concentration $e(N_0^+ - N_0^-)$, where e is the elementary charge, is compensated by certain immobile charges, i.e., crystal ions. Such a compensation is expected to be present in this model. To consider the influence of charge transport processes, it is necessary to use model expressions for electronic currents and the currents produced by the compensation charge carriers. In the following it is assumed that drift of free electrons and compensating mobile charge carriers are the dominant charge transport processes. The corresponding model expressions for the current densities j_\pm are

$$j_\pm = e\mu_\pm N^\pm E, \quad (5.2)$$

where E is the electric field, μ_- is the mobility of free electrons, and μ_+ is the mobility of the compensation mobile charges. The mobilities are indeed positive quantities. The electron flux is obviously $-\mu_- n E$, it is antiparallel to the electronic current. The flux of the positive compensation charges, $\mu_+ N^+ E$, is antiparallel to the electron flux. The

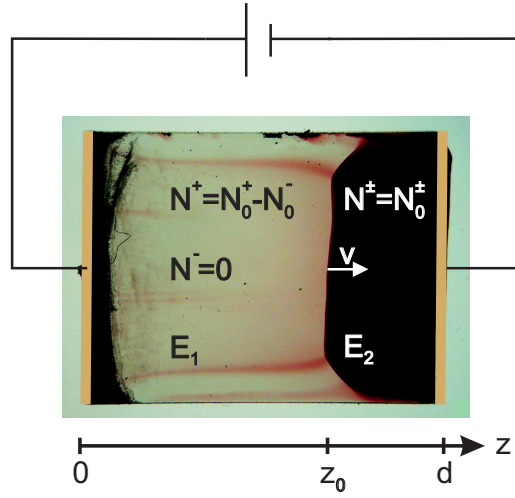


Figure 5.1: Geometric schematic of the shock-wave model.

products $-\mu_-E$ and μ_+E represent the drift velocities of free electrons and mobile compensation charges, respectively. Both mobilities are expected to be thermally activated $\mu_{\pm} \propto \exp[-E_A^{\pm}/(k_B T)]$. From Fig. 3.22 it can be inferred that this assumption is indeed valid for the electrons.

Diffusion of the charge carriers can be responsible for the sharpness of the shock-wave front. In the leading approximation it is, however, negligible. The bulk photovoltaic effect is absent under thermal excitation.

5.1.2.2 Shock-wave solution

Let d be the thickness of an iron-doped LiNbO_3 crystal so that the coordinate z is changing from 0 to d (see Fig. 5.1). Let a negative voltage $-U_0$ be also applied between the electrodes at positions d and 0. Consequently the average applied field inside the sample is $-E_0 = -U_0/d$.

The aim of this analysis is to find a shock-wave solution for $N^{\pm}(z, t)$ and the electric field distribution $E(z, t)$ in the presence of the voltage. It is assumed that the shock-wave front at the time t is situated at $z = z_0(t)$, and the velocity of this front is $v = v(z_0)$. All variables experience discontinuities at this point. To the left side of the front, i.e., for $0 < z < z_0$, $N^- = n = 0$, i.e., iron is completely oxidized and $N^+ = N_0^+ - N_0^-$ is larger than 0 for charge compensation. The field E is $E = E_1$, see Fig. 5.1. The condition of

electrical neutrality in this range is fulfilled. To the right side of the front ($z_0 < z < d$) it is assumed that $N^\pm = N_0^\pm$ (non-perturbed concentrations) and $E = E_2$. This also satisfies the charge neutrality condition. Since the applied voltage is negative, it is expected that $E_{1,2} < 0$.

Consider now the balance of mobile charge carriers at the front point. Since $N^- = 0$ for $z < z_0$, no electrons can cross the front from the left side. For $z > z_0$, the electron flux is positive because $E_2 < 0$. As the field E is negative, the electron flux is directed to the right. The only possibility to maintain the balance for electrons is to set $v = -\mu_- E_2$. This means that the electrons are standing in the coordinate frame which moves with the front velocity v . The balance equation for the compensation charge means that their fluxes on both sides of the front are the same in the moving coordinate frame,

$$(N_0^+ - N_0^-)(\mu_+ E_1 - v) = N_0^+(\mu_+ E_2 - v). \quad (5.3)$$

Substituting $v = -\mu_- E_2$ in this equation, it is obtained that

$$\mu_+(N_0^+ - N_0^-)E_1 = (\mu_+ N_0^+ + \mu_+ N_0^-)E_2. \quad (5.4)$$

This equation has to be supplemented by the voltage-dropping relation

$$E_1 z_0 + (d - z_0)E_2 = -U_0. \quad (5.5)$$

Combining Eqs. (5.4) and (5.5), the fields E_1 and E_2 are calculated,

$$\frac{E_1}{E_0} = -\frac{\mu_+ N_0^+ + \mu_- N_0^-}{\mu_+(N_0^+ - N_0^-) + \xi(\mu_+ + \mu_-)N_0^-} \quad (5.6)$$

$$\frac{E_2}{E_0} = -\frac{\mu_+(N_0^+ - N_0^-)}{\mu_+(N_0^+ - N_0^-) + \xi(\mu_+ + \mu_-)N_0^-}, \quad (5.7)$$

where $\xi = z_0/d$ is the normalized front coordinate. Both fields are negative, as expected.

It is useful to use two ratios, $r_\mu = \mu_-/\mu_+$ and $r_N = N_0^+/N_0^-$, instead of four parameters N_0^\pm and μ^\pm . Being expressed by these ratios, Eqs. (5.6) and (5.7) read:

$$\frac{E_1}{E_0} = -\left[1 + \frac{(\xi - 1)(r_\mu + 1)}{(r_\mu + r_N)}\right]^{-1} \quad (5.8)$$

$$\frac{E_2}{E_0} = -\left[1 + \frac{\xi(r_\mu + 1)}{(r_\mu + r_N)}\right]^{-1} \quad (5.9)$$

For $z_0 = 0$ and $z_0 = d$ Eqs. (5.8) and (5.9) lead to $E_2 = -E_0$ and $E_1 = -E_0$ respectively. The field ratio E_1/E_2 is independent of the front coordinate z_0 ,

$$\frac{E_1}{E_2} = \frac{r_N + r_\mu}{r_N - 1}, \quad (5.10)$$

and it is larger than one.

We can also calculate the front velocity,

$$v = \mu_- E_0 \left[1 + \frac{\xi(r_\mu + 1)}{(r_N - 1)} \right]^{-1}. \quad (5.11)$$

It is a decreasing function of $\xi = z_0/d$. The velocity changes from $\mu_- E_0$ at $z_0 = 0$ to $\mu_- E_0(r_N - 1)/(r_N + r_\mu)$ at $z_0 = d$. The measurements of the position of the absorption front in Fig. 3.17 show a linear time dependence, i.e., a constant velocity of the absorption front. But in this experiment the current limit is active, i.e., the current is kept constant while the electric field is adapted continuously. A constant current means the amount of charges that flows through the crystal per time unit remains constant. If a fixed fraction of the current contributes to the oxidization a constant velocity of the front can be expected. With increasing current limit the amount of charges that flows and therefore the amount of charges that contributes to the oxidization is also increased. Hence the front velocity is enhanced.

A linear dependence of the front velocity on the electric field is predicted by the model. In Fig. 3.18 a linear dependence of the front velocity on the current limit is shown. According to Ohm's law $j = \sigma E$, the current density is proportional to the electric field, i.e., the front velocity depends linearly on the electric field, as expected. Even with a time dependent $E(t)$, the linear relation to the front velocity holds. However, future measurements of the absorption front at constant electric field and temperature are useful for a further support of the shock-wave model.

Since $v = dz_0/dt$, the time that is required for the front to cross the entire crystal is given by

$$t_0 = \int_0^d dz_0/v(z_0) = \frac{d}{\mu_- E_0} \left(1 + \frac{1}{2} \frac{r_\mu + 1}{r_N - 1} \right). \quad (5.12)$$

This time t_0 will be larger than $d/(\mu_- E_0)$, the time electrons would need to pass the entire crystal when no oxidization would take place and $r_\mu > 1$, i.e., more compensation charges than mobile electrons are present in the crystal. Since up to 4.0 % Fe the compensation charges do not limit the oxidization process, this condition seems to be fulfilled. It is analyzed in the following what kind of charge carriers are responsible for the charge compensation.

5.1.3 Charge compensation mechanism

The charges of the electrons that are removed from the crystal during the thermo-electric oxidization process have to be compensated by either the indiffusion of negative charge carriers, e.g., hydroxyl ions (OH^-) or oxygen ions (O^{2-}), or by the outdiffusion of positive

charge carriers, e.g., hydrogen ions (H^+), lithium ions (Li^+), niobium ions (Nb^{5+}), or iron ions ($\text{Fe}^{2+/3+}$). Significant movement of iron ions can be ruled out, because the strong Fe^{3+} peak around $\lambda = 483$ nm after the oxidization clearly indicates the presence of iron and, furthermore, the diffusion constant of iron, as known from the literature [126], is too small to allow large drift distances at the temperatures used. It is reasonable to consider the diffusion constants and activation energies of these ions. In Sect. 2.3.1 an overview is given. It can be seen that lithium is more mobile than oxygen and niobium at the temperatures used in the annealing experiments. However, the values for the activation energy and the diffusion constants vary in the literature within a very broad range. So one has to be sceptic about their validity. Nevertheless, hydrogen ions, that are even more mobile than lithium ions [86] ($E_A \approx 0.9$ eV, $D_0 \approx 10^{-3}$ cm²/s), and lithium ions are the most probable candidates as charge compensating ions. According to the shock-wave model the compensating ions drift to the cathode. Indeed surface precipitations are observed mainly close to the cathode (see Fig. 3.9, 3.14, and 3.16). A part of these precipitations is solvable in water, that is why the cathode detaches in warm water (Sect. 3.2.6). The mass spectroscopy shows that lithium is enriched in this layer. Consequently this layer consists most likely of lithium compounds that are solvable in water like lithium oxide (Li_2O), lithium hydroxide (LiOH), or lithium carbonate (Li_2CO_3). Most probably these compounds form when lithium leaves the crystal at the cathode in order to compensate for the electronic charges. Hydrogen can also leave the crystal at the cathode, but it probably does not form solid compounds that can be detected. These rather qualitative arguments are further supported by the analysis of the birefringence measurements (Sect. 3.2.5).

Birefringence changes It is shown that the oxidization is accompanied by changes of the birefringence of the crystals (Fig. 3.26). It is known from [127] that the birefringence is related to the lithium concentration by the following expression:

$$(n_e - n_o)(\lambda) = [c_{\text{Li}} - a(\lambda)]/b(\lambda), \quad (5.13)$$

with $(n_e - n_o)(\lambda)$ being the birefringence depending on the wavelength λ , c_{Li} the lithium concentration, and $a(\lambda)$ as well as $b(\lambda)$ known constants that depend only on the wavelength of the incident light. Small changes in the hydrogen concentration, that occur during the oxidization treatment, do not have a significant impact on the birefringence, as it is known from thermal fixing experiments [93]. According to the shock-wave model, the expected change in the lithium concentration is given by

$$\Delta c_{\text{Li}} = \Delta c_{\text{Fe}^{2+}} - \Delta c_{\text{H}^+}. \quad (5.14)$$

From the absorption measurements (see Fig. 3.25 (b)) the change of the Fe^{2+} concentration $\Delta c_{\text{Fe}^{2+}}$ and the change of the hydrogen concentration Δc_{H^+} are known (see Tab. 3.2).

With the help of Eq. (5.14), the change of the lithium concentration and subsequently $|\Delta(n_e - n_o)|_{\text{calc}}$, that is expected according to the shock-wave model, is calculated. For this calculation a starting value for the lithium concentration has to be assumed. In our highly doped crystals this value is not well known, but only *changes* of the birefringence are relevant for this analysis. They depend only very weakly on the initial lithium concentration. Additionally the changes of the lithium concentration ($\Delta c_{\text{Li}} \approx 10^{25} \text{ m}^{-3}$) are small compared to the absolute lithium concentration ($c_{\text{Li}} \approx 10^{28} \text{ m}^{-3}$). A starting value of 48.6 mol% Li_2O is used. The result is shown in Tab. 5.1 and compared to the values that are observed by the scans over the absorption front with the Sénarmont setup (Fig. 3.26). There is an excellent agreement between birefringence changes that are predicted from the

c_{Fe} [wt% Fe_2O_3]	pretreatment	$ \Delta(n_e - n_o) _{\text{meas}}$ [10^{-4}]	$ \Delta(n_e - n_o) _{\text{calc}}$ [10^{-4}]
0.05	reduced	1.3 ± 0.1	1.5 ± 0.5
0.5	—	1.2 ± 0.1	1.7 ± 0.5
1.0	oxidized	1.0 ± 0.1	1.4 ± 0.5
1.0	—	< 0.1	0.01 ± 0.003

Table 5.1: Nominal iron concentration c_{Fe} , pretreatment before the thermo-electric oxidation, measured birefringence changes $|\Delta(n_e - n_o)|_{\text{meas}}$, and calculated birefringence changes $|\Delta(n_e - n_o)|_{\text{calc}}$ for all crystals used.

absorption spectra and those that are measured with the Sénarmont setup. The rather large uncertainties originate from the relation between absorption and Fe^{2+} and H^+ concentrations that mainly contribute to the error bars. It is assumed that these relations are still valid for the highly iron-doped crystals used. Other contributions to the birefringence changes are also possible, e.g., absorption changes leading to changes of the refractive index (Kramers Kronig relations [128]), but they are expected to be small, because only a polarization-dependent absorption change can lead to a change of the birefringence. In our case the polarization dependence of the absorption peaks is rather weak. For the absorption changes that result from oxidization of iron centers a Kramers Kronig contribution to the birefringence changes of one order of magnitude smaller than the contribution from the change of the lithium concentration is estimated. Therefore Kramers Kronig related effects can be neglected.

5.1.4 Charge transport processes

The conductivity spectra of the iron-doped LiNbO_3 crystals (see Fig. 3.21) show good agreement with the random free energy barrier model. This model assumes a randomly

varying potential landscape (Fig. 2.10). LiNbO_3 with its many Nb_{Li} antisite defects and especially the highly iron-doped crystals seem to fulfill this condition very well. The DC conductivity σ_{dc} of the crystals in the as-grown and the oxidized state that are obtained from the fits show two thermally activated charge transport processes in the Arrhenius plots (see Fig. 3.22). The activation energies are about $E_{\text{A}}^{(1)} = 0.32$ eV and $E_{\text{A}}^{(2)} = 1.2$ eV. In Figs. 3.22 and 3.23 it can be seen that the straight line that corresponds to $E_{\text{A}}^{(1)} = 0.32$ eV is shifted with the iron concentration and with the oxidization state. Hence it scales with the Fe^{2+} concentration that is increased with the total iron concentration in the as-grown state of the crystals and that can be changed by oxidizing treatments. Obviously, the transport of electrons between iron centers is the dominating charge transport at temperatures where the straight line, corresponding to $E_{\text{A}}^{(1)}$, is present in the Arrhenius plot. There are a lot of reports of similar values in the literature. They are summarized in Tab. 5.2. In Refs. [94,129] it is shown that tunneling between adjacent iron centers is the dominant charge transport mechanism for LiNbO_3 crystals with doping levels ranging from 0.05 up to 3.0 % Fe, derived from holographic measurements of the dependence of the DC conductivity on the doping level (see Eq. (2.18)). Tunneling can be thermally activated by, e.g., excitation of electrons to energetically higher states within the potential well, but the exact mechanism cannot be clarified in this work.

The attribution of the part of the Arrhenius plot, which shows the larger activation energy $E_{\text{A}}^{(2)} = 1.2$ eV, to a charge carrier is rather complicated. In the literature lots of values for activation energies of undoped or slightly iron-doped crystals are reported. They are summarized in Tab. 5.2. Many reports attribute the activation energy to hydrogen impurities. In Fig. 3.23 three crystals with different hydrogen concentrations are compared. The hydrogen concentrations of the thermo-electrically oxidized and the conventionally oxidized sample vary by a factor of 50, while no significant shift of the straight line that corresponds to the activation energy of 1.2 eV is detected. Conclusively hydrogen impurities cannot be the dominant charge carrier in the highly-doped LiNbO_3 crystals at these temperatures above 250 °C. The reports in the literature, that attribute $E_{\text{A}}^{(2)}$ to hydrogen concern only undoped or slightly iron-doped LiNbO_3 crystals. It is quite possible that high iron doping influences the diffusivity of lithium ions. From Fig. 3.24 it can be seen that the activation energies for the untreated samples decrease slightly with increasing doping level leading to an increased lithium diffusivity. Further candidates for the charge transport corresponding to $E_{\text{A}}^{(2)}$ are lithium ions or lithium vacancies that have been shown to drift significantly inside the crystals at temperatures above 450 °C (see Sect. 5.1.3). The activation energies that are given for Li in the literature vary between 1 and 3 eV [86].

Doping level [wt % Fe ₂ O ₃]	$E_A^{(1)}$ ≈ 0.3 eV	$E_A^{(2)}$ ≈ 1 eV	Temperature range [°C]	Reference
0	–	1.43	950–1050	[100]
0	–	1.5	600–900	[130]
0	–	1.16	210–310	[131]
0	–	≈ 1.25	460–620	[132]
0	0.28	1.07	20–180	[133]
0.07	0.33	1.08	20–180	[133]
0.138	0.28	0.97	30–180	[134]
0.004–0.75	0.3	≈ 1.1	30–300	[135]

Table 5.2: Reference data from the literature: Doping levels, activation energies around 0.3 eV and 1 eV, temperature ranges used, and references.

5.1.5 Strength of the oxidization

The strength of the oxidization, i.e., the concentration ratio $c_{\text{Fe}^{2+}}/c_{\text{Fe}}$ can be determined by absorption spectroscopy and by conductivity spectroscopy.

5.1.5.1 Absorption spectroscopy

The absorption coefficients of the crystals in the as-grown state and after the thermoelectric oxidization (Figs. 3.10) are used to determine the Fe^{2+} concentrations according to Eq. (2.17). The concentrations of Fe^{2+} for all crystals in the as-grown and thermoelectrically oxidized state as well as the concentration ratios $c_{\text{Fe}^{2+}}/c_{\text{Fe}}$ are shown in Tab. 5.3. The resulting uncertainty of the Fe^{2+} concentration is about 30 %. The total iron concentration was determined by atomic absorption spectroscopy (see Tab. 3.1). The absorption coefficient around the wavelength 477 nm is governed by the Fe^{3+} absorption for all oxidized samples (Fig. 3.10 (b)). This Fe^{3+} peak is subtracted from the spectra in order to determine the Fe^{2+} concentration. However, no clear absorption peak of Fe^{2+} is visible for the oxidized samples. Hence the given value for the Fe^{2+} concentration and the concentration ratio $c_{\text{Fe}^{2+}}/c_{\text{Fe}}$ can be considered as an upper limit only. There can be contributions to the absorption coefficient from additional Fe^{3+} absorptions or scattering and absorption from induced bulk defects. In order to obtain exact values instead of upper limits for the Fe^{2+} concentration, the conductivity spectra are analyzed.

c_{Fe} [wt% Fe_2O_3]	As grown		Oxidized	
	$c_{\text{Fe}^{2+}}$ [$10^{25}/\text{m}^3$]	$c_{\text{Fe}^{2+}}/c_{\text{Fe}}$	$c_{\text{Fe}^{2+}}$ [$10^{25}/\text{m}^3$]	$c_{\text{Fe}^{2+}}/c_{\text{Fe}}$
0.5	3.0	0.20	< 0.048	$< 3.7 \times 10^{-3}$
1.0	5.3	0.18	< 0.055	$< 2.3 \times 10^{-3}$
2.0	10	0.18	< 0.065	$< 1.6 \times 10^{-3}$
3.0	15	0.17	< 0.3	$< 6.0 \times 10^{-3}$

Table 5.3: Nominal iron concentration c_{Fe} , Fe^{2+} concentration $c_{\text{Fe}^{2+}}$ and concentration ratio of Fe^{2+} and the total iron concentration $c_{\text{Fe}^{2+}}/c_{\text{Fe}}$ for crystals in the as-grown state as well as for thermo-electrically oxidized samples. The values for the oxidized crystals are obtained from absorption spectra.

5.1.5.2 Conductivity spectra

In the Arrhenius plot of the DC conductivities σ_{dc} obtained from the conductivity spectra a straight line is observed that scales with the Fe^{2+} concentration. It originates from a thermally activated charge transport of electrons from Fe^{2+} . Since results in Refs. [94, 129] suggest tunneling as charge transport mechanism, the residual Fe^{2+} concentration after the thermo-electric oxidization $c_{\text{Fe}^{2+}}(\text{oxidized})$ can be determined from the measured DC conductivities with the help of Eqs. 2.18 and 2.19:

$$\frac{\sigma_{\text{dc}}(\text{oxidized})}{\sigma_{\text{dc}}(\text{as grown})} = \frac{c_{\text{Fe}^{2+}}(\text{oxidized})c_{\text{Fe}}}{c_{\text{Fe}^{2+}}(\text{as grown})c_{\text{Fe}^{3+}}(\text{as grown})}. \quad (5.15)$$

The Fe^{2+} concentration in the as-grown state $c_{\text{Fe}^{2+}}(\text{as grown})$ is known from the absorption spectra (see Tab 5.3). Furthermore it is assumed that in the oxidized state $c_{\text{Fe}^{3+}} = c_{\text{Fe}}$ and the total iron concentration c_{Fe} is known from AAS (Tab. 3.1). The Fe^{3+} concentration in the as-grown state is calculated by $c_{\text{Fe}^{3+}}(\text{as grown}) = c_{\text{Fe}} - c_{\text{Fe}^{2+}}(\text{as grown})$. The results are summarized in Tab. 5.4. The values have errors of about 30 %.

For this analysis tunneling of electrons between adjacent Fe sites is assumed. It may also be possible that hopping between Fe centers via the conduction band takes place. In that case $\sigma_{\text{dc}} \propto c_{\text{Fe}^{2+}}$. The use of this relation leads to results within the same order of magnitude compared to the values presented in Tab. 5.4.

The obtained values for the Fe^{2+} concentrations are not upper limits, because the activation energy shows that the electrons are the dominant charge carriers at the temperatures used. It can be seen that $c_{\text{Fe}^{2+}}$ is diminished by up to five orders of magnitude due to the thermo-electric oxidization. The rather large value of the crystal doped with 0.5 % Fe is probably due to some small brown inhomogeneities in the degree of oxidization. It can be estimated

c_{Fe} [wt% Fe_2O_3]	As grown		Oxidized	
	$c_{\text{Fe}^{2+}}$ [$10^{25}/\text{m}^3$]	$c_{\text{Fe}^{2+}}/c_{\text{Fe}}$	$c_{\text{Fe}^{2+}}$ [$10^{21}/\text{m}^3$]	$c_{\text{Fe}^{2+}}/c_{\text{Fe}}$
0.5	3.0	0.20	29	2.2×10^{-4}
1.0	5.3	0.18	1.1	4.7×10^{-6}
2.0	10	0.18	2.1	5.8×10^{-6}

Table 5.4: Nominal iron concentration c_{Fe} , Fe^{2+} concentration $c_{\text{Fe}^{2+}}$ and concentration ratio of Fe^{2+} and the total iron concentration $c_{\text{Fe}^{2+}}/c_{\text{Fe}}$ for crystals in the as-grown state as well as for thermo-electrically oxidized samples. The values for the oxidized crystals are obtained from conductivity spectra.

that in the oxidized crystals containing 1.0 and 2.0 % Fe the residual Fe^{2+} concentration is similar or even smaller compared to that of undoped LiNbO_3 in the as-grown state.

5.2 Suppression of photorefraction

5.2.1 Photorefraction in highly iron-doped LiNbO_3 crystals

In Fig. 4.4 it is shown that the optical damage *decreases* with increasing iron-doping level for highly-doped, completely oxidized LiNbO_3 . This behavior can be explained with the one-center model. The refractive index change Δn is given by (Eqs. 2.6-2.11):

$$\Delta n \propto \frac{c_{\text{Fe}^{2+}}}{\sigma_{\text{ph}} + \sigma_{\text{d}}}. \quad (5.16)$$

The photoconductivity $\sigma_{\text{ph}} \propto c_{\text{Fe}^{2+}}/c_{\text{Fe}^{3+}}$ is strongly decreased by the oxidization, whereas the dark conductivity σ_{d} is enhanced with increasing doping level, because at the high doping levels used the dark conductivity is governed by tunneling of electrons between adjacent iron sites (Eqs. 2.18 and 2.19):

$$\sigma_{\text{d}} \propto \frac{c_{\text{Fe}^{2+}} c_{\text{Fe}^{3+}}}{c_{\text{Fe}}} \exp \left(-\frac{a}{\sqrt[3]{c_{\text{Fe}}}} \right). \quad (5.17)$$

The comparison with the conductivity spectra shows indeed that the dark conductivity of the oxidized samples increases with the doping level and is far above the dark conductivity of the undoped samples (Fig. 3.22). The conductivity of the crystal doped with 0.5 % Fe is probably increased by brown inhomogeneities of the Fe^{2+} concentration and therefore is as large as the conductivity of the sample with 1.0 % Fe.

At the high doping levels used the dark conductivity may exceed the photoconductivity significantly. Consequently the photoconductivity is neglected and the photorefractive index change can be expressed as

$$\Delta n \propto \exp\left(\frac{a}{\sqrt[3]{c_{\text{Fe}}}}\right), \quad (5.18)$$

using the approximation for complete oxidization $c_{\text{Fe}^{3+}} = c_{\text{Fe}}$. Hence, the model predicts that the optical damage, i.e., the refractive index change Δn , decreases strongly with increasing iron concentration. This matches the results in Fig. 4.4. Furthermore Δn is predicted to be independent of the residual Fe^{2+} concentration. Thus slight inhomogeneities in the oxidization strength do not affect the optical damage.

In Fig. 4.4 it can be seen that the optical damage of highly doped oxidized and undoped as-grown LiNbO_3 crystals is within the same order of magnitude. To understand this result one has mainly to consider the conductivities in Eq. 5.16, because the Fe^{2+} concentrations $c_{\text{Fe}^{2+}}$ are within the same order of magnitude for both, the highly iron-doped and oxidized as well as the undoped crystals in the as-grown state. In the case of the highly iron-doped and oxidized crystal the *photoconductivity* can be neglected, whereas the undoped crystal in the as-grown state has a negligible *dark conductivity*. To obtain similar refractive index changes for both crystals, the photoconductivity of the undoped crystal has to be equal to the dark conductivity of the highly-doped LiNbO_3 sample. The photoconductivity of undoped LiNbO_3 crystals in the as-grown state is known from the Ref. [36]. For the light intensities used in the beam fanning experiment it is about $\sigma_{\text{ph}} \approx 2 \times 10^{-12} (\Omega\text{cm})^{-1}$. The LiNbO_3 crystal doped with 2 % Fe exhibits a dark conductivity of $\sigma_{\text{d}} \approx 10^{-13} (\Omega\text{cm})^{-1}$ at room temperature (Fig. 3.22). For the oxidized crystal doped with 3 % Fe, that shows nearly equal optical damage compared to the undoped sample, no dark conductivity measurements were performed, but it can be estimated from Fig. 3.22 that its dark conductivity is in the order of magnitude $\sigma_{\text{d}} \approx 10^{-12} (\Omega\text{cm})^{-1}$. Hence, the dark conductivity of the doped sample is indeed similar to the photoconductivity of the undoped crystal. Hence the one-center model can describe the photorefractive behavior of these crystals at least qualitatively.

Probably untreated highly iron-doped LiNbO_3 samples exhibit even less photorefractive optical damage by orders of magnitude, because their dark conductivity is orders of magnitude higher compared to that of the oxidized samples (Fig. 3.22 (a)), but they are useless for applications, due to their huge absorption in the visible. In fact the absorption of the oxidized highly iron-doped LiNbO_3 crystals is already too high for most applications (see Fig. 3.10 (b)).

5.2.2 Photorefraction in undoped LiNbO₃ crystals

The thermo-electric oxidization is able to suppress the optical damage in congruently melting undoped lithium niobate crystals by about one order of magnitude over a wide range of light intensities at room temperature (Fig. 4.7). It has been shown that this oxidization method leads to a decrease of the Fe²⁺ concentrations by up to 5 orders of magnitude in highly iron-doped crystals (Tab. 5.4). It is reasonable to assume that also in undoped LiNbO₃ crystals with iron impurities of less than 1 ppm a strong oxidization takes place. The suppression of the optical damage, i.e., the light-induced refractive-index change, can be described within the framework of the one-center model (Sect. 2.2.2.1). The refractive index change Δn is given by:

$$\Delta n \propto \frac{c_{\text{Fe}^{2+}}}{\sigma_{\text{ph}} + \sigma_{\text{d}}} \propto \frac{c_{\text{Fe}^{3+}}}{1 + \sigma_{\text{d}}/\sigma_{\text{ph}}}. \quad (5.19)$$

Here $\sigma_{\text{ph}} \propto c_{\text{Fe}^{2+}}/c_{\text{Fe}^{3+}}$ has been used. The photoconductivity σ_{ph} is decreased by the oxidization, whereas the dark conductivity σ_{d} is governed by ionic charge transport processes and therefore independent of changes of the Fe²⁺ concentration (Sect. 5.1.4). The Fe³⁺ concentration $c_{\text{Fe}^{3+}}$ changes probably only slightly during the oxidization, because in the as-grown state the majority of the iron impurities are usually present as Fe³⁺. Consequently the oxidization leads to a decrease of the refractive-index change, i.e., a suppression of the optical damage.

As an alternative explanation for the optical damage suppression the increased stoichiometry due to the formation of LiNb₃O₈ is considered (see Eq. (2.15)). But a suppression of the optical damage would require $c_{\text{Li}}/(c_{\text{Li}} + c_{\text{Nb}}) > 49.9\%$ (Sect. 2.2.2.4). Such a strong increase of the lithium concentration can be ruled out, because in that case remarkable shifts of the band edge and the OH vibration peak in the absorption spectra occur [136]. These shifts are not observed after thermo-electric oxidization (Sect. 4.2.2.1).

It can be expected that the thermo-electric oxidization is also able to suppress the unwanted green induced infrared absorption (GRIIRA, see Sect. 2.2.2.3), that originated from the excitation of electrons from Fe²⁺ to the conduction band and the subsequent retrapping in Nb_{Li} [29]. In oxidized crystals almost no electrons are photoexcitable and therefore there cannot be any retrapping.

A strong enhancement of the second-harmonic output power is demonstrated (Fig. 4.8). It has been shown that a stable output power of up to 2.6 W is already obtainable. The ultimate limit for the output power is reached when two or more photons excite electrons directly from the valence band to the conduction band. They can be retrapped in Fe³⁺ centers and the photorefractive effect can arise. In that case a quadratic dependence of the optical damage on the incident light intensity is expected. In Fig. 4.7 it can be seen that a rather linear dependence is present. This implies that still electrons from impurity

centers are responsible for the residual optical damage. Hence a further improvement of the thermo-electric oxidization by optimizing its parameters is probably the best way to get even enhanced optical damage resistance.

The temperature dependence of the output power in Fig. 4.9 shows excellent agreement with the theory implying that the ferroelectric domain pattern, that was present in the crystals before the thermo-electric oxidization, is not affected by this treatment. This is a significant advantage in comparison to many other optical-damage-suppression-methods. In the following section a critical, quantitative comparison is tried.

5.3 Comparison of methods to suppress optical damage

Since the discovery of optical damage in 1966 [5] a variety of methods to suppress optical damage have been developed. They are reviewed in Sect. 2.2.2.4. It is challenging to compare these methods, because many different ways to quantify the optical damage were used, and the crystal quality is largely improved within the last 40 years. But in spite of that, a comparison is tried in Tab. 5.5. This comparison cannot be considered to be complete. Moreover, it is possible that values given here contain large errors or the application of old methods to state-of-the-art crystals could lead to different results. It is only valid to compare the factors F_{Sup} , i.e., the optical damage suppression compared to congruently melting undoped LiNbO_3 crystals, as long as the optical damage depends rather linear on the incident light intensity, because the factors were gained at different intensities.

Whereas most methods considered in Tab. 5.5 show larger suppression factors for optical damage than the thermo-electric oxidization, the striking advantage over most methods is the use of standard congruently melting undoped LiNbO_3 . That is why large second-harmonic output could be realized in this work. Other methods, that also use undoped congruently melting LiNbO_3 , possess other disadvantages: To heat the crystals up to 200 °C is rather inconvenient, because turbulences in the surrounding air can disturb the light beams. For the simultaneous illumination with UV light a second strong UV light source is required. Hence the thermo-electric oxidization is one of the most promising techniques to make LiNbO_3 crystals suitable for applications in nonlinear-optical devices.

5.4 Connections to other fields of science

In this section an overview is given about connections of the thermo-electric oxidization to other fields of physics.

Method	F_{Sup}	P_{SHG} [W]	at λ [nm]	Remark	Ref.
Mg doping	$\geq 80_e$	2.8_m	542	$T = 22\text{ }^\circ\text{C}$	[137]
Heating $200\text{ }^\circ\text{C}$	32_e	2.7_m	532	F_{Sup} est. from [69]	[138]
Thermo-electric oxidization	10_m	2.6_m	515	$T = 90\text{ }^\circ\text{C}$	this work
Mg doping + VTE	10^6_m	–	488	0.5 mol% Mg	[59]
Mg doping + stoichiometry	2000_m	–	532	0.78 mol% Mg	[139]
H^+ exchange	$10^2\text{--}10^4_m$		532	$c_{\text{Li}}/(c_{\text{Li}} + c_{\text{Nb}}) = 49.5\%$	[64]
Sc doping + SLN	10^3_m	–	532	1.3 mol% Sc	[60]
In doping	100_m	–	488	3 mol% In	[48]
Zn doping	80_m	–	488	7 % Zn	[44]
UV illumination	30_m	–	532	$I_{\text{UV}} = 6\text{ W/m}^2$	[67]
Sc doping	$\geq 20_e$	–	488	1.5 mol% Sc	[140]
Hf doping	20_m	–	532	4–8 mol% Hf	[141, 142]
Annealing $150\text{ }^\circ\text{C}$ + illumination	10_m	–	460	Ti indiffused waveguide	[74]
Heating $120\text{ }^\circ\text{C}$	5.5_m	–	488		[69]
Stoichiometry	2_m	–	514.5	depends strongly on $c_{\text{Li}}/(c_{\text{Li}} + c_{\text{Nb}}) = 49.9\%$	[28]

Table 5.5: Review of the optical-damage-suppression methods. The optical damage suppression factors F_{Sup} compared to congruently melting undoped LiNbO_3 crystals are given as well as the maximum realized continuous-wave second-harmonic output power P_{SHG} and the according light wavelenth λ . Pulsed second-harmonic generation is not reviewed. In the remark column important information concerning the comparison of the data are denoted. The References indicate from which publication the data are taken. The indices e and m show if the values are estimated or measured.

5.4.1 Thermal fixing

In Sect. 2.3.2.5 thermal fixing, a method to stabilize holograms, is introduced. In both methods, thermal fixing and thermo-electric oxidization, ions are shifted by electrical fields, either internal space-charge fields or externally applied electrical fields. Electrons are also moved either by the bulk photovoltaic effect or by the external field. Both methods use the enhanced mobility of charge carriers at elevated temperatures. The thermo-electric oxidization utilizes much higher temperatures because the charge carriers have to drift

much longer distances and in some cases higher temperatures are required to excite the electrons and mobilize them. In the case of hologram recording the electrons are mobilized by optical excitation. The final result in both cases is a region where the crystal is oxidized and the charge is compensated by moving ions.

5.4.2 Electrochromism

Electrochromism, a reversible color change of a material due to an applied electric field, was discovered to occur in WO_3 by Kraus in 1953 [143]. The reversible electric-field-induced incorporation of small ions such as H^+ or Li^+ into a host material that contains usually many vacancies leads to a coloration due to a change of the valence state of an ionic species or the creation of color centers. There is a vast amount of different materials exhibiting electrochromism using different mechanisms. Among them there are perovskites as well as metal oxides and others. An overview is given in [117]. Thermo-electric oxidization removes ions from a host material with many vacancies with a subsequent color change due to a change in valency state of an ion. Hence it can also be considered as an electrochromic process.

5.4.3 Lithium ion batteries

Most portable computers contain a Li ion battery as power source. During charging lithium ions from a lithium source, e.g., a lithium containing oxide material, drift into a host material, e.g., graphite. For charge compensation an electronic current flows through the external wire. During discharging this process is reversed. The reversible intercalation of lithium from a source into the host is crucial for this process. The large mobility of Li^+ ions is exploited. An overview is given in [144]. The thermo-electric oxidization also exploits the mobility of lithium ions and their ability to leave a crystal lattice, while an compensating electronic current flows through a wire.

5.4.4 Resistive switching

A recent promising development for mass storage devices comparable to hard disc drives is the resistive switching technology [145, 146]. Often oxide materials are used such as doped perovskites. Their resistance is switched between a highly resisting state and a state of low resistance with the help of an externally applied electric field. The microscopic processes are unknown for many of the materials that are used. The thermo-electric oxidization is able to change the resistance of iron-doped LiNbO_3 crystals by orders of magnitude with an electric field. It can be considered as resistive switching technique.

Chapter 6

Outlook

The thermo-electric oxidization is a very promising technique in order to change several crystal properties such as absorption, conductivity, and optical damage resistance. Each of these property changes can be of relevance for future applications.

In undoped LiNbO_3 crystals the electronic conductivity is much smaller than the ionic conductivity. An optimum oxidization is expected for nearly equal ionic and electronic conductivities as it is the case in highly iron-doped LiNbO_3 crystals. Another idea to improve the oxidization of undoped LiNbO_3 crystals is to illuminate the crystals during the thermo-electric oxidization. By this means the electronic conductivity can be increased, by the photoconductivity. The light intensity is a new parameter that allows to tune the optimum oxidization temperature. This may lead to a much enhanced oxidization.

To verify the shock-wave model further oxidization experiments at constant temperature and electric field are helpful. The velocity of the absorption front can be compared with the predictions of the model.

The modeling of the processes within the framework of the shock-wave model enables another promising possibility, the prediction of suitable annealing parameters from conductivity spectra. While the optimum parameters in this work were found by systematic variations of all parameters, this model may help to extend the thermo-electric oxidization to other materials. From measurements of the conductivity a prediction can be made whether a material is suited or not. It will be helpful to use Hall measurements to determine the sign of the charge carriers that are observed in the Arrhenius plots of the conductivity. If two charge transport processes are present with different signs at suitable temperatures, annealing experiments are promising. The conductivity values can be used to predict the oxidization temperature and the time, that such a treatment would last as well as the required electric field.

Although a microscopic model is given and supported by many different measurements, there are still open questions and spaces for improvement. For example it is not yet clear which factor is responsible for the residual Fe^{2+} concentration. Systematic studies of the dependence of the Fe^{2+} concentration after annealing on the annealing parameters will most probably lead to a further increase of the obtainable second-harmonic output.

Chapter 7

Summary

Lithium niobate crystals (LiNbO_3) are a promising material for nonlinear-optical applications like frequency conversion to generate visible light, e.g., in laser displays, but their achievable output power is greatly limited by the "optical damage", i.e., light-induced refractive-index changes caused by excitation of electrons from iron impurities and the subsequent retrapping in unilluminated areas of the crystal. The resulting space-charge fields modify the refractive indices due to the electro-optic effect. By this "photorefractive effect" the phase-matching condition, i.e., the avoidance of destructive interference between light generated at different crystal positions due to the dispersion of the fundamental wave and the converted wave, is disturbed critically above a certain light intensity threshold.

Several methods exist to suppress optical damage, e.g., high doping with metal ions such as magnesium. All methods possess inherent disadvantages, e.g., high doping usually leads to a worse crystal quality. Moreover, the periodic structuring of the crystallographic c -axis, which is necessary for the quasi phase matching, is complicated. In this work the influence of annealing treatments conducted in the presence of an externally applied electric field ("thermo-electric oxidation") on the valence state of iron impurities and thereby on the optical damage is investigated. It is observed that for highly iron-doped LiNbO_3 crystals this treatment leads to a nearly complete oxidation from Fe^{2+} to Fe^{3+} indicated by the disappearance of the absorption caused by Fe^{2+} . During the treatment an absorption front forms that moves with constant velocity through the crystal. The absorption in the visible as well as the electrical conductivity are decreased by up to five orders of magnitude due to this novel treatment. The ratio of the Fe^{2+} concentration to the total iron concentration – a measure for the strength of the oxidation – is in the order of 10^{-6} for oxidized crystals whereas it is about 10^{-1} for untreated samples. Birefringence changes are observed at the absorption front that are explained by the removal of hydrogen and lithium ions from the crystal that compensate for the charges of the also removed electrons from Fe^{2+} .

A microscopic shock-wave model is developed that explains the observed absorption front by a self-enhancing oxidization process due to the increase of the crystal resistance and the subsequently enhanced voltage drop over the oxidized volume.

Undoped congruently melting LiNbO_3 crystals are also thermo-electrically oxidized. Measurements of light-induced birefringence changes are utilized to show that the optical damage in these crystals is suppressed by one order of magnitude over a wide range of light intensities. This effect is explained within the framework of the one-center model by the nearly complete oxidization. The maximum achievable frequency-doubled light output power is measured for thermo-electrically oxidized and periodically-poled congruently melting LiNbO_3 crystals. An output power of up to 3 W light of the wavelength 515 nm is realized at 90 °C instead of about 30 mW output power for untreated crystals. The temperature dependence of the power of the frequency-doubled light shows that the periodic domain structure is not affected by the oxidizing treatment.

A striking advantage of the thermo-electric oxidization compared to other optical damage suppression method is that standard undoped, congruently melting, periodically-poled LiNbO_3 crystals can be improved. In most cases doping, e.g., with magnesium – the most advanced optical damage suppression method – causes additional challenges concerning crystal quality and periodic poling. Hence the thermo-electric oxidization appears as one of the most promising optical-damage-suppression methods for nonlinear-optical applications.

Bibliography

- [1] National Research Council, ed. *Harnessing light: Optical science and engineering for the 21st century*. National Academy Press, Washington, D.C., 1998.
- [2] “In pursuit of perfect TV color, with LED’s and lasers”, The New York Times, July 18, 2007.
- [3] A. M. Prokhorov and Y. S. Kuz’minov *Physics and chemistry of crystalline lithium niobate*. Adam Hilger, 1990.
- [4] Y. S. Kuz’minov *Lithium niobate crystals*. Cambridge International Sciences, 1995.
- [5] A. Ashkin, G. D. Boyd, J. M. Dziedzic, R. G. Smith, A. A. Ballmann, J. Levinstein, and K. Nassau, “Optically-induced refractive index inhomogeneities in LiNbO_3 and LiTaO_3 ”, *Appl. Phys. Lett.* **9**, 72 (1966).
- [6] K. Buse, “Light-induced charge transport processes in photorefractive crystals I: models and experimental methods”, *Appl. Phys. B: Lasers Opt.* **64**, 273 (1997).
- [7] W. Zachariasen *Untersuchungen über die Kristallstruktur von Sesquioxiden und Verbindungen ABO_3* . I Kommisjon Hos Jacob Dybwad, 1928.
- [8] R. Weis and T. Gaylord, “Lithium niobate: Summary of physical properties and crystal structure”, *Appl. Phys. A: Mater. Sci. Process.* **37**, 191 (1985).
- [9] F. Agullo-Lopez, J. A. Aust, F. Caccavale et al. *Properties of lithium niobate*. INSPEC, 2002.
- [10] K.-H. Hellwege, ed. *Landolt Börnstein - Numerical data and functional relationships in science and technology, new series*. Springer, 1981.
- [11] O. F. Schirmer, O. Thiemann, and M. Wöhlecke, “Defects in LiNbO_3 – I. Experimental aspects”, *J. Phys. Chem. Solids* **52**, 185 (1991).

- [12] U. Schlarb and K. Betzler, "Influence of the defect structure on the refractive indices of undoped and Mg-doped lithium niobate", *Phys. Rev. B* **50**, 751 (1994).
- [13] S. C. Abrahams and P. Marsh, "Defect structure dependence on composition in lithium niobate", *Acta Crystallogr., Sect. B: Struct. Sci.* **42**, 61 (1986).
- [14] M. G. Clark, F. J. Disalvo, A. M. Glass, and G. E. Peterson, "Electronic-structure and optical index damage of iron-doped lithium-niobate", *J. Chem. Phys.* **59**, 6209 (1973).
- [15] E. Hecht *Optics*. Addison-Wesley, Reading, Massachusetts, 1974.
- [16] P. Butcher and D. Cotter *The elements of nonlinear optics*. Cambridge University Press, 1990.
- [17] N. Bloembergen *Nonlinear optics*. World Scientific, 1996.
- [18] R. Boyd *Nonlinear optics*. Elsevier, 2003.
- [19] P. A. Franken, A. E. Hill, C. W. Peters, and G. Weinreich, "Generation of optical harmonics", *Phys. Rev. Lett.* **7**, 118 (1961).
- [20] P. F. Bordui and M. M. Fejer, "Inorganic crystals for nonlinear-optical frequency-conversion", *Ann. Rev. Mater. Sci.* **23**, 321 (1993).
- [21] V. Dmitriev, G. Gurzadyan, and D. Nikogosyan *Springer series in optical sciences volume 64: Handbook of nonlinear optical crystals*. Springer, 1991.
- [22] D. Hum and M. Fejer, "Quasi-phasematching", *C. R. Phys.* **8**, 180 (2007).
- [23] J. A. Armstrong, N. Bloembergen, J. Ducuing, and P. S. Pershan, "Interactions between light waves in a nonlinear dielectric", *Phys. Rev.* **127**, 1918 (1962).
- [24] F. Jermann and J. Otten, "The light-induced charge transport in LiNbO₃:Fe at high light intensities", *J. Opt. Soc. Am. B* **10**, 2085 (1993).
- [25] J. J. Liu, P. P. Banerjee, and Q. W. Song, "Role of diffusive, photovoltaic, and thermal effects in-beam fanning in LiNbO₃", *J. Opt. Soc. Am. B* **11**, 1688 (1994).
- [26] F. S. Chen, "Optically induced change of refractive indices in LiNbO₃ and LiTaO₃", *J. Appl. Phys.* **40**, 3389 (1969).
- [27] H. B. Serreze and R. B. Goldner, "Study of wavelength dependence of optically induced birefringence change in undoped LiNbO₃", *Appl. Phys. Lett.* **22**, 626 (1973).

-
- [28] M. Fontana, K. Chah, M. Aillerie, R. Mouras, and P. Bourson, "Optical damage resistance in undoped LiNbO_3 crystals", *Opt. Materials* **16**, 111 (2001).
- [29] Y. Furukawa, K. Kitamura, A. Alexandrovski, R. K. Route, M. M. Fejer, and G. Foulon, "Green-induced infrared absorption in MgO doped LiNbO_3 ", *Appl. Phys. Lett.* **78**, 1970 (2001).
- [30] G. E. Peterson, A. M. Glass, A. Carneval, and P. M. Bridenbaugh, "Control of laser damage in LiNbO_3 ", *J. Am. Ceram. Soc.* **56**, 278 (1973).
- [31] T. Volk, N. Rubinina, and M. Wohlecke, "Optical-damage-resistant impurities in lithium niobate", *J. Opt. Soc. Am. B* **11**, 1681 (1994).
- [32] Y. Furukawa, M. Sato, K. Kitamura, Y. Yajima, and M. Minakata, "Optical-damage resistance and crystal quality of LiNbO_3 single-crystals with various $[\text{Li}]/[\text{Nb}]$ ratios", *J. Appl. Phys.* **72**, 3250 (1992).
- [33] G. I. Malovichko, V. G. Grachev, E. P. Kokanyan, O. F. Schirmer, K. Betzler, B. Gather, F. Jermann, S. Klauer, U. Schlarb, and M. Wohlecke, "Characterization of stoichiometric LiNbO_3 grown from melts containing K_2O ", *Appl. Phys. A: Mater. Sci. Process.* **56**, 103 (1993).
- [34] R. Holman, P. Cressman, and J. Revelli, "Chemical control of optical damage in lithium niobate", *Appl. Phys. Lett.* **32**, 280 (1978).
- [35] D. Jundt, M. Fejer, and R. Byer, "Optical properties of lithium-rich lithium niobate fabricated by vapor transport equilibration", *IEEE J. Quant. Elec.* **26**, 135 (1990).
- [36] F. Jermann, M. Simon, and E. Krätzig, "Photorefractive properties of congruent and stoichiometric lithium niobate at high light intensities", *J. Opt. Soc. Am. B* **12**, 2066 (1995).
- [37] G. G. Zhong, J. Jin, and Z. K. Wu, "Measurements of optically induced refractive-index damage of lithium niobate doped with different concentrations of MgO ", *J. Opt. Soc. Am.* **70**, 631 (1980).
- [38] D. A. Bryan, R. Gerson, and H. E. Tomaschke, "Increased optical damage resistance in lithium niobate", *Appl. Phys. Lett.* **44**, 847 (1984).
- [39] M. C. Wengler, U. Heinemeyer, E. Soergel, and K. Buse, "Ultraviolet light-assisted domain inversion in magnesium-doped lithium niobate crystals", *J. Appl. Phys.* **98**, 064104 (2005).
- [40] T. Volk, V. Pryalkin, and N. Rubinina, "Optical-damage resistant $\text{LiNbO}_3\text{:Zn}$ crystal", *Opt. Lett.* **15**, 996 (1990).

- [41] T. R. Volk, M. A. Ivanov, V. I. Pryalkin, and N. M. Rubinina, “Photorefractive and nonlinear-optical properties of optical-damage resistant $\text{LiNbO}_3\text{:Zn}$ crystals”, *Ferroelectrics* **126**, 57 (1992).
- [42] Y. F. Kong, J. K. Wen, and H. F. Wang, “New doped lithium niobate crystal with high resistance to photorefractive - $\text{LiNbO}_3\text{:In}$ ”, *Appl. Phys. Lett.* **66**, 280 (1995).
- [43] Y. Zhang, Y. H. Xu, M. H. Li, and Y. Q. Zhao, “Growth and properties of Zn doped lithium niobate crystal”, *J. Cryst. Growth* **233**, 537 (2001).
- [44] T. Volk, B. Maximov, T. Chernaya, N. Rubinina, M. Wohlecke, and V. Simonov, “Photorefractive properties of $\text{LiNbO}_3\text{:Zn}$ crystals related to the defect structure”, *Appl. Phys. B: Lasers Opt.* **72**, 647 (2001).
- [45] T. Volk, B. Maximov, S. Sulyanov, N. Rubinina, and M. Wohlecke, “Relation of the photorefractive and optical-damage resistance to the intrinsic defect structure in LiNbO_3 crystals”, *Opt. Materials* **23**, 229 (2003).
- [46] T. R. Volk and N. M. Rubinina, “A new optical-damage resistant impurity in lithium-niobate crystals - indium”, *Ferroelectrics Letters Section* **14**, 37 (1992).
- [47] T. Volk, M. Wohlecke, N. Rubinina, N. V. Razumovski, F. Jermann, C. Fischer, and R. Bower, “ LiNbO_3 with the damage-resistant impurity indium”, *Appl. Phys. A: Mater. Sci. Process.* **60**, 217 (1995).
- [48] R. Wang, B. Wang, Y. L. Liu, and L. S. Shi, “Double-frequency properties of In:LiNbO_3 crystals”, *Cryst. Res. Technol.* **40**, 684 (2005).
- [49] J. K. Yamamoto, K. Kitamura, N. Iyi, S. Kimura, Y. Furukawa, and M. Sato, “Increased optical-damage resistance in Sc_2O_3 -doped LiNbO_3 ”, *Appl. Phys. Lett.* **61**, 2156 (1992).
- [50] E. P. Kokanyan, L. Razzari, I. Cristiani, V. Degiorgio, and J. B. Gruber, “Reduced photorefractive in hafnium-doped single-domain and periodically poled lithium niobate crystals”, *Appl. Phys. Lett.* **84**, 1880 (2004).
- [51] S. Q. Li, S. G. Liu, Y. F. Kong, D. L. Deng, G. Y. Gao, Y. B. Li, H. C. Gao, L. Zhang, Z. H. Hang, S. L. Chen, and J. J. Xu, “The optical damage resistance and absorption spectra of $\text{LiNbO}_3\text{:Hf}$ crystals”, *J. Phys.: Condens. Matter* **18**, 3527 (2006).
- [52] L. Sun, J. Wang, Q. Lv, B. Q. Liu, F. Y. Guo, R. Wang, W. Cai, Y. H. Xu, and L. C. Zhao, “Defect structure and optical damage resistance of In:Mg:Fe:LiNbO_3 crystals with various Li/Nb ratios”, *J. Cryst. Growth* **297**, 199 (2006).

-
- [53] Y. R. Nie, R. Wang, and B. Wang, "Growth and optical damage properties of In:Zn:LiNbO₃ waveguide substrate", *Cryst. Res. Technol.* **42**, 23 (2007).
- [54] Z. H. Hu, P. Guo, J. Y. Li, and X. H. Zhen, "Structure and optical damage resistance of In:Yb:Er:LiNbO₃ crystals", *Cryst. Res. Technol.* **42**, 488 (2007).
- [55] S. Q. Fang, Y. J. Qiao, X. H. Zhang, and F. R. Ling, "Increased optical damage resistance in Ce:Cu:LiNbO₃ by doping with Sc₂O₃ for quasi-nonvolatile holographic storage", *Phys. Status Solidi A* **204**, 833 (2007).
- [56] Y. Furukawa, K. Kitamura, S. Takekawa, K. Niwa, and H. Hatano, "Stoichiometric Mg:LiNbO₃ as an effective material for nonlinear optics", *Opt. Lett.* **23**, 1892 (1998).
- [57] K. Niwa, Y. Furukawa, S. Takekawa, and K. Kitamura, "Growth and characterization of MgO doped near stoichiometric LiNbO₃ crystals as a new nonlinear optical material", *J. Cryst. Growth* **208**, 493 (2000).
- [58] L. Palfalvi, G. Almasi, J. Hebling, A. Peter, and K. Polgar, "Measurement of laser-induced refractive index changes of Mg-doped congruent and stoichiometric LiNbO₃", *Appl. Phys. Lett.* **18**, 2245 (2002).
- [59] S. S. Chen, H. D. Liu, Y. F. Kong, Z. H. Huang, J. J. Xu, and G. Y. Zhang, "The resistance against optical damage of near-stoichiometric LiNbO₃:Mg crystals prepared by vapor transport equilibration", *Opt. Materials* **29**, 885 (2007).
- [60] M. Nakamura, S. Takekawa, Y. W. Liu, and K. Kitamura, "Crystal growth of Sc-doped near-stoichiometric LiNbO₃ and its characteristics", *J. Cryst. Growth* **281**, 549 (2005).
- [61] S. Q. Fang, B. Wang, T. Zhang, F. R. Ling, and Y. Q. Zhao, "Growth and characteristics of near-stoichiometric Zn:LiNbO₃ crystals grown by TSSG method", *Mater. Chem. Phys.* **89**, 249 (2005).
- [62] J. Li, X. J. Chen, B. Wu, B. Li, and S. H. Pan, "Laser-induced dark traces in doped LiNbO₃ crystals", *Appl. Phys. Lett.* **67**, 3384 (1995).
- [63] J. C. Deng, Y. F. Kong, J. Li, J. K. Wen, and B. Li, "Reduction of laser-induced dark traces in LiNbO₃:Mg and LiNbO₃:Zn by heat treatment", *J. Appl. Phys.* **79**, 9334 (1996).
- [64] O. Caballero-Calero, A. Garcia-Cabanes, J. M. Cabrera, M. Carrascosa, and A. Alcazar, "Optical damage in x-cut proton exchanged LiNbO₃ planar waveguides", *J. Appl. Phys.* **100**, 093103 (2006).

- [65] J. Olivares, E. Dieguez, F. J. Lopez, and J. M. Cabrera, “Fe ions in proton-exchanged LiNbO₃ waveguides”, *Appl. Phys. Lett.* **61**, 624 (1992).
- [66] K. Mizuuchi, A. Morikawa, T. Sugita, and K. Yamamoto, “Electric-field poling in Mg-doped LiNbO₃”, *J. Appl. Phys.* **96**, 6585 (2004).
- [67] Y. Liu, R. Jayavel, M. Nakamura, K. Kitamura, T. Yamaji, and H. Hatano, “Suppression of beam fanning in near-stoichiometric lithium niobate crystals by ultraviolet light irradiation”, *J. Appl. Phys.* **92**, 5578 (2002).
- [68] Y. Ninomia and T. Motoki, “LiNbO₃ light modulator”, *Rev. Sci. Instrum.* **43**, 519 (1972).
- [69] J. Rams, A. Alcazar-de Velasco, M. Carrascosa, J. M. Cabrera, and F. Agullo-Lopez, “Optical damage inhibition and thresholding effects in lithium niobate above room temperature”, *Opt. Commun.* **178**, 211 (2000).
- [70] E. Krätzig and R. Orlowski, “Light-induced charge transport in doped LiNbO₃ and LiTaO₃”, *Ferroelectrics* **27**, 241 (1980).
- [71] H. J. Levinstein, A. A. Ballmann, R. T. Denton, A. Ashkin, and J. M. Dziedzic, “Reduction of the susceptibility to optically induced index inhomogeneities”, *J. Appl. Phys.* **38**, 3101 (1967).
- [72] R. G. Smith, D. B. Fraser, R. T. Denton, and T. C. Rich, “Correlation of reduction in optically induced refractive-index inhomogeneity with OH content in LiTaO₃ and LiNbO₃”, *J. Appl. Phys.* **39**, 4600 (1968).
- [73] G. E. Peterson, A. M. Glass, and T. J. Negran, “Control of susceptibility of lithium niobate to laser-induced refractive index changes”, *Appl. Phys. Lett.* **19**, 130 (1971).
- [74] R. A. Becker, “Thermal fixing of Ti-indiffused LiNbO₃ channel waveguides for reduced photorefractive susceptibility”, *Appl. Phys. Lett.* **45**, 121 (1984).
- [75] G. E. Betts, F. J. O’Donnell, and K. G. Ray, “Effect of annealing on photorefractive damage in titanium-indiffused LiNbO₃ modulators”, *IEEE Photonic. Tech. L.* **6**, 211 (1994).
- [76] R. L. Byer, J. F. Young, and R. Feigelson, “Growth of high-quality LiNbO₃ crystals from congruent melt”, *J. Appl. Phys.* **41**, 2320 (1970).
- [77] H. M. O’Bryan, P. K. Gallagher, and C. D. Brandle, “Congruent composition and Li-rich phase-boundary of LiNbO₃”, *J. Am. Ceram. Soc.* **68**, 493 (1985).

-
- [78] B. C. Grabmaier, W. Wersing, and W. Koestler, "Properties of undoped and MgO-doped LiNbO_3 - Correlation to the defect structure", *J. Cryst. Growth* **110**, 339 (1991).
- [79] E. Born, J. Hornsteiner, T. Metzger, and E. Riha, "Diffusion of niobium in congruent lithium niobate", *Phys. Status Solidi A* **177**, 393 (2000).
- [80] M. A. McCoy, S. A. Dregia, and W. E. Lee, "Crystallography of surface nucleation and epitaxial-growth of lithium triniobate on congruent lithium-niobate", *J. Mater. Res.* **9**, 2029 (1994).
- [81] L. O. Svaasand, M. Eriksrud, G. Nakken, and A. P. Grande, "Solid-solution range of LiNbO_3 ", *J. Cryst. Growth* **22**, 230 (1974).
- [82] H. Nagata, T. Sakamoto, H. Honda, J. Ichikawa, E. M. Haga, K. Shima, and N. Haga, "Reduced thermal decomposition of OH-free LiNbO_3 substrates even in a dry gas atmosphere", *J. Mater. Res.* **11**, 2085 (1996).
- [83] A. Koide, H. Shimizu, and T. Saito, "Prevention of thermal degradations by using dehydrated LiNbO_3 crystal", *Jpn. J. Appl. Phys., Part 2* **33**, L957 (1994).
- [84] L. D. Pokrovskii, "Formation of the HNbO_3 phase by high-temperature annealing of LiNbO_3 substrates", *J. Struct. Chem.* **41**, 890 (2000).
- [85] A. Koide, H. Shimizu, and T. Saito, "Main cause of surface waveguides formed under LiNbO_3 crystal surface during thermal treatment", *Jpn. J. Appl. Phys., Part 1* **36**, 239 (1997).
- [86] D. P. Birnie, "Review - Analysis of diffusion in lithium niobate", *J. of Materials Science* **28**, 302 (1993).
- [87] Y. Q. Lu, Y. L. Lu, Q. Luo, Y. Y. Zhu, X. F. Chen, C. C. Xue, and N. B. Ming, "A change in domain morphology in optical superlattice LiNbO_3 induced by thermal annealing", *J. Phys.: Condens. Matter* **9**, 747 (1997).
- [88] H. Kurz, E. Krätzig, W. Keune, H. Engelmann, U. Gonser, B. Dischler, and A. Räuber, "Photorefractive centers in LiNbO_3 , studied by optical-, Mössbauer- and EPR-Methods", *Appl. Phys. A: Mater. Sci. Process.* **12**, 355 (1977).
- [89] K. Olimov, M. Falk, K. Buse, T. Woike, J. Hormes, and H. Modrow, "X-ray absorption near edge spectroscopy investigations of valency and lattice occupation site of Fe in highly iron-doped lithium niobate crystals", *J. Phys.: Condens. Matter* **18**, 5135 (2006).

- [90] K. Peithmann, J. Hukriede, K. Buse, and E. Krätzig, “Photorefractive properties of LiNbO_3 crystals doped by copper diffusion”, *Phys. Rev. B: Condens. Matter Mater. Phys.* **61**, 4615 (2000).
- [91] Y. P. Yang, D. Psaltis, M. Luennemann, D. Berben, U. Hartwig, and K. Buse, “Photorefractive properties of lithium niobate crystals doped with manganese”, *J. Opt. Soc. Am. B* **20**, 1491 (2003).
- [92] T. Vitova, M. Falk, T. Woike, K. Buse, and J. Hormes, “Combined X-ray and VIS absorption and nonresonant High Resolution X-Ray Emission Spectroscopy studies of valency and site occupation of manganese in Mn-doped lithium niobate crystals”, unpublished.
- [93] T. Volk and M. Wohlecke, “Thermal fixation of the photorefractive holograms recorded in lithium niobate and related crystals”, *Crit. Rev. Solid State Mater. Sci.* **30**, 125 (2005).
- [94] I. Nee, M. Müller, K. Buse, and E. Krätzig, “Role of iron in lithium-niobate crystals for the dark-storage time of holograms”, *J. Appl. Phys.* **88**, 4282 (2000).
- [95] J. C. Dyre, “The random free-energy barrier model for AC conduction in disordered solids”, *J. Appl. Phys.* **64**, 2456 (1988).
- [96] W. Phillips and D. L. Staebler, “Control of Fe^{2+} concentration in iron-doped lithium-niobate”, *J. Electron. Mater.* **3**, 601 (1974).
- [97] B. Dischler, J. Herrington, A. Räuber, and H. Kurz, “Correlation of photorefractive sensitivity in doped LiNbO_3 with chemically-induced changes in optical-absorption spectra”, *Solid State Commun.* **14**, 1233 (1974).
- [98] O. Thiemann and O. Schirmer, “Energy levels of several 3d impurities and EPR of Ti^{3+} in LiNbO_3 ”, *SPIE Electro-Optic and Magneto-Optic Materials* **1018**, 18 (1988).
- [99] P. Jorgensen and R. W. Bartlett, “High temperature transport processes in lithium niobate”, *J. Phys. Chem. Solids* **30**, 2639 (1969).
- [100] A. Mehta, E. K. Chang, and D. M. Smyth, “Ionic transport in LiNbO_3 ”, *J. Mater. Res.* **6**, 851 (1991).
- [101] P. F. Bordui, D. H. Jundt, E. M. Standifer, R. G. Norwood, R. L. Sawin, and J. D. Galipeau, “Chemically reduced lithium niobate single crystals: Processing, properties and improved surface acoustic wave device fabrication and performance”, *J. Appl. Phys.* **85**, 3766 (1999).

-
- [102] A. Garcia-Cabanes, L. Arizmendi, J. M. Cabrera, and F. Agullolopez, "New aspects of reduction treatments on Fe-doped LiNbO_3 ", *Cryst. Lattice Def. Amorph. Mat.* **15**, 131 (1987).
- [103] A. Dhar and A. Mansingh, "On the correlation between optical and electrical properties in reduced lithium niobate crystals", *J. Phys. D: Appl. Phys.* **24**, 1644 (1991).
- [104] H. Jhans, J. M. Honig, and C. N. R. Rao, "Optical properties of reduced LiNbO_3 ", *J. Phys. C* **19**, 3649 (1986).
- [105] H. G. Reik and D. Heese, "Frequency dependence of electrical conductivity of small polarons for high and low temperatures", *J. Phys. Chem. Solids* **28**, 581 (1967).
- [106] D. Sugak, Y. Zhydashvskii, Y. Sugak, O. Buryy, S. Ubizskii, I. Solskii, M. Schrader, and K. D. Becker, "In situ investigation of optical absorption changes in LiNbO_3 during reducing/oxidizing high-temperature treatments", *J. Phys.: Condens. Matter* **19**, 086211 (2007).
- [107] J. Crank *The mathematics of diffusion*. Oxford University Press, 1958.
- [108] J. Koppitz, O. F. Schirmer, and A. I. Kuznetsov, "Thermal-dissociation of bipolarons in reduced undoped LiNbO_3 ", *Europhys. Lett.* **4**, 1055 (1987).
- [109] M. H. Li, Y. Q. Zhao, K. B. Xu, and Y. H. Xu, "Oxidation and reduction treatment of photorefractive $\text{Fe}:\text{LiNbO}_3$ crystal", *Chin. Sci. Bull.* **41**, 655 (1996).
- [110] I. S. Akhmadullin, V. A. Golenishchev-Kutuzov, and S. A. Migachev, "Electronic structure of deep centers in LiNbO_3 ", *Phys. Solid State* **40**, 1012 (1998).
- [111] S. Ducharme and J. Feinberg, "Altering the photorefractive properties of BaTiO_3 by reduction and oxidation at 650 °C", *J. Opt. Soc. Am. B* **3**, 283 (1986).
- [112] V. Leyva, A. Agranat, and A. Yariv, "Dependence of the photorefractive properties of $\text{KTa}_{1-x}\text{Nb}_x\text{O}_3:\text{Cu,V}$ on Cu valence state concentration", *J. Appl. Phys.* **67**, 7162 (1990).
- [113] H. Levinstein and C. Capio, "Decorated dislocations in LiNbO_3 and LiTaO_3 ", *J. Appl. Phys.* **38**, 2761 (1967).
- [114] S. Bredikhin, S. Scharner, M. Klingler, V. Kveder, B. Red'kin, and W. Weppner, "Change of the stoichiometry and electrocoloration due to the injection of Li and O ions into lithium niobate crystals", *Ionics* **3**, 470 (1997).

- [115] S. Bredikhin, S. Scharner, M. Klingler, V. Kveder, B. Red'kin, and W. Weppner, "Peculiarity of O^{2-} and Li^+ electrodiffusion into lithium niobate single crystals", *Solid State Ionics* **135**, 737 (2000).
- [116] S. Bredikhin, S. Scharner, M. Klingler, V. Kveder, B. Red'kin, and W. Weppner, "Nonstoichiometry and electrocoloration due to injection of Li^+ and O^{2-} ions into lithium niobate crystals", *J. Appl. Phys.* **88**, 5687 (2000).
- [117] T. Yamase, "Photo- and electrochromism of polyoxometalates and related materials", *Chem. Rev.* **98**, 307 (1998).
- [118] K. Buse, S. Breer, K. Peithmann, S. Kapphan, M. Gao, and E. Krätzig, "Origin of thermal fixing in photorefractive lithium niobate crystals", *Phys. Rev. B: Condens. Matter Mater. Phys.* **56**, 1225 (1997).
- [119] R. Schmidt and I. Kaminow, "Metal-diffused optical waveguides in $LiNbO_3$ ", *Appl. Phys. Lett.* **25**, 458 (1974).
- [120] J. Kohler, N. Imanaka, and G. Y. Adachi, "Multivalent cationic conduction in crystalline solids", *Chem. Mater.* **10**, 3790 (1998).
- [121] J. M. Akmeida, G. Boyle, A. P. Leite, R. M. Delarue, C. N. Ironside, F. Cacavalle, P. Chakraborty, and I. Mansour, "Chromium diffusion in lithium-niobate for active optical wave-guides", *J. Appl. Phys.* **78**, 2193 (1995).
- [122] H. De Sénarmont, "Sur les modifications que la reflexion spéculaire à la surface des corps métallique imprime à un rayon de lumière polarisée", *Ann. Chim. Phys.* **73**, 337 (1840).
- [123] U. Schlarb and K. Betzler, "Refractive indices of lithium niobate as a function of wavelength and composition: A generalized fit", *Phys. Rev. B* **48**, 15613 (1993).
- [124] S. Kapphan and A. Breitskopf, "PE-layers and proton diffusion profiles in $LiNbO_3$ investigated with Fourier-IR and second harmonic generation", *phys. stat. sol. (a)* **133**, 159–166 (1992).
- [125] J. M. Cabrera, J. Olivares, M. Carrascosa, J. Rams, R. Müller, and E. Diéguez, "Hydrogen in lithium niobate", *Adv. Phys.* **45**, 349 (1996).
- [126] D. Kip, B. Gather, H. Bendig, and E. Krätzig, "Concentration and refractive index profiles of titanium- and iron-diffusion planar $LiNbO_3$ waveguides", *Phys. Status Solidi A* **139**, 241 (1993).
- [127] U. Schlarb and K. Betzler, "Refractive indices of lithium niobate as a function of wavelength and composition", *J. Appl. Phys.* **73**, 3472 (1993).

-
- [128] J. D. Jackson *Classical electrodynamics*. John Wiley & Sons, New York, 1999.
- [129] M. Falk, J. Japs, T. Woike, and K. Buse, "Charge transport in highly iron-doped oxidized lithium niobate single crystals", *Appl. Phys. B : Lasers Opt.* **87**, 119 (2007).
- [130] G. Bergmann, "Electrical conductivity of LiNbO₃", *Solid State Commun.* **6**, 77 (1968).
- [131] M. Masoud and P. Heitjans, "Impedance spectroscopy study of Li ion dynamics in single crystal, microcrystalline, nanocrystalline, and amorphous LiNbO₃", *Diffusion In Materials: Dimat 2004* **237-240**, 1016 (2005).
- [132] G. T. Niitsu, H. Nagata, and A. C. M. Rodrigues, "Electrical properties along the x and z axes of LiNbO₃ wafers", *J. Appl. Phys.* **95**, 3116 (2004).
- [133] S. V. Yevdokimov and A. V. Yatsenko, "Specific features of the dark conductivity in lithium niobate crystals of congruent composition", *Phys. Solid State* **48**, 336 (2006).
- [134] Y. P. Yang, I. Nee, K. Buse, and D. Psaltis, "Ionic and electronic dark decay of holograms in LiNbO₃:Fe crystals", *Appl. Phys. Lett.* **78**, 4076 (2001).
- [135] I. B. Barkan, M. V. Entin, and S. I. Marennikov, "Conductivity of Fe-doped LiNbO₃ crystals", *Phys. Status Solidi A* **44**, K91 (1977).
- [136] I. Földvari, K. Polgár, R. Voszka, and R. Balasanyang, "A simple method to determine the real composition of LiNbO₃ crystals", *Crystal Res. Technol.* **19**, 1659 (1984).
- [137] H. Furuya, A. Morikawa, K. Mizuuchi, and K. Yamamoto, "High-beam-quality continuous wave 3 W green-light generation in bulk periodically poled MgO:LiNbO₃", *Jpn. J. Appl. Phys., Part 1* **45**, 6704 (2006).
- [138] G. D. Miller, R. G. Batchko, W. M. Tulloch, D. R. Weise, M. M. Fejer, and R. L. Byer, "42%-efficient single-pass cw second-harmonic generation in periodically poled lithium niobate", *Opt. Lett.* **22**, 1834 (1997).
- [139] Y. Furukawa, K. Kitamura, S. Takekawa, A. Miyamoto, M. Terao, and N. Suda, "Photorefraction in LiNbO₃ as a function of [Li]/[Nb] and MgO concentrations", *Appl. Phys. Lett.* **77**, 2494 (2000).
- [140] J. Yamamoto, T. Yamazaki, and K. Yamagishi, "Noncritical phase matching and photorefractive damage in Sc₂O₃:LiNbO₃", *Appl. Phys. Lett.* **64**, 3228 (1994).
- [141] P. Galinetto, F. Rossella, P. Minzioni, L. Razzari, I. Cristiani, V. Degiorgio, and E. P. Kokanyan, "Microraman and photorefractivity study of hafnium-doped lithium niobate crystals", *J. Nonl. Opt. Phys. & Mater.* **15**, 9 (2006).

- [142] E. P. Kokanyan, “Hafnium-doped periodically poled lithium niobate crystals: Growth and photorefractive properties”, *Ferroelectrics* **341**, 119 (2006).
- [143] T. Kraus, “Labor-Bericht, Balzers AG”, unpublished.
- [144] J. Tarascon and M. Armand, “Issues and challenges facing rechargeable lithium batteries”, *Nature* **414**, 359 (2001).
- [145] A. Beck, J. G. Bednorz, C. Gerber, C. Rossel, and D. Widmer, “Reproducible switching effect in thin oxide films for memory applications”, *Appl. Phys. Lett.* **77**, 139 (2000).
- [146] S. F. Alvarado, F. La Mattina, and J. G. Bednorz, “Electroluminescence in $\text{SrTiO}_3\text{:Cr}$ single-crystal nonvolatile memory cells”, *Appl. Phys. A : Mater. Sci. Process.* **89**, 85 (2007).
- [147] A. Gerrard and J. Burch *Introduction to matrix methods in optics*. Courier Dover Publications, 1994.

Appendix A

Sénarmont method

The central statement of the Sénarmont compensator method is that a quarter-wave plate at a fixed angle is able to turn arbitrary elliptic light polarization into linear polarization. This statement is considered here in detail.

In general the light power behind the analyzer P is given by

$$P = \frac{1}{2}P_0\{1 + \sin(\frac{\pi}{2} - 2\alpha)\cos[2(\alpha - \beta)]\cos\Gamma - \sin[2(\alpha - \beta)]\sin\Gamma\}, \quad (\text{A.1})$$

as it can be deduced with the help of Müller matrices [15,147]. Here P_0 denotes the initial light power, α the angle of the quarter-wave plate, β the angle of the analyzer, and Γ the phase difference of ordinarily and extraordinarily polarized light beams that is induced by the birefringence of the crystal. The angles α and β are measured with respect to the axis that includes 45° with the y - and the c -axis, i.e., the plane of polarization of the incident light beam. Let the angle of the first polarizer be 0° to generate equal fractions of ordinarily and extraordinarily polarized light. If the quarter-wave plate is also adjusted to an angle of 0° Eq. (A.1) reads:

$$P = \frac{1}{2}P_0[1 + \cos(2\beta - \Gamma)]. \quad (\text{A.2})$$

It can be seen that for all values of Γ , i.e., every elliptic polarization, the transmitted light power behind the analyzer follows a cosine when the analyzer is rotated. The maximum of the cosine is at the angle $\beta = \Gamma/2 + 2\pi n$ with $n \in \mathbb{Z}$. At this angle the transmitted power equals the initial power ($P = P_0$). That means that the light beam behind the quarter-wave plate is linearly polarized.

List of publications

- K. Brands, M. Falk, D. Haertle, Th. Woike, K. Buse, "Impedance spectroscopy of iron-doped lithium niobate crystals", in preparation
- T. Vitova, M. Falk, Th. Woike, K. Buse, J. Hormes, "Combined X-ray and VIS absorption and non-resonant high resolution X-ray emission spectroscopy studies of valency and site occupation of manganese in Mn-doped lithium niobate crystals", in preparation
- T. Vitova, J. Hormes, M. Falk, K. Buse, "Site-selective investigation of site symmetry and site occupation of iron in Fe-doped lithium niobate crystals", submitted to J. Phys. Condens. Matter (2007)
- I. Breunig, M. Falk, B. Knabe, R. Sowade, K. Buse, P. Rabiei, D.H. Jundt, "Second harmonic generation of 2.6 W green light with thermo-electrically oxidized undoped congruent lithium niobate crystals below 100 °C", accepted by Appl. Phys. Lett. (2007)
- M. Falk, Th. Woike, K. Buse, "Charge compensation mechanism for thermo-electric oxidization in lithium niobate crystals", J. Appl. Phys. **102**, 063529 (2007)
- M. Falk, Th. Woike, K. Buse, "Reduction of optical damage in lithium niobate crystals by thermo-electric oxidization", Appl. Phys. Lett. **90**, 251912 (2007)
- J. Japs, M. Falk, Th. Woike, B. Sturman, K. Buse, "Charge transport properties of highly iron-doped LiNbO₃ crystals investigated with nanosecond light pulses", submitted to Phys. Rev. B (2007)
- M. Falk, J. Japs, Th. Woike, K. Buse, "Charge transport in highly iron-doped oxidized lithium niobate single crystals", Appl. Phys. B **87**, 119 (2007)

- Kh. Olimov, M. Falk, K. Buse, Th. Woike, J. Hormes, H. Modrow "X-ray absorption near edge spectroscopy investigations of valency and lattice occupation site of Fe in highly iron-doped lithium niobate crystals", J. Phys. Condens. Matter **18**, 5135 (2006)
- M. Falk, K. Buse "Thermo-electric method for nearly complete oxidization of highly iron-doped lithium niobate crystals", Appl. Phys. B **81**, 853 (2005)

Acknowledgements

I have been accompanied and supported by many people during my thesis. It is a pleasant aspect that I have now the opportunity to express my gratitude for all of them.

First of all I want to thank Prof. Dr. Karsten Buse for the opportunity to carry out my thesis at the Heinrich Hertz chair. He always supported me in every way and allowed me great latitude for my work. I thank Prof. Dr. Karl Maier for the primary review of this thesis as well as Prof. Dr. Werner Mader and PD Dr. Bernard Metsch for the secondary review. Furthermore I am much obliged to PD Dr. Theo Woike. He supported me always with bright ideas and I gained deeper understanding of physics and philosophy during our discussions. Special thanks go to Prof. Dr. Boris Sturman. Without him the shock-wave model would not have been developed. I am grateful to Prof. Dr. Marty M. Fejer for the invitation to the Stanford University. My research stay provided me extraordinary insights into the life and work at one of the world's leading universities. I thank the entire group of Prof. Dr. Fejer, especially Prof. Dr. Ashot S. Markosyan, Dr. Roger Route, Dr. David Hum, Dr. Carsten Langrock, and Vivian Drew, who supported me in many ways during my stay. I am also grateful to Dr. Dieter Jundt and Dr. Payam Rabiei from Crystal Technology, Inc., who supported me by providing high quality PPLN crystals. Special thanks go to my diploma students Dipl. Phys. Julius Japs, Dipl. Phys. Katharina Brands, and Stephan Gronenborn. The team work with each of them was both very successful and enjoyable. I am deeply grateful to the entire team of the Heinrich Hertz chair. The ambiance was always very stimulating. Dr. Ákos Hoffmann found solutions for every technical question. Dipl. Phys. Judith Schwesyg always took some time for discussions and I thank Dipl. Phys. Ingo Breunig, Dipl. Phys. Rosita Sowade, and Bastian Knabe for conducting the SHG experiments. Moreover I appreciate the excellent X-Ray studies of Tonya Vitova, Khusniddin Olimov, PD Dr. Hartwig Modrow, and Prof. Dr. Hormes, that led to a deeper understanding of the incorporation of Fe and Mg impurities in LiNbO_3 .

I feel a deep sense of gratitude for Kathrin Lehmann, who accompanied me with lots of patience and remains a unique friend to me. I am deeply grateful to Dipl. Phys. Judith Schwesyg, who accompanied me through all the ups and downs of my life and always helped me with words and deeds.

Last but not least I am much obliged to my sister Regina Falk and my parents Grita and Wolfgang Falk for their incredible support during my studies.